THESIS FOR THE DEGREE OF DOCTOR OF PHILOSOPHY

Momentum exchange between light and nanostructured matter

Daniel ANDRÉN

Department of Physics
Chalmers University of Technology
Göteborg, Sweden, 2021

MOMENTUM EXCHANGE BETWEEN LIGHT AND NANOSTRUCTURED MATTER

DANIEL ANDRÉN

ISBN 978-91-7905-468-7

Doktorsavhandlingar vid Chalmers tekniska högskola
Ny serie nr. 4935
ISSN 0346-718X

Division of Nano- and Biophysics
Department of Physics
Chalmers University of Technology
SE-412 96 Göteborg
Sweden
Telephone: +46 (0)31 - 772 10 00

Prevailing contact email: daniel.j.andren@gmail.com

Cover:
Illustration of the different types of momentum exchange between light and nanostructured matter investigated in this thesis. Left: Optical forces and torques used in optical tweezers to manipulate gold nanoparticles. Middle: Optical phase-gradient metasurfaces composed of nanoparticles designed to shape light by transferring momentum to it. Right: Microscopic metasurfaces designed as beam-deflectors. The linear and angular momentum change of light is counteracted by an optical reaction force and torque to conserve momentum, providing a handle to drive so-called metavehicles.

Printed in Sweden by
Chalmers digitaltryck
Chalmers Tekniska Högskola
Göteborg, Sweden, 2021

CHALMERS UNIVERSITY OF TECHNOLOGY

Department of Physics

Momentum exchange between light and nanostructured matter

Daniel ANDRÉN

Abstract

An object's translational and rotational motion is associated with linear and angular momenta. When multiple objects interact the exchange of momentum dictates the new system's motion. Since light, despite being massless, carries both linear and angular momentum it too can partake in this momentum exchange and mechanically affect matter in tangible ways. Due to conservation of momentum, any such exchange must be reciprocal, and the light therefore acquires an opposing momentum component. Hence, light and matter are inextricably connected and one can be manipulated to induce interesting effects to the other. Naturally, any such effect is facilitated by having strongly enhanced light-matter interaction, which for visible light is something that is obtained when nanostructured matter supports optical resonances. This thesis explores this reciprocal relationship and how nanostructured matter can be utilised to augment these phenomena.

Once focused by a strong lens, light can form *optical tweezers* which through optical forces and torques can confine and manipulate small particles in space. Metallic nanorods trapped in two dimensions against a cover glass can receive enough angular momentum from circularly polarised light to rotate with frequencies of several tens of kilohertz. In the first paper of this thesis, the photothermal effects associated with such optical rotations are studied to observe elevated thermal environments and morphological changes to the nanorod. Moreover, to elucidate upon the interactions between the trapped particle and the nearby glass surface, in the thesis' second paper a study is conducted to quantify the separation distance between the two under different trapping conditions. The particle is found to be confined $\sim$30-90 nm away from the surface.

The momentum exchange from a single nanoparticle to a light beam is negligible. However, by tailoring the response of an array of nanoparticles, *phase-gradient metasurfaces* can be constructed that collectively and controllably alter the incoming light's momentum in a macroscopically significant way, potentially enabling a paradigm shift to flat optical components. In the thesis' third paper, a novel fabrication technique to build such metasurfaces in a patternable polymer resist is investigated. The technique is shown to produce efficient, large-scale, potentially flexible, substrate-independent flat optical devices with reduced fabricational complexity, required time, and cost.

At present, optical metasurfaces are commonly viewed as stationary objects that manipulate light just like common optical components, but do not themselves react to the light's changed momentum. In the last paper of this thesis, it is realised that this is an overlooked potential source of optical force and torque. By incorporating a beam-steering metasurface into a microparticle, a new type of nanoscopic robot – a *metavehicle* – is invented. Its propulsion and steering are based on metasurface-induced optical momentum transfer and the metavehicle is shown to be driven in complex shapes even while transporting microscopic cargo.

KEYWORDS: nano-optics, optical force and torque, phase-gradient metasurface, rotary nanomotor, optical tweezers, metavehicle, momentum exchange.

List of publications

The following papers are included in this thesis:

I **Probing Photothermal Effects on Optically Trapped Gold Nanorods by Simultaneous Plasmon Spectroscopy and Brownian Dynamics Analysis**
Daniel Andrén, Lei Shao, Nils Odebo Länk, Srdjan S. Aćmović, Peter Johansson, & Mikael Käll
ACS Nano **11**, 10053 – 10061 (2017).

II **Surface Interactions of Gold Nanoparticles Optically Trapped Against an Interface**
Daniel Andrén, Nils Odebo Länk, Hana Šípová-Jungová, Steven Jones, Peter Johansson, & Mikael Käll
The Journal of Physical Chemistry C **123**, 16406 – 16414 (2019).

III **Large-Scale Metasurfaces Made by an Exposed Resist**
Daniel Andrén, Jade Martínes-Llinás, Philippe Tassin, Mikael Käll, & Ruggero Verre
ACS Photonics **7**, 885 – 892 (2020).

IV **Microscopic Metavehicles Powered and Steered by Embedded Optical Metasurfaces**
Daniel Andrén, Denis G. Baranov, Steven Jones, Giovanni Volpe, Ruggero Verre, & Mikael Käll
Under review (2021).

Declaration of author contributions:

I: I performed all optical experiments and data analysis, and wrote a first draft of the paper.

II: I performed optical experiments, Brownian motion simulations, and data analysis, and wrote a draft of the paper.

III: I performed the method development, numerical simulations, nanofabrication, and optical characterisation, as well as wrote a first draft of the paper.

IV: I developed the nanofabrication process, optimised optical properties, did all experimental work, and wrote a first draft of the manuscript.

Supplementary papers not included in this thesis:

For all papers below I took part in discussions and aided in the drafting of the manuscripts. Further specific contribution to each project are listed below.

S.I **Gold Nanorod Rotary Motors Driven by Resonant Light Scattering**
Lei Shao, Zhong-Jian Yang, Daniel Andrén, Peter Johansson, & Mikael Käll
ACS Nano **9**, 12542 – 12551 (2015).

My contribution: I assisted in optical measurements and performed some numerical analysis.

S.II **Brownian Fluctuations of an Optically Rotated Nanorod**
Faegheh Hajizadeh, Lei Shao, Daniel Andrén, Peter Johansson, Halina Rubinsztein-Dunlop, & Mikael Käll
Optica **4**, 746 – 751 (2017).

My contribution: I assisted in optical measurements and data-analysis.

S.III **Photothermal Heating of Plasmonic Nano-antennas: Influence on Trapped Particle Dynamics and Colloid Distribution**
Steven Jones, Daniel Andrén, Pawel Karpinski, & Mikael Käll
ACS Photonics **5**, 2878 – 2887 (2018).

My contribution: I performed the nanofabrication of nano-antennas.

S.IV **Photothermal DNA Release from Laser-tweezed Individual Gold Nanomotors Driven by Photon Angular Momentum**
Hana Šípová, Lei Shao, Nils Odebo Länk, Daniel Andrén, & Mikael Käll
ACS Photonics **5**, 2168 – 2175 (2018).

My contribution: I contributed to the data-analysis and thermal calculations.

S.V **Optically Controlled Stochastic Jumps of Individual Gold Nanorod Rotary Motors**
Lei Shao, Daniel Andrén, Steven Jones, Peter Johansson, & Mikael Käll
Physical Review B **98**, 085404 (2018).

My contribution: I contributed to conceiving the study and in interpreting the results.

S.VI **Construction and Operation of a Light-driven Gold Nanorod Rotary Motor System**
Daniel Andrén, Pawel Karpinski, & Mikael Käll
Journal of Visualized Experiments: JoVE **136** (2018).
`https://www.jove.com/video/57947/`

My contribution: I led the work on the article, wrote a draft of the paper, and generated the scientific content for the video version of the article.

S.VII **Counter-Propagating Optical Trapping of Resonant Nanoparticles Using a Uniaxial Crystal**
Pawel Karpinski, Steven Jones, Daniel Andrén, & Mikael Käll
Laser & Photonics Reviews **12**, 1800139 (2018).

My contribution: I performed the required nanofabrication.

S.VIII **Large-Scale Fabrication of Shaped High Index Dielectric Nanoparticles on a Substrate and in Solution**
Ruggero Verre, Nils Odebo Länk, Daniel Andrén, Hana Šípová, & Mikael Käll
Advanced Optical Materials **6**, 1701253 (2018).

My contribution: I performed part of the nanofabrication and optical experiments.

S.IX **A Gaussian Reflective Metasurface for Advanced Wavefront Manipulation**
Jade Martínes-Llinás, Clément Henry, Daniel Andrén, Ruggero Verre, Mikael Käll, & Philippe Tassin
Optics Express **27**, 21069 – 21082 (2019).

My contribution: I contributed to the numerical analysis and interpretation of the results.

S.X **Ultrafast Modulation of Thermoplasmonic Nano-Bubbles in Water**
Steven Jones, Daniel Andrén, Tomasz J. Antosiewicz, & Mikael Käll
Nano Letters **19**, 8294 – 8302 (2019).

My contribution: I was responsible for the nanofabrication.

S.XI **Nanoscale Inorganic Motors Driven by Light: Principles, Realizations, and Opportunities**
Hana Šípová-Jungová, Daniel Andrén, Steven Jones, & Mikael Käll
Chemical Reviews **120**, 269 – 287 (2019).

My contribution: I partook in defining the scope of the review, wrote the section about optical forces and torques, and provided feedback on the complete manuscript.

S.XII **Full Optical Characterization of Single Nanoparticles Using Quantitative Phase Imaging**
Samira Khadir, Daniel Andrén, Patrick C. Chaumet, Serge Monneret, Nicolar Bonod, Mikael Käll, & Guillaume Baffou
Optica **7**, 243 – 248 (2020).

My contribution: I fabricated gold nanorods to be characterised.

S.XIII **Strong Transient Flows Generated by Thermoplasmonic Bubble Nucleation**
Steven Jones, Daniel Andrén, Tomasz J. Antosiewicz, Alexander Stilgoe, Halina Rubinsztein-Dunlop, & Mikael Käll
ACS Nano **14**, 17468 – 17475 (2020).

My contribution: I was responsible for the nanofabrication.

S.XIV **Metasurface Optical Characterization Using Quadriwave Lateral Shearing Interferometry**
Samira Khadir, Daniel Andrén, Ruggero Verre, Qinghua Song, Serge Monneret, Patrice Genevet, Mikael Käll, & Guillaume Baffou
ACS Photonics **8**, 603 – 613 (2021).

My contribution: I optimised and fabricated the Pancharatnam-Berry metasurfaces and contributed to the interpretation of the data.

Acknowledgements

The last five years have been a great source of personal and scientific growth for me. I am thankful to many people who have inspired and helped me to get to this point where I am presenting a doctoral thesis.

Mikael, thank you for believing in me from start to finish and for your valuable supervision throughout. Your breadth of knowledge and approach to science has inspired me to grow and I've become a better scientist thanks to your guidance.

Steven, I could not have asked for a better companion with whom to share the journey through this endeavour. My most sincere "thanks bud"!

Ruggero, trying to keep up with you has been a blast! Your enthusiasm is contagious and the nanofabrication you taught me has been of inestimable importance. Best of luck with the new job.

Nils, the older sibling of my Ph.D. student family. Thank you for clearing out my confusion regarding both theory and graduate work formalities. I'm glad to stay updated on your post-disertation career and expanding family!

Adriana, few people spread as much happiness around them as you do. Thank you for that. Also, if I ever finish the IM swim, know you made that happen!

Mahdi and Pantea, I doubt that Mikael could have hired a better duo to replace me and Steve! I look forward to seeing what the future brings for you.

Hana, it's amazing to see your family grow, but we sure miss you! Thanks for all the help with chemistry, as well as for all of our chats about life and science.

Lei, thank you for sparking my interest in nanoplasmonics and for everything you taught me early on. I know you have a bright future in academia!

Special thanks to the rest of the coauthors of the papers I've been mainly involved in. Srdjan, Peter, Pawel, Jade, Philippe, Denis, and Giovanni – we have made beautiful science together and I have learnt a lot from you all!

Also, a big thanks to all the past and present group members of the Bionanophotonics division for making it a great place to work. You know I have great things to say about you too. Unfortunately, my space here is limited. Suffice it to say, I hope I've been as much of a reason for you to enjoy your job as you have for me to enjoy mine!

Moreover, I am thankful to the Excellence Initiative Nano for believing in me and funding my research, and to all the people working at Myfab Chalmers for providing valuable help and guidance.

Lastly, my deepest gratitude to my loving wife and family. I would not have embarked on this journey, nor enjoyed it as much, if it wasn't for your unwavering support and encouragement.

Daniel Andrén

Göteborg, 2020/03/15

Contents

Chapter 1

Introduction

Light is everywhere. Yet it will travel unimpeded from the furthest outskirts of the universe unless it encounters matter. Hence, all our experiences of light arise from its interaction with matter, making the two inextricably connected. For instance, when a light-beam strikes an object, it in turn reradiates in the form of diffusely and specularly scattered light, encoding the shape and characteristic of the object. The scattered light eventually is absorbed by our eye's light-sensitive chromophore retinal, or a photosensitive detector, enabling us to *see* the object.

The electromagnetic spectrum encompasses all radiation from gamma rays to radio signals. What is colloquially referred to as (visible) *light* is the narrow part of this spectrum (400-750 nm), which can be visually perceived by humans. Nevertheless, in many cases, scientists are a bit lenient with the term and let "light" encompass also near-infrared (NIR, $\lambda \lesssim 1100$ nm), and less frequently also near-ultraviolet (near-UV) wavelengths. Regardless, since being an electromagnetic field it is fundamentally governed by Maxwell's equations and its propagation by the electromagnetic wave equation. Moreover, light often has a specific polarisation associated with it, which in this thesis will be central [1].

Apart from carrying energy, light also possesses linear and angular momentum. The linear momentum component was first suggested by Kepler in 1619 when observing comet tails pointing away from the sun and subsequently predicted analytically by Maxwell in 1873. The net directional energy flux of the wave (as described by the Poynting vector) is found to result in a radiation pressure in the direction of propagation. Furthermore, the angular momentum component can itself be decomposed into spin and orbital angular momentum. The spin angular momentum is associated with the degree of circular polarisation of light, whereas the orbital component arises from its spatial distribution. The interaction between light and matter can in a variety of ways lead to the exchange of momentum, enabling both tangible mechanical effects and the tailoring of light beams by engineering the structure and optical properties of matter. In essence, the multifaceted momentum exchange between light and matter is the heart of this thesis, and augmented and potentially new functions are explored by nanostructuring matter so that it acts as optical antennas.

An antenna's constituent material, size and shape are chosen for it to be *resonantly* excited by the electromagnetic wave within its particular information-carrying frequency band. Generally, such resonant interaction occurs when the wavelength of radiation and the antenna element's characteristic dimension are comparable. Hence, radio-wave antennas have constituent elements of just below a metre (Figure 1.1a). If the antenna size is reduced, concomitantly the optimal wavelength

of operation is too. A beautiful demonstration of this can be seen from a simple experiment at home. By putting two nearly-touching grapes in a microwave oven, the refractive index and wavelength of radiation matches to such a degree that the antenna concentrates enough energy to form plasma in the gap between the grapes (Figure 1.1b) [2]. Consequently, by continued reduction of the antenna's size, it should be possible to construct *optical antennas* that efficiently react to and manipulate visible light [3]. Indeed, by choosing materials with appropriate bulk optical properties and subsequently structuring them to have characteristic dimensions on the order of 10-1000 nm, resonantly enhanced light-matter interactions are attainable (Figure 1.1c).

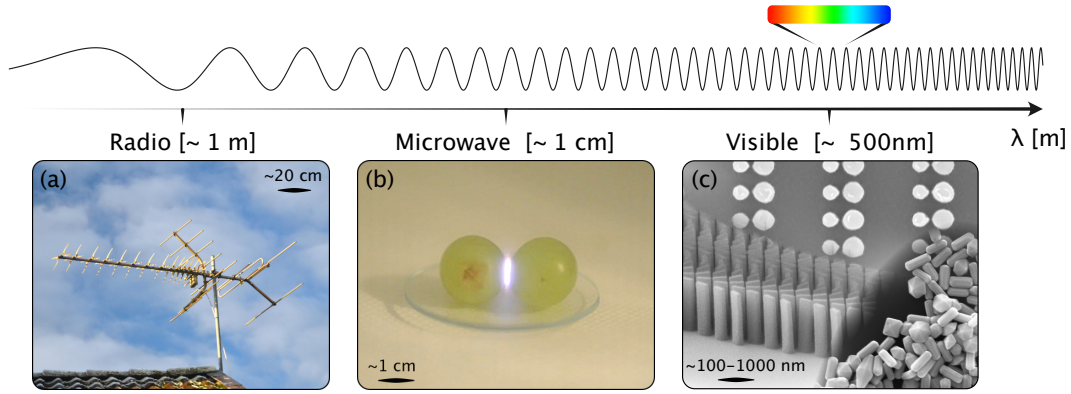

FIGURE 1.1: Illustration of shape-dependent enhanced interaction between electromagnetic radiation and matter at different wavelengths (not to scale). (a) A radio-antenna is constructed to receive and transmit electromagnetic signals with a wavelength on the order of metres. (b) The size and refractive index of grapes (or any other small water-based round object) is such that when placed in a microwave, they act as an antenna for microwave radiation. This concentrates a sufficient amount of energy in the gap for plasma to form. Figure from [2] under CC BY-NC-ND 4.0. (c) Examples of nanostructured objects investigated in this thesis, functioning as antennas at optical wavelengths.

These optical resonance effects are studied in the field of nano-optics, and single-particle resonances are introduced in Chapter 2. The material category of choice for several decades has been noble metals, which when nanostructured support plasmonic resonances and produce vivid colours of both colloidal solutions and surfaces [4, 5]. Depending on the exact size, dimension, and environment of the nanoparticle, its optical response can be varied widely. In plasmonics these strongly enhanced interactions have been the focus of research efforts related to e.g. bio-sensing [6], medicine [7, 8], data storage [9], solar cells [10], and photocatalysis [11]. For long, nano-optics was more or less synonymous with plasmonics; however, in recent years a new candidate has entered the race. Many of the advantageous nano-optical resonance effects can be attained also with low-loss, high-index dielectric nanoparticles [12], while avoiding potentially detrimental aspects of plasmonic nanoparticles such as strong Ohmic heating, lack of magnetic response, and CMOS incompatibility.

A sufficiently small single nanoparticle interacts with incoming radiation much like an induced point dipole. This gives rise to scattering and absorption, which can be understood from simplified phenomenological models. However, by combining a multitude of nanoparticles, their optical response will combine and present previously unexpected collective effects. One can then obtain an optical *metamaterial* that have unusual properties not found in natural materials. For instance, metamaterials have been suggested to present negative refractive indices

[13], perfect lensing [14], and cloaking [15]. At long (microwave and longer) wavelengths there are few complications to make three-dimensional periodic structures, but when the wavelength of operation shrinks towards NIR and visible wavelengths the challenges compound. Instead, scientists have adopted an approach where a single surface is decorated with engineered nanostructures, forming a *metasurface* [16]. In particular, metasurfaces that modify the phase of the transmitted light have attracted appreciable attention in the last decade since they enable the creation of flat optical components capable of modifying the direction and polarisation of light [17]. In Chapter 3 the conception and execution of such *phase-gradient metasurfaces* are introduced. In the context of this thesis, the changed propagation direction or polarisation of light in such metasurfaces is unavoidably associated with momentum exchange between the incoming light and the nanostructured matter.

Experimental verification of the transfer of linear momentum from light to matter was done early last century [18]. However, since the resulting optical forces are vanishingly small by our macroscopic world's standards it was long thought that it was a parenthetical effect (e.g. the radiation pressure produced by the sun on a square meter of the Earth is on the order of a few μN, which is less than a single grain of sand distributed over this area). That is until Arthur Ashkin performed his iconic work in the 1970-80s. He found that by focusing laser light through a strong lens, μm-sized latex beads could be affected by an appreciable force [19]. Subsequent experiments led to the development of the "single-beam gradient optical trap" [20–22], where small particles could be confined in three dimensions, due to a gradient force that directs a particle towards the high-intensity region of a focused beam. These so-called *optical tweezers* have since their conception produced ripples through both the academic as well as industrial landscape, with proven usefulness in as diverse fields as molecular biology for studying forces [23–25], and for cooling single atoms in atomic physics [26, 27]. Its usefulness is well illustrated by the fact that half of the 2018 Nobel prize in Physics was awarded to Ashkin for the conception of optical tweezers.

The enhanced optical interaction of resonant nanoparticles could potentially be beneficial to strengthen the confinement in optical tweezers. Plasmonic particles were initially challenging to trap in 3D until it was realised that an off-resonance laser could confine small metallic nanospheres even more effectively than their dielectric counterparts [28]. Since then, three-dimensional optical trapping of metallic nanoparticles have been investigated from a fundamental perspective [29–33], as well as for applications: e.g. within thermal generation and thermodynamics [34–37], novel nanofabrication techniques [38], the study of biological systems [39, 40], and enhanced chemical reactions [41].

Furthermore, angular momentum transfer to matter was first experimentally demonstrated a few decades after its linear counterpart [42]. As with optical forces, the torque associated with light's angular momentum is negligible on macroscopic scales. Yet, in optical tweezers, the light intensity becomes sufficient for also the optical torque to become noticeable. Initially, optical torque was applied to rotate dielectric microparticles [43–45], but soon it was realised that the enhanced optical response of resonant nanoparticles could amplify optical torques as well [46, 47]. In Chapter 4, the momentum transfer from light to matter producing significant optical forces and torques are further discussed.

Unfortunately, the nanoparticles with the strongest optical interactions are the least optimal for 3D trapping. Their large absorption and scattering prevent them from being confined in three dimensions by a single laser beam since they are pushed from the stable trapping location by non-conservative radiation pressure. Instead, a geometry where a particle is trapped in two dimensions against a cover-glass is often employed. The surface is made to have the same charge polarity as the nanoparticle and hence the destabilising scattering force is counteracted by Coulomb repulsion from the surface. In this trapping geometry the benefits of nanoparticle resonances can be fully exploited, enabling exotic optomechanical systems such as optical vortex traps [48], optical binding [49], ring traps [50], and optical printing lithography [51]. Another system enabled in such a 2D optical trapping environment is a high-speed rotary nanomotor [52]. Due to efficient transfer of angular momentum when the laser light is circularly polarised, a metallic nanorod can reach rotation frequencies of more than 40 kHz in water [53]. In **Paper I**, we studied such rotary nanomotors and in particular the unavoidable photothermal effects present when confining resonant particles in high-intensity near-resonant optical fields. By combining Brownian motion analysis and dark-field spectroscopy, both optically induced morphological changes of the nanorods and superheated water around the nanomotor were observed.

Throughout previous studies in 2D optical tweezers, the separation distance between the confined resonant nanoparticle and the repulsive surface has remained unknown. Often a particle is even viewed as residing in a homogenous aqueous environment. However, particle-surface interactions are known to give rise to alterations in hydrodynamic properties, Brownian motion, optical, and thermal properties of the trapped object. Hence, knowledge of the separation distance is critical for making confident claims in any system utilising 2D optical tweezers geometries. Therefore, in **Paper II**, analysis and measurements were performed to characterise nanoparticle/surface interaction and separation distance. Through separation distance-sensitive scattering from frustrated total internal reflection combined with numerical simulations of Brownian dynamics, the separation distance for an archetypal nanoparticle, a gold nanosphere with a diameter of 100 nm, was determined to be below one particle diameter.

The impressive range of light-manipulation attainable with phase-gradient metasurfaces alludes to the possibility of using them for optomechanical manipulation as well. The most intuitive and intriguing such application is maybe to replace the complex, bulky, and expensive objective lens with a flat counterpart – to construct optical tweezers with reduced form-factor. The idea has recently been realised [54] and even demonstrate some additional functionalities such as polarisation-dependent [55], and vortex-beam trapping [56, 57]. Regardless of the intended use of a phase-gradient metasurface, it is of the essence to enable efficient, safe, and economical fabrication schemes. In an exploratory study aimed at constructing phase-gradient metasurfaces for optical tweezers, we realised a new fabrication technique that has the potential to fulfil all these requirements. This method is presented in **Paper III** and enables the construction of high-efficiency phase-gradient metasurfaces directly in a patterned negative resist, instead of using this as an intermediate step in a more complex fabrication process. We demonstrate metalenses with focusing efficiencies of above 50%, the ability to fabricate macroscopic flat optics, and flexible and substrate-independent metasurfaces.

The manipulation of propagation direction and polarisation of light in phase-gradient metasurfaces implies momentum exchange between the incoming light and the metasurface. In optical tweezers, linear and angular momentum exchange and the conservation thereof is the origin of optical forces and torques acting on matter. However, in the metasurface community, momentum exchange is always discussed from the perspective of the momentum gained by light, while the concomitant opposite momentum experienced by the metasurface is overlooked. In **Paper IV** we realise that, by properly designing a phase-gradient metasurface and subsequently embedding it in a microparticle, the reaction forces and torques arising due to light-matter momentum exchange can be made useful. Even in extended semi-plane-wave illumination so-called *metavehicles* can be propelled by redirecting normally incident light and steered in complex patterns by the control of light's polarisation.

Generally, performing research within nano-optics requires a wide range of specialised competencies within theoretical electrodynamics, numerical simulations, nanofabrication, and experimental optical characterisation. In summary, when a novel idea is conceived, a nanostructure is designed to interact well with chosen light, oftentimes using numerical simulations. Thereafter, the optimised structure needs to be experimentally realised, which can either be done with top-down or bottom-up nanofabrication. Subsequently, optical characterisation needs to be performed to verify that the expected behaviour is indeed observed. The most critical methods are discussed in the appended papers; however, the scope of journal publications does not allow a detailed examination of all the techniques. Therefore, Chapter 5 attempts to bridge the gap between what is conferred in the articles and the full understanding needed to reproduce the research presented in the appended papers.

Lastly, performing research allows us to expand the sphere of human knowledge, if only ever so slightly. When doing so one needs to pay attention to the most minute details and run the risk of losing track of the bigger picture. Therefore, to conclude this thesis, Chapter 6 seeks to reflect on the appended papers in a wider context, acknowledge some still unresolved questions, as well as outline possible future implications of the attained results. However, before getting to the point where all that can be appreciated we need to dive into the specific topics introduced above. Let's get started!

Chapter 2

Resonant light-matter interactions

Resonance is a ubiquitous phenomenon in physics. It occurs when an object with a certain natural frequency becomes subject to a perturbation with a frequency that matches its natural frequency. When this resonance condition is fulfilled the amplitude of the object's response to the perturbation becomes increasingly large. Resonances can be seen on all size scales from atomic to stellar and for systems affected by any type of force, be it mechanical, electrical, optical, or other.

The simplest case of a resonance is that of the driven harmonic oscillator, which can be illustrated by the everyday experience of pushing a child on a swing. From this system, we already have an intuitive understanding of the amplitude and phase response of a resonance. To maximise the swing's amplitude we push the swing with a certain frequency at its highest point, corresponding to 90° out of phase with the swing. If we push faster or slower the swing's amplitude diminishes quickly. Figure 2.1 illustrates these three cases and graphs the

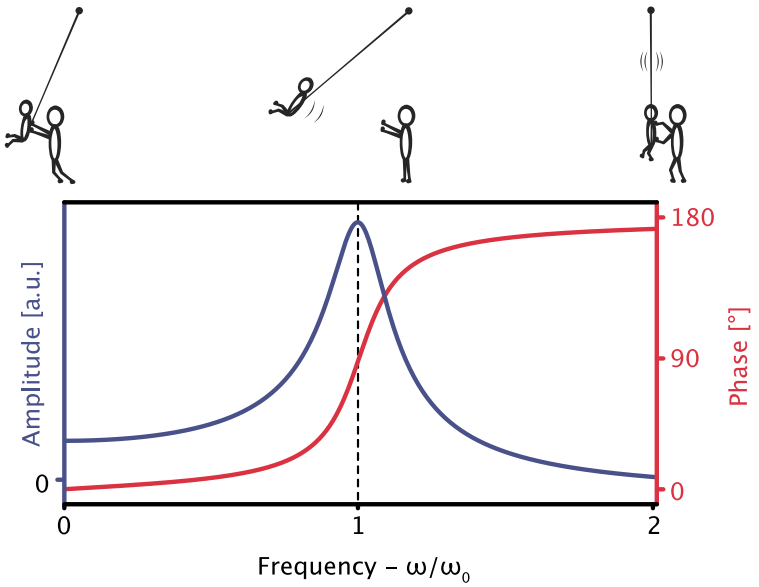

FIGURE 2.1: The amplitude and phase relation for a driven harmonic resonator graphed against frequency normalised by the resonance frequency. The response at three different frequency domains is illustrated with the intuitive example of a child on a swing. For any driven harmonic resonator the amplitude displays a Lorentzian curve shape with the maximum at the system's resonance frequency. The width of the curve is dictated by the system damping. At frequencies far below the resonator's natural frequency, the displacement follows (is in phase with) the driving force. Increasing the frequency to fulfil the resonance condition the driving force and the displacement are 90° out of phase. Further increasing the frequency above the resonance, the amplitude drops to zero and the driving force and object's response are completely out of phase.

amplitude and phase in relation to the resonance frequency for a general driven harmonic oscillator. In fact, this simple model can be generalised to encompass the qualitative behaviour of most resonances and is helpful to keep in mind when discussing the physics in this thesis.

As it turns out, visible light is optimally suited to excite resonances in nanostructured matter with at least one size scale being ∼100-1000 nanometers. This is something that Nature figured out long before scientists did and vivid structural colours of animals and plants are the result of diffractive and interference resonance effects [58–60]. In research, these occurrences are studied in the field of nano-optics where strongly enhanced light-matter interactions in nanoparticles have gained ample attention [5]. In this chapter, some such resonances relevant to the work performed in this thesis will be introduced in further detail, but before that a brief introduction to basic light-matter interaction is appropriate. For more extended treatments of subject matter, see [1, 4, 61].

2.1 Optical properties of matter

A single atom has orbitals that are separated into discrete energy levels. As multiple atoms join into a bulk solid, these energy levels merge to form continuous bands of allowed energy states for electrons. The band structure and the location of its valence and conduction bands determines the optical properties of a material and whether is is a metal, semiconductor, or insulator. As a photon of light carrying an energy of $E = \hbar\omega$ impinges on a material, it can deposit its energy to an electron in the valence band, which reaches the conduction band and forms an electron-hole pair. The sum of all allowed such transitions will then result in the absorption spectrum of the particular material, from which the optical properties of the material can be understood. Compared to the momentum of electrons, the momentum carried by visible light ($k = \frac{2\pi}{\lambda}$) is negligible. Therefore, in an isotropic medium only the photon's energy is relevant and the resulting transitions associated with optical processes are nearly vertical along k in the energy-momentum diagram. While playing a negligible role for a material's optical properties, the photon's momentum is nevertheless non-zero, which leads to substantial mechanical effects attributed to momentum exchange between light and matter as discussed in coming chapters of the thesis.

The quantum mechanical interpretation of materials and their interaction with light is, despite being a more complete model, not necessary within the context of this thesis. Rather, classical electrodynamics suffices to explain the phenomena studied. Thus, we now set out to understand the optical properties of matter from a classical starting point: When an electric field $\mathbf{E}$ interacts with matter it will displace the charged particles in this material, effectively distorting the material and also the electric field itself. The resulting field can be described by the auxiliary displacement field

$$\mathbf{D} = \varepsilon_0 \mathbf{E} + \mathbf{P}. \tag{2.1}$$

Here, $\mathbf{P}$ is the macroscopic polarisation density, which for a linear, homogenous, isotropic and non-magnetic material can be expressed proportionally to the electrical susceptibility χ as

$$\mathbf{P} = \varepsilon_0 \chi \mathbf{E} \quad \Rightarrow \quad \mathbf{D} = \varepsilon \mathbf{E}. \tag{2.2}$$

The implication is reached by introducing a permittivity $\varepsilon = \varepsilon_{\mathrm{r}}\varepsilon_0 = \varepsilon(\chi + 1)$, where ε_{r} is the relative permittivity or the dielectric constant of the material, effectively describing how a material responds to an electric field. Straightforwardly, the larger ε_{r} becomes the more the material interacts with light, and the dielectric constant becomes central in understanding a material's optical response.

The expressions above are for a single wavelength, which is why it is sensible to talk about a dielectric *constant*. However, all materials exhibit dispersion, meaning that their optical response is frequency-dependent. Hence, for broadband illumination one has to introduce a dielectric *function* $\varepsilon_{\mathrm{r}}(\omega)$, which is a complex-valued and frequency-dependent property. Dielectric materials with an approximately negligible absorption have real dielectric functions that tend to be nearly constant at optical frequencies, whereas metals have strongly frequency-dependent dielectric functions with negative real and non-zero imaginary components.

The dielectric function of a material is a quantity that can be indirectly measured experimentally. However, it turns out that we can gain plenty of insight into the optical properties of a material from analysing an analytic, one-dimensional, classical atom model. If the atom is modelled as a positively charged nucleus with an electron around it, an equation of motion for the electron can be written as a driven, damped harmonic oscillator as

$$\ddot{x}(t) + \zeta\dot{x}(t) + \omega_0^2 x(t) = -\frac{e}{m_{\mathrm{e}}}E(x,t). \tag{2.3}$$

Here, m_e is the electron mass, and e its charge. ζ is the characteristic damping frequency, and ω_0 is the resonant frequency of the system. By performing a Fourier transform in terms of angular frequency ω, one can after some reorganisation reach an expression for the dipolar polarisation density as

$$P(\omega) = \frac{Ne^2/m_e}{\omega_0^2 - \omega^2 - \mathrm{i}\zeta\omega}E(\omega), \tag{2.4}$$

with N being the electron density. Assuming a homogeneous and isotropic material as in Equation (2.2), an expression for the dielectric function can be written as

$$\varepsilon_{\mathrm{r}}(\omega) = 1 + \frac{\omega_p^2}{\omega_0^2 - \omega^2 - \mathrm{i}\zeta\omega}\ , \tag{2.5}$$

where $\omega_p = \sqrt{Ne^2/m_e\varepsilon_0}$ is the plasma frequency. What we have arrived at is the Lorentz model for the relative permittivity of a dielectric material. The first term in Equation (2.5) is the free space response and the second term the material response. To correct for the contribution of positive ion cores to the electric field displacement, this term can be replaced by a correction term, ε_∞ [62].

In the case of a conducting metal, the restoring force term in Equation (2.3) vanishes since the conduction electrons are not bound to the nuclei ($\omega_0 = 0$). Hence, the derivation above can be repeated, resulting in

$$\varepsilon_{\mathrm{r}}(\omega) = \varepsilon_\infty - \frac{\omega_p^2}{\omega^2 + \mathrm{i}\zeta\omega}\ , \tag{2.6}$$

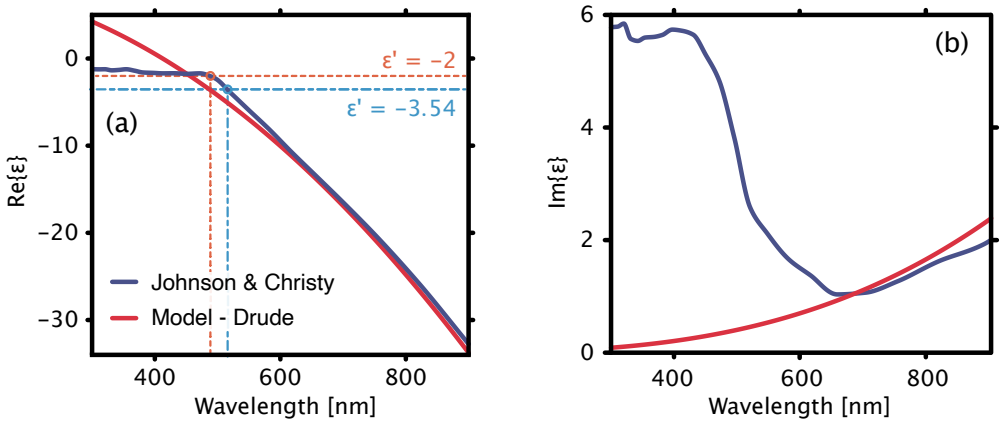

FIGURE 2.2: Real (a) and imaginary (b) parts of the dielectric function for gold from the Drude model, calculated for an electron density of $5.9 \cdot 10^{28}\mathrm{m}^{-3}$, $\varepsilon_\infty = 9$, and carrier relaxation time of $\tau = 27.3$ fs [63], compared to the one experimentally measured by Johnson and Christy [64]. In particular, note the good agreement in the visible red and NIR spectrum, and the discrepancy that becomes apparent at shorter wavelengths, especially for Im$\{\varepsilon\}$ due to interband transitions in the metal.

which is the Drude model of relative permittivity for metals. In this case, N is rather the density of free electrons, and the damping rate can be written as $\zeta = \frac{1}{\tau}$ where τ is the mean carrier relaxation time. Due to its high conductivity as well as its chemical inertness, gold holds a special place in nano-optics, as we will see later. By using the Drude model of Equation 2.6, the overall shape of the dielectric function of gold, and hence its optical response, is well captured by this simple approximation, as seen in Figure 2.2. Unfortunately, this simple model does not predict the optically induced transitions between the valence and conduction band often referred to as interband or d-band transitions, which enhance absorption below a wavelength of 600 nm. The discrepancy is seen most clearly for Im$\{\varepsilon\}$ in Figure 2.2b.

We have now arrived at the complex-valued dielectric function for dielectric and metallic materials, which for Maxwell's equations is an important property. However, a physically more intuitive parameter to describe the optical properties of, especially dielectric, materials is the refractive index. The complex refractive index is related to the dielectric function as

$$\sqrt{\varepsilon_\mathrm{r}} = \tilde{n} = n + i\kappa, \tag{2.7}$$

again under the assumption that no magnetic response is present. Here, n is the ordinary refractive index that compared to free space scales e.g. the phase velocity ($c = \frac{c_0}{n}$) and wavelength ($\lambda = \frac{\lambda_0}{n}$) of a wave as it propagates through a medium. κ is the attenuation coefficient, describing the amount of loss that the wave experiences upon propagation. If the attenuation has no position-dependence, the intensity of a wave as it propagates through a medium decays according to the Beer-Lambert law as $I(z) = I_0 \mathrm{e}^{-2k_0\kappa z} = I_0 \mathrm{e}^{-\mu z}$, where $k_0 = \frac{2\pi}{\lambda_0}$ is the free space wavenumber and $\mu = -2k_0\kappa$ is the absorption coefficient.

Silicon is among the most prevalent dielectric materials in science and engineering. Below, it will be discussed in the context of nano-optics. Its complex refractive index is well described by a single Lorentz oscillator model in the visible to near-infrared (NIR) wavelength regime (Figure 2.3). Outside of this spectral band, the single-termed model departs from reality. In fact, real materials have multiple resonance

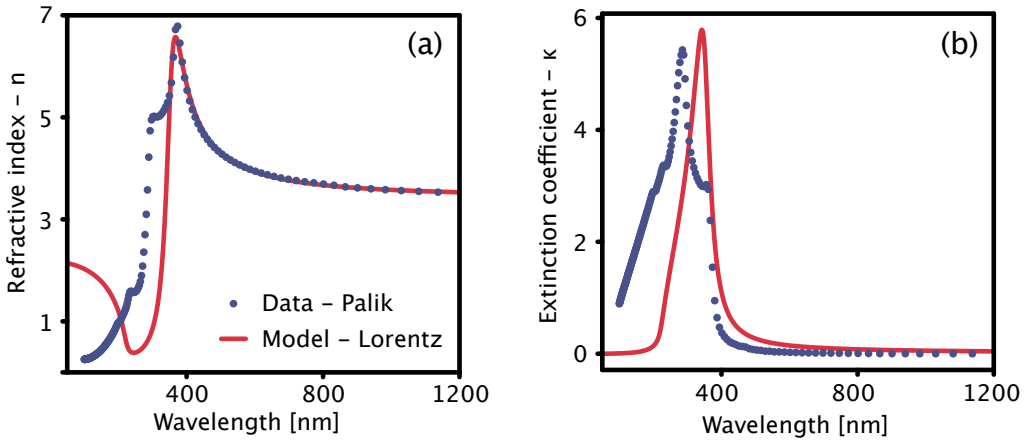

FIGURE 2.3: Refractive index (a) and extinction coefficient (b) for silicon, calculated from the Lorentz model, compared to experimentally measured ones [66]. For the model a plasma frequency of 1979 THz ($\lambda = 152$ nm), a resonance frequency of 835 THz ($\lambda = 359$ nm), a characteristic damping ratio of 0.02, and $\varepsilon_\infty = 6.7$ was used. A single Lorentz oscillator model predicts the optical properties well in the visible to NIR wavelengths – the spectral range relevant for the work performed in this thesis. For a model to agree over a wider wavelength band one can use a sum of Lorentz oscillators.

modes, all of which are more complex than a dipolar electron oscillator and all add to the material's optical response. Yet, all of these resonances can be approximated by a Lorentzian model, and a more accurate refractive index can be obtained by summing multiple Lorentz oscillators [65].

Finally, a few observations that can be drawn from the general shape of the Lorentz oscillator model for dielectric function and refractive index:

- Near resonance, strongly enhanced optical interactions occur and the index of refraction (Figure 2.3a) is high. However, the absorption (Figure 2.3b) in a resonantly excited material concomitantly becomes high, whereas far from resonance absorption is usually negligible.
- As the wavelength increases (frequency decreases), n and $\mathrm{Re}\{\varepsilon_\mathrm{r}\}$ are for the most part decreasing. This is referred to as normal dispersion and gives rise to e.g. the well-known tendency of prisms to refract blue light more than red. However, around the resonance wavelength dispersion is reversed (anomalous) and a prism would instead bend long wavelength more than short ones.
- The refractive index and attenuation coefficient (as well as the real and imaginary part of the dielectric constant) are intimately connected and the equations impose constraints on physically realisable combinations of the two. The formal way of describing this is by saying that the two properties are Kramers-Kronig related.

2.2 Light-matter interactions of subwavelength particles

To understand light-matter interactions, above we worked our way from the fundamental electric displacement field, via the dielectric function, to the more physically intuitive refractive index and attenuation coefficient of a material. On the macroscopic scale, these are sufficient to describe the propagation of light in

and between media, as these are the properties used in the Fresnel equations to describe reflection and refraction, as well as in the Beer-Lamberts law to describe attenuation upon propagation [1]. This is also the domain of our everyday experiences of optics – reflection from a lake, a colour spectrum in a rainbow, or the shiny appearance of a metal. However, both these equations and our intuition become inadequate as the size of matter shrinks towards the nanoscale and become comparable to the wavelength of light. Much like the treatment of atoms and molecules, it here rather becomes relevant to describe light-matter interactions in terms of scattering and absorption [61].

From a fundamental standpoint, any electromagnetic radiation arises from oscillatory electric charges. As an incident electromagnetic wave interacts with matter it displaces charge within that material. Such charge displacements will in turn give rise to secondary electromagnetic radiation, which becomes the scattered light. The shape and size of the particle, its material properties, and the medium in which it resides, together with the angular, intensity, and polarisation characteristics of the incident light all contribute to the resulting scattering and absorption. For the general case, this is undeniably a daunting problem.

For arbitrary particles with complex shapes and without clear symmetry, no analytical solutions to describe the scattering and absorption are possible and the community instead relies on numerical simulations to estimate their optical response. Such numerical methods are plentiful, and grid-based approaches like finite difference time domain (FDTD), discrete dipole approximation (DDA), finite element methods (FEM), and boundary element methods (BEM) allow for simulation of any arbitrary geometry. These rely on being able to divide a nanoparticle into small domains and solving Maxwell's equations numerically in the time or frequency domain [67].

Nevertheless, for homogenous spherical particles there exists an analytical solution to the scattering problem. By solving Maxwell's equations in spherical coordinates one can obtain converging infinite series of vector spherical harmonics that describe the electromagnetic field at any point. This was found by Gustav Mie in 1908 [68] and is now referred to as Mie theory [61]. At the time of G. Mie, using these solutions must have been cumbersome, since several multipoles need to be summed to reach sufficient accuracy. Today though, as computational capacity has exponentially increased, Mie theory has become a valuable tool for nano-optics research.

While being a powerful computational method, it remains challenging to gain intuitive physical insights about the sphere's optical properties and interactions from the Mie multipole sums. Hence, to reach some physically intuitive insights about the light-matter interactions of subwavelength particles we will yet again turn to a simplified model system.

2.2.1 Quasi-static approximation

If a particle is sufficiently small, i.e. much smaller than the wavelength of light, the charge displacement and consequently the scattered field will follow that of an electric dipole. Hence, the optical interaction can be adequately described solely by the particle's induced electric dipole moment and any spatial variations of the field within the particle can be neglected [61]. For visible wavelengths, such approximations can be regarded as accurate for objects with dimensions below 30

nm. It is possible to expand the model to include slightly larger particles (<100 nm) if retardation effects from radiative damping as the particle's size increases and size-induced depolarisation from emission at different points in the particle is taken into account. These retardation effects are captured in the modified long-wavelength approximation (MLWA) [69, 70].

Spherical case

The simplest case to consider is a small isotropic homogeneous sphere of radius r_0 with the dielectric function $\varepsilon_{\mathrm{r}}(\omega)$ that is located in an isotropic and non-absorbing medium with the dielectric constant ε_{m}. By solving the Laplace equation for the electrostatic case and applying appropriate boundary conditions (details outlined in [4]) the induced dipole moment by a driving electric field $\mathbf{E}$ for the sphere is found to be

$$\mathbf{p} = 4\pi\varepsilon_0\varepsilon_{\mathrm{m}} r_0^3 \frac{\varepsilon_{\mathrm{r}}(\omega) - \varepsilon_{\mathrm{m}}}{\varepsilon_{\mathrm{r}}(\omega) + 2\varepsilon_{\mathrm{m}}}\mathbf{E} = \varepsilon_0\varepsilon_{\mathrm{m}}\alpha(\omega)\mathbf{E}, \tag{2.8}$$

where $\alpha = 4\pi r_0^3 \frac{\varepsilon_{\mathrm{r}}(\omega)-\varepsilon_{\mathrm{m}}}{\varepsilon_{\mathrm{r}}(\omega)+2\varepsilon_{\mathrm{m}}}$ is defined as the electric dipole polarisability of the sphere. From the functional form of $\alpha(\omega)$ one realises that a resonant enhancement occurs as $\varepsilon_{\mathrm{r}}(\omega) \to -2\varepsilon_{\mathrm{m}}$ for a certain ω, i.e. where the real part of the dielectric function of the particle's material equals -2 times the dielectric constant of the environment.

Spheroidal case

Apart from spherical particles, the two most common shapes used within nano-optic research are rod- and disk-shaped objects. Within the quasi-static approximation, these shapes can be approximated with prolate and oblate spheroids (cigar and disk shapes), respectively. Since these rotationally symmetric objects have three principal axis a_1, a_2, and a_3, where two are of equal size ($a_1 > a_2 = a_3$ for prolate and $a_1 = a_2 < a_3$ for oblate spheroids) , they support two unique dipolar resonance modes that depending on the size and material parameters of the object will appear at two different wavelengths. Expressions for polarisabilities along each separate axis ($i = 1, 2, 3$) of the spheroids, representing the separate dipolar modes are then expressed as [61]

$$\alpha_{\mathrm{i}}(\omega) = \frac{4\pi a_1 a_2 a_3}{3} \frac{\varepsilon_{\mathrm{r}}(\omega) - \varepsilon_{\mathrm{m}}}{\varepsilon_{\mathrm{m}} + \mathcal{D}_i(\varepsilon_{\mathrm{r}}(\omega) - \varepsilon_{\mathrm{m}})}, \tag{2.9}$$

where $\mathcal{D}_i$ are geometrical factors for each principal directions of the ellipsoid. These are obtained by

$$\mathcal{D}_i = \frac{a_1 a_2 a_3}{2} \int_0^\infty \frac{1}{(a_i^2 + q)\left(\prod_i \sqrt{a_i^2 + q}\right)} \mathrm{d}q. \tag{2.10}$$

For any ellipsoid the geometrical factors for the three axis must sum to 1 ($\mathcal{D}_1 + \mathcal{D}_2 + \mathcal{D}_3 = 1$). Furthermore, a sphere has three equal axis and hence $\mathcal{D}_{1,2,3} = \frac{1}{3}$, resulting in Equation (2.9) reducing to the spherical case of (2.8). In the extreme case of a flat disk or a thin needle, $\mathcal{D}_1$ approaches 0 monotonically. The resonance condition when the denominator of Equation (2.9) approaches 0 occurs when $\varepsilon_{\mathrm{r}}(\omega) \to -\frac{(1-\mathcal{D}_i)}{\mathcal{D}_i}\varepsilon_{\mathrm{m}}$. This implies that for a material with normal dispersion,

as the long axis of the ellipsoid grows, the resonance excitation along this axis will shift towards longer wavelengths.

For anisotropic particles, it is useful to construct a three-dimensional tensor containing the polarisabilities of the three separate axes. As the axes of the spheroid are aligned with the Cartesian coordinate axes, the polarisability tensor will be diagonal. The polarisability tensor can further be decomposed into a real and imaginary part according to $\boldsymbol{\alpha} = \boldsymbol{\alpha}' + \mathrm{i} \cdot \boldsymbol{\alpha}''$.

2.2.2 Scattering and absorption

After this discussion, we are ready to approach the core of light-matter interactions with subwavelength particles, namely how they scatter and absorb light. Let us consider a thought experiment (Figure 2.4) where a beam of light travels unimpeded from a source to a detector that registers an electromagnetic energy of U_0. When placing a subwavelength particle in the light beam the detector would register an energy $U < U_0$, where some energy has been *extinguished* by the particle. Some of the energy will have been *scattered* by the particle in directions not collectable by the detector. Under the assumption that the experiment is taking place in a non-absorptive medium, the rest of the lost energy can be accounted for by *absorption* in the particle.

Hence, the nanoparticle will distort the oscillating electromagnetic field surrounding it. By placing the nanoparticle within a closed surface $\mathcal{S}$ one can find the net rate at which electromagnetic energy W crosses the boundary according to

$$W = \int_{\mathcal{S}} \mathbf{S} \cdot \hat{\mathbf{n}} \, \mathrm{d}\mathcal{S}. \tag{2.11}$$

At any point on the surface, $\hat{\mathbf{n}}$ denotes the vector normal to $\mathcal{S}$, whereas $\mathbf{S} = \mathbf{E} \times \mathbf{H}$ is the Poynting vector, describing the directional energy flux in terms of the electric and magnetic fields. The fields can be decomposed into an incident, a scattering,

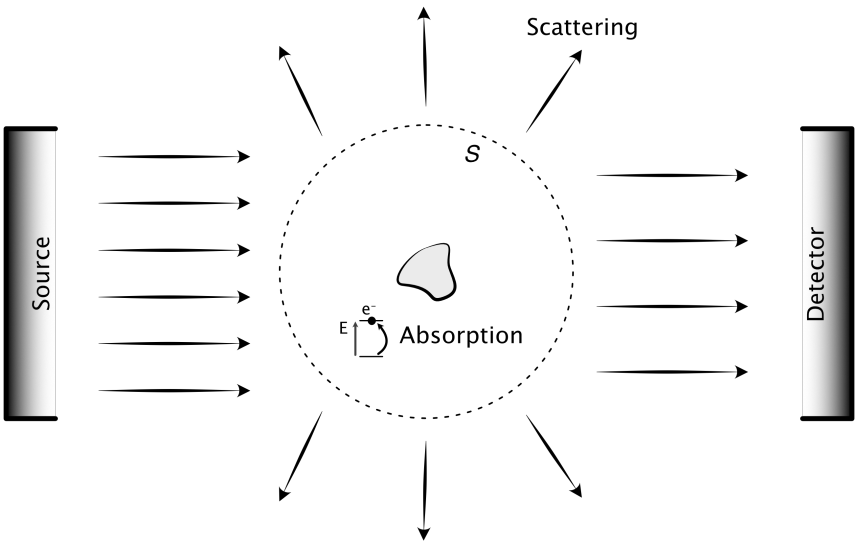

FIGURE 2.4: Extinction of an arbitrary subwavelength particle. The collected energy is less than the incident one, which is accounted for by scattering and absorption from the particle. By enclosing the particle ($\mathcal{S}$, dashed circle) and analysing the fields on this closed surface, the scattered and absorbed fields can be extracted.

and an absorbed component, and hence the total energy flow can be written as a sum of said components, whereas the extinguished energy is obtained as the sum of the scattering and absorbed energies.

By then taking the ratio between the energy for scattering, absorption, or extinction and the incident power density, a measure for the efficiency of this mode of light-matter interaction is obtained. Such a ratio, i.e. $\sigma_{\text{scatt}} = \frac{W_{\text{scatt}}}{I_{\text{inc}}}$, has the dimension of area and is therefore referred to as a cross section. This is a useful value since it can be compared to experimentally measurable properties such as a nanoparticle's dark-field scattering spectrum, the transmission through an array of nanoparticles, or the absorption leading to photothermal heating, all of which play central parts in this thesis. Interestingly, when a particle is resonantly excited its optical cross section can vastly exceed its geometric counterpart.

Thus, our daunting problem boils down to expressing the full electromagnetic fields in and around the particle as it interacts with incoming light. For arbitrarily complex particles and geometries, the numerical methods mentioned above (FDTD, FEM, DDA, etc.) are routinely used. For spherically symmetric objects the analytical Mie theory provides solutions, and under the quasi-static approximation the cross sections can be derived as

$$\sigma_{\text{scat}} = \frac{k^4}{6\pi} |\alpha(\omega)|^2, \qquad (2.12) \qquad \sigma_{\text{ext}} = k\text{Im}\{\alpha(\omega)\}, \qquad (2.13)$$

by integrating the time-averaged field from a point dipole as it is excited by an oscillating plane wave. Here $k = \frac{2\pi n_{\text{m}}}{\lambda_0}$, and n_{m} is the refractive index of the medium [61]. From these two equations, one can also calculate the absorption cross section as $\sigma_{\text{abs}} = \sigma_{\text{ext}} - \sigma_{\text{scat}}$.

Finally, to experimentally measure the optical cross sections and properties of individual subwavelength particles can be challenging. A technique called quadriwave lateral shearing interferometry (QLSI) which has previously been used for phase imaging microscopy in nano-photonics [71–73] was in **Paper S.XII** proposed as a convenient and reliable approach. With this technique, the generalised polarisability of an arbitrary nanoparticle can be measured and used to extract all the optical cross sections. To exemplify this, Figure 2.5 demonstrates the polarisability of individual anisotropic gold nanorods measured by the technique, however also nanospheres of gold and polystyrene were studied.

2.3 Resonances in metal nanoparticles

It turns out that the optical properties of noble metals are well suited for distinct light-matter interactions, mediated by so-called *plasmons*. In general, a plasmon is the collective oscillation of conduction electrons in a material, excited by an electromagnetic field. The oscillation will be resonantly driven when the frequency of the incoming light matches a condition set by the material's properties, its shape, and surroundings. The plasmon family has three members, where the first is the bulk plasmon. This is the collective electron oscillation in the bulk of a material, as seen in the free electron model above. The second type, the surface plasmon polariton resonance, exists on interfaces between a plasmonic material and a dielectric. Albeit the most studied and commercialised type of plasmonic effect [4, 75, 76], it will not be further discussed in this thesis. Rather, we are interested in the last member of the plasmon family; the localised surface plasmon

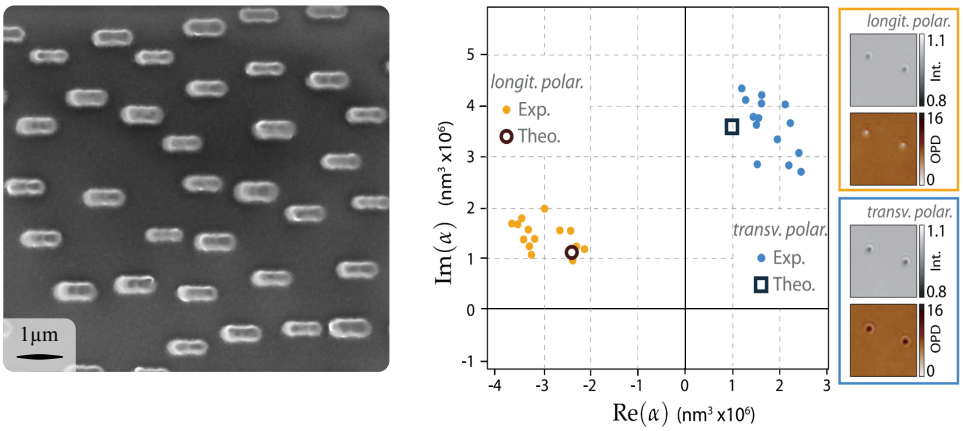

FIGURE 2.5: The QLSI technique applied for full optical characterisation of nanoparticles. Left: An SEM image of fabricated gold nanorods. Right: Experimentally measured polarisabilities for the two principal axis (longitudinal - orange, and transverse - blue) of the nanorod, compared to a DDA simulation of the nominal nanorod. Insets to the right show the intensity and phase images used to extract the polarisability values. The right subfigure is adapted with permission from [74] ©2020 The Optical Society.

(LSP) resonance. This arises when all three dimensions of a noble metal structure are reduced to the nanoscale. As this resonance occurs, which for gold and silver nanoparticles typically happen in the visible part of the electromagnetic spectrum, scattering and absorption are significantly enhanced. Throughout the last decades these strengthened optical interaction has lead to a wealth of valuable and useful findings [77–80], with plenty of promising areas left to explore further [81, 82].

Quantum mechanically, a plasmon is the quantisation of the collective electron oscillation in the form of a quasiparticle. How the plasmon quasiparticle interacts with its surrounding and other quasiparticles (photons, excitons, phonons, etc.) determines the resulting optical interaction. As plasmons in a nanoparticle are excited they immediately face a multitude of possible decay channels that can be both radiative and non-radiative [80, 83]. The time-line for this decay of the plasmon is summarised in Figure 2.6. Radiative damping inevitably occurs from $t = 0$ as re-emission of photons due to the accelerated charge within the particle. During the first ∼100 fs some plasmons will non-radiatively decay via Landau

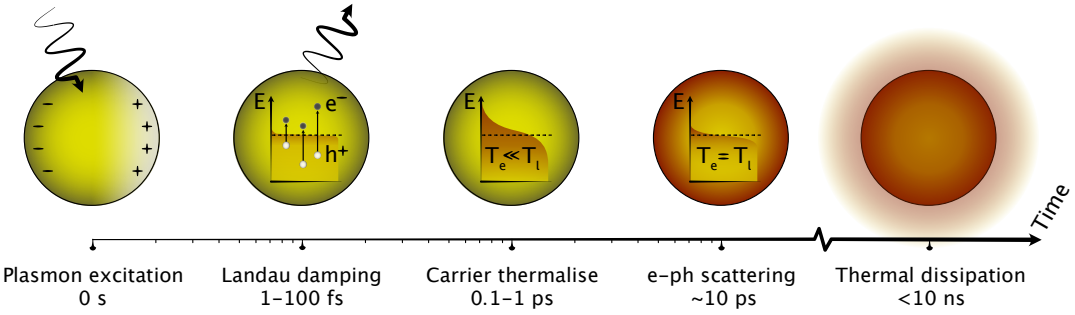

FIGURE 2.6: The fate of the plasmon from excitation to decay. A plasmon is excited at $t = 0$. Immediately decay ensues, via radiative decay due to oscillating charges and Landau damping where hot electron-hole pairs form. These hot carriers thermalise with the carrier bath via electron-electron scattering and subsequently electron-phonon scattering extends the thermal increase to the lattice. Lastly, heat transfer from the nanoparticle to the surrounding complete the non-radiative decay chain.

damping into energetic electron-hole pairs. Some of these excitons will decay radiatively and reemit photons in the form of luminescence, while the so-called *hot* carriers will during the subsequent picosecond or so thermalise with the normal carriers to form a quasi-equilibrium carrier distribution, with an effective temperature well above the lattice temperature. In the picoseconds to come, electron-phonon scattering equilibrates this elevated carrier temperature by heat transfer into the lattice. Lastly, on timescales up to nanoseconds, phonon-phonon interaction allows the increased temperature to dissipate into the surrounding media. For the research performed for this thesis the quantum picture of the plasmon and its decay is for the most part redundant and is not discussed further. However, it should be noted that it is a central topic in plasmonics that has enabled e.g. enhanced photocatalysis, photodetectors, and energy harvesting in solar cells [83].

Phenomenologically, the LSP resonance can be understood even from the Lorentz oscillator and quasi-static models discussed above (Section 2.1 and 2.2.1) since the dielectric functions of noble metals are such that they fulfil the resonance condition in Equations (2.8) and (2.9) at visible wavelengths. Furthermore, since noble metals present strong dispersion in the visible spectrum, the LSP resonance positions become very sensitive to the surrounding dielectric environment. Since $\mathrm{Re}\{\varepsilon(\omega)\}$ is a decreasing function with increasing λ, the LSP resonance redshifts as the refractive index of the surrounding medium increases. This is illustrated in Figure 2.2a by the lines where the gold dielectric constant fulfils the resonance condition for a spherical nanoparticle residing in air and water. In fact, to use the highly refractive index sensitive LSPR position as a sensor is one of the most investigated applications of LSP resonant particles [78].

Moreover, the localised surface plasmon resonance behaviour is strongly dependent on the shape of the resonant particle. For a small nanosphere that can accurately be represented by a point dipole, only a dipolar resonance is excited as predicted by the quasi-static model above (Figure 2.7a), whereas larger nanospheres can support higher-order modes, e.g. quadrupolar as in the one seen in Figure 2.7b[1]. For anisotropic nanoparticles such as nanorods, the single spherical resonance is split into separate resonance modes. These modes are corresponding to resonant excitations of the free electrons in the longitudinal or transverse direction of the rod (Figure 2.7c,d).

A nanoparticle's optical cross sections can at this point be calculated to spectrally resolve the resonant effects. Using an experimentally measured dielectric function for gold [64], the extinction cross section in the quasi-static approximation for gold spheres of increasing diameter (Figure 2.8a) and gold rods of fixed diameter and increasing length (Figure 2.8b) are calculated using Equations (2.12) and (2.13). For the spherical case, the LSP resonance position is seen to redshift and broaden with particle size. For the nanorod, two separate plasmon modes are observed. One at around 525 nm corresponding to the transverse resonance and one that is red-shifted and depends on the particle's aspect ratio, which corresponds to the longitudinal oscillation. The red-shift arises due to the increased separation between the surface charges on either end of the rod, which reduces the restoring force and hence the energy of the resonance.

[1]The asymmetry in the electric field distribution stems from retardation effects, which are not captured in the quasi-static approximation discussed in Section 2.2.1.

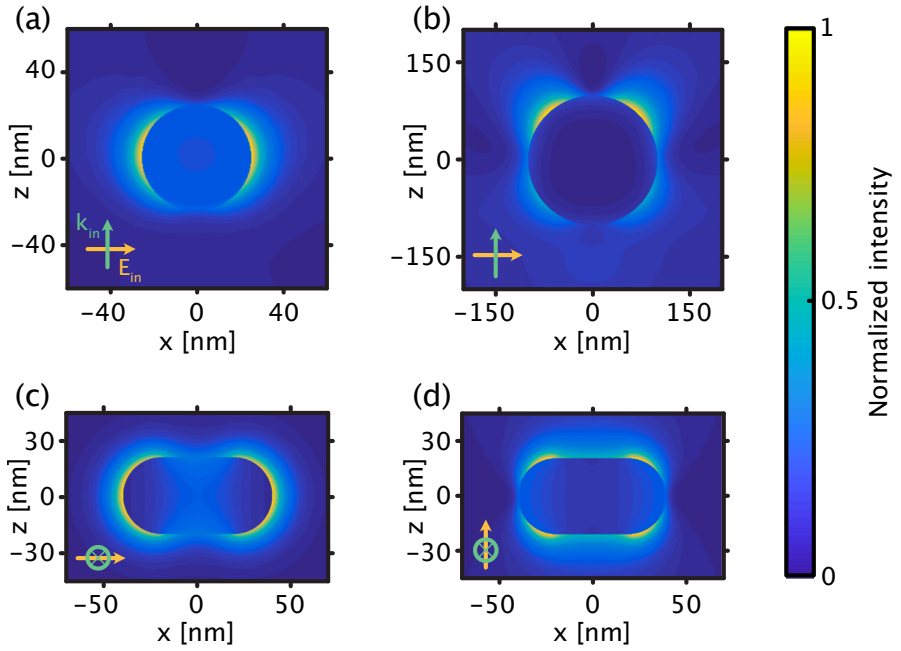

FIGURE 2.7: Electric field intensities from FEM simulations of gold nanoparticles placed in vacuum and excited by plane waves. The electric field intensities are normalised to their maximum values. Arrows indicate the direction of propagation (green), and polarisation (yellow) of light. When the frequency of the field matches the LSP resonance frequency, a collective electron oscillation is induced. (a) A spherical particle of $r = 25$ nm excited at $\lambda = 525$ nm, where the dipolar mode dominates. (b) A spherical particle of $r = 100$ nm excited at $\lambda = 560$ nm, where the quadrupolar mode is dominant. (c), (d) A nanorod of dimensions 40x80 nm excited with light polarised along the longitudinal (c, $\lambda = 612$ nm) and transverse (d, $\lambda = 525$ nm) direction.

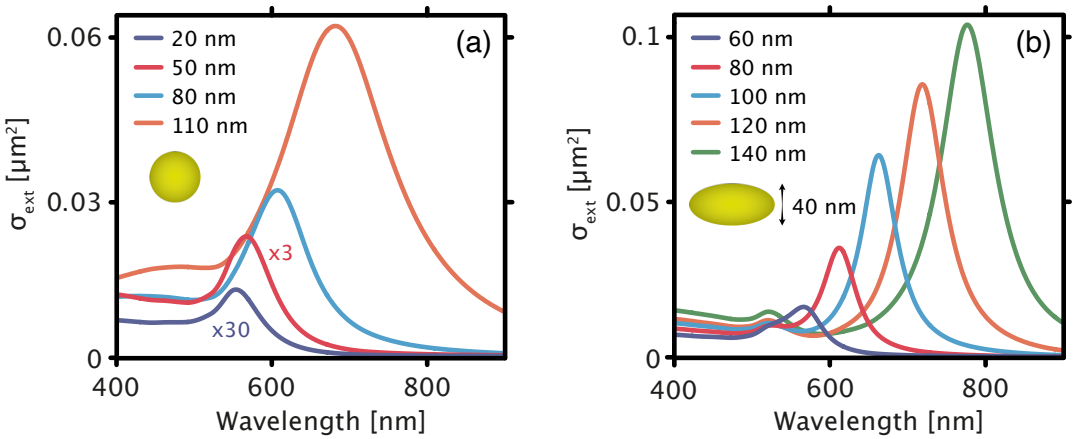

FIGURE 2.8: Extinction cross section spectra of gold nanoparticles when placed in vacuum and illuminated by an unpolarised plane wave. The calculations are performed using the quasi-static approximation with applied MLWA corrections for (a) spherical particles as their diameter increase, and (b) spheroidal nanorods with a fixed width (40 nm) and increasing length.

For all spectra in Figure 2.8, a slight plateau in the extinction is present at shorter wavelengths. At energies above 2.5 eV (∼500 nm) photon energies are sufficient to excite electrons from the d-bands below the Fermi surface to bands above it. These interband transitions lead to increased damping and absorption at blue wavelengths, and often are seen as detrimental. By choosing another plasmonic material one can avoid interband transitions in the visible regime. For example, the band edge wavelength for silver, where interband transitions become allowed, is

located in the UV spectral region [80]. Nevertheless, since they enhance hot electron generation due to Landau damping, some researcher view them as beneficial [83].

2.4 Resonances in dielectric nanoparticles

Although research and development focused on plasmonic nanoparticles have resulted in a plethora of innovations in the last decades, it is not without its drawbacks, e.g. strong Ohmic heating, lack of magnetic response, and CMOS incompatibility. Therefore, partly to complement and partly to supplant plasmonic nanoparticles, the library of resonant nanostructures has been expanded in recent years. The most promising new candidate is that of high-index dielectric (HID) nanoparticles [12, 84].

As compared to the plasmonic resonances that arise from restoring forces on the metal's free surface charges, dielectric nanoparticles present resonances that occur within the nanoparticle and can be classified as *geometric*. Much like a Fabry-Perót resonator where enhancement occurs when the optical path length is a multiple of the cavity length, the lowest energy geometric resonance in an HID nanoparticle occurs when the wavelength of light in the nanoparticle is approximately equal to the particle's diameter ($2r_0 \approx \frac{\lambda_0}{n_{\text{HID}}}$) [12].

The most common choice of material for HID nanostructures is silicon, yet also gallium arsenide, germanium, titanium dioxide and others have been explored [85]. These materials have refractive indices for visible wavelengths in the range $\sim$2-5. Hence, the sizes of resonant HID nanoparticles usually becomes larger than 150 nm. Here, the quasi-static approximation is no longer useful, but Mie solutions to Maxwell's equations become perfectly suited [86]. The Mie solutions allow the internal and scattered fields to be expressed as infinite series of electric and magnetic multipoles where each multipole corresponds to a certain resonance mode [61]. For HID nanoparticles the electric and magnetic multipoles can have comparable strength, as opposed to plasmonic particles where the magnetic contribution to the Mie series is negligible. This endows HID nanoparticles with the potential for optical magnetism, where a material acts magnetic at optical frequencies despite having a vanishingly small permeability[2], as well as a whole new set of resonances that can be explored and exploited [89].

Since the permittivity is positive for dielectrics, the electric fields within HID nanoparticles are not expelled. This results in both linear and circulating electric charge displacements within the nanoparticle, which constitute Mie resonances of both electric and magnetic character [90]. The effect is illustrated in Figure 2.9, where the electric field intensity distributions is displayed for a silicon nanosphere when placed in vacuum and illuminated by a plane wave. At a wavelength of 785 nm, an annulus of high intensity forms within the particle. This corresponds to a circulating current, which from basic electromagnetism we know forms a magnetic dipole. At a wavelength of 585 nm, an electric dipole appears, which is orthogonal to the magnetic one.

[2]This is something that has been sought after with plasmonic nanostructures as well, but due to the limited magnetic contribution for simple shapes, more complex ones such as split-ring resonators [87] and vertical dimer structures [88] have become prevalent since they support circulating electrical currents.

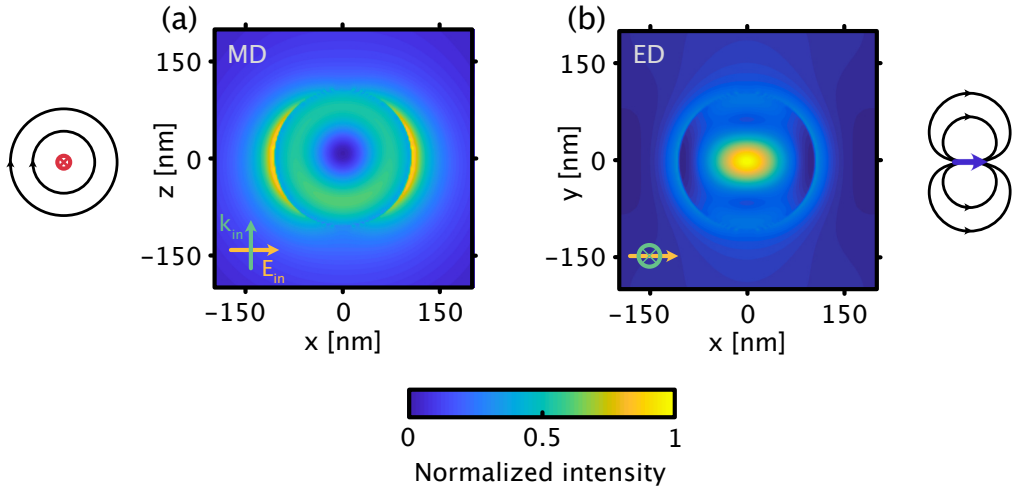

FIGURE 2.9: Electric field intensities from FDTD simulations of a 200 nm diameter crystalline silicon nanosphere placed in vacuum and excited by a plane wave. The electric field intensities are normalised to their maximum values. Arrows indicate the direction of propagation (green), and polarisation (yellow) of light. (a) Intensity distribution at the wavelength of $\lambda = 785$ nm, where the magnetic dipole mode is excited by a circulating current loop. (b) Intensity distribution at the wavelength of $\lambda = 585$ nm, where the electric dipole mode is excited. To the left/right are insets illustrating the characteristic electric field lines for such resonances [89].

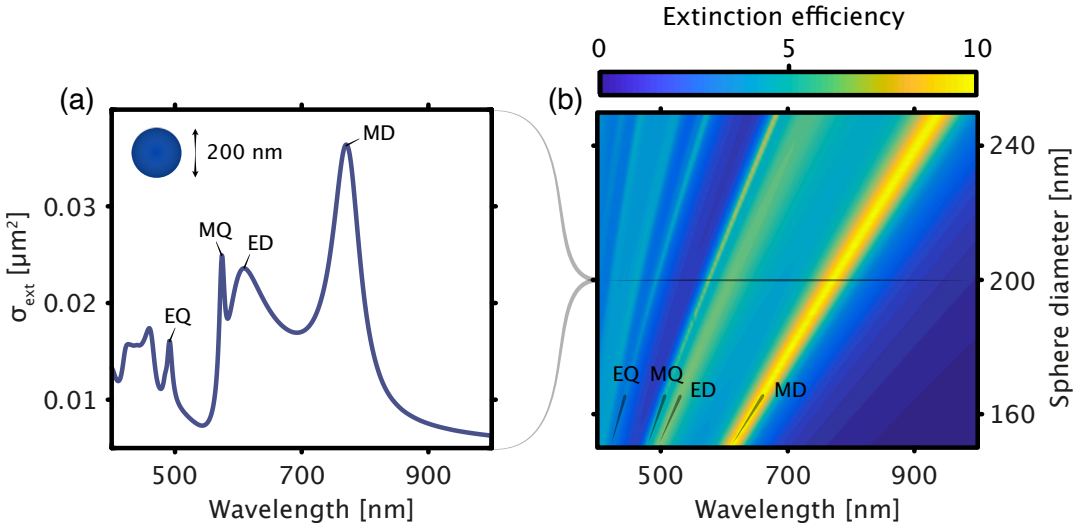

FIGURE 2.10: Extinction spectra of silicon nanospheres when placed in vacuum and illuminated by an unpolarised plane wave. (a) Extinction cross section for a nanosphere with a diameter of 200 nm, calculated by a Mie model [91]. The low-order resonance modes; magnetic and electric dipoles (MD and ED), and quadrupoles (MQ and EQ) all show up as distinct peaks in the spectrum, with the MD mode having the lowest energy. (b) Extinction efficiency for nanospheres with increasing diameter. When increasing sphere size, all modes red-shift proportionally until eventually only higher order modes remain in the visible range.

It is interesting to understand how the complete spectral response of HID nanoparticles behaves. To this end, the extinction spectrum for a 200 nm sphere is calculated using Mie theory (Figure 2.10a). Several resonance peaks appear, where the one with lowest energy is attributed to the magnetic dipolar mode. Then for increasing energy, the electric dipole is followed by magnetic and electric quadrupoles. Further increasing the energy, even higher order resonances form at wavelengths fulfilling the geometrical constraints set by the nanoparticle, as long as they are not extinguished by the increased absorption at shorter wavelengths.

The spectral position of these resonances is linearly dependent on the particle's size, which is obvious when the extinction efficiency spectrum (the ratio between extinction and physical cross sections ($\frac{\sigma_{\text{ext}}}{\pi r_0^2}$) is graphed for a range of different particle sizes (Figure 2.10b). All the modes red-shift as the particle size increases. If the nanoparticle is made sufficiently large, the low-order resonances shift to infrared wavelengths, and the resonances that remain in the visible wavelength band are only higher order modes.

That HID nanoparticles support both types of multipoles make their optical response even richer with potential than their plasmonic counterparts. A magnetic excitation that interacts with an electric one can lead to highly directional scattering patterns when they fulfil the so-called Kerker condition [92, 93]. Furthermore, depending on the shape of the nanoparticle, various modes can be shifted independently [94, 95]. This is strongly contributing to the allure of dielectric nanophotonics since many exotic effects can be realised by controlling and overlapping multiple resonances. Apart from directional scattering from particles meeting Kerker's conditions, interesting effects such as nonradiative anapole modes, unconventional beam steering and nonlinear effects have also been demonstrated [12]. A specific field where dielectric nanophotonics has gained traction in recent years is within the field of optical metasurfaces, which is the topic of the next chapter in this thesis.

2.5 Photothermal effects

As with any resonance, the favourable properties of resonant nanoparticles, come at the price of significant absorption. Due to electron-phonon relaxation, this will lead to enhanced heating and subsequent heat transfer to the environment. Such elevated thermal environments can be problematic in applications, e.g. in biological processes and other temperature-sensitive experiments. For plasmonic nanoparticles this is particularly problematic, because of the high attenuation coefficient of noble metals at visible wavelengths. Therefore, the following discussion will mostly concern them. In recent years turning to resonant high-index dielectric nanoparticles to replace plasmonic ones has been suggested to mitigate these detrimental effects [89]. Nevertheless, in the field of thermoplasmonics they are instead exploited seeing that the plasmonic particle can also be used as a nanoscopic source of heat [96–98]. Below, we introduce the two photothermal effects that stand out as the most important for this thesis, namely the primary effect of heating, and the secondary effect of nanoparticle reshaping.

Moreover, when resonant nanoparticles are submerged in water the heating can be sufficient to nucleate a bubble around them [96]. This occurs after the water has been superheated to temperatures above 200°C and has been seen for both ensembles [99, 100] and individual particles [101, 102]. These systems are interesting from a fundamental perspective, but could also result in some niche applications. For example, in **Papers S.X** and **S.XIII** surface-bound photo-induced nanobubbles were modulated at high speeds and seen to generate flows in the surrounding water with speeds surpassing 4 mm/s. This could potentially be of use to concentrate analytes to sensors or as microfluidic actuators. My colleague Dr. Steven Jones has done an excellent job of summarising this research direction in his recent thesis [103] and hence it is not discussed further here.

2.5.1 Heating

The heat power density generated at a given point in a nanoparticle is determined through Ohmic heating via the electric field intensity at that point. In the case of gold, owing to the considerably high thermal conductivity, the temperature distribution within the nanoparticle can be considered uniform. If such a particle is placed in water, the thermal distribution around it is predominately determined by conductive heat transfer and the thermal conductivity of the water around it. For a sphere in a homogeneous medium under constant illumination, the temperature distribution as a function of radial distance r to the sphere's center can be obtained by solving the steady-state heat equation in spherical coordinates as [96]

$$T(r) = \frac{r_0}{r}\Delta T + T_{\text{amb}}. \tag{2.14}$$

Here, r_0 is the radius of the sphere, and $\Delta T = \frac{\sigma_{\text{abs}} I}{4\pi K r_0}$. I is the intensity of the incoming light and K is the thermal conductivity of the environment. If the particle of interest has a more intricate shape, or if the geometry is not as easily parameterised (e.g. at an interface), more rigorous analysis or even numerical simulations are needed. However, for a range of cases (low aspect ratio nanorods, nanodisks on substrates, etc.) Equation (2.14) provides a valid approximation.

Optical heating of metallic nanoparticles is the most ubiquitous photothermally induced phenomenon in thermoplasmonics. Depending on the overlap between the LSP resonance and the excitation laser, temperature increases of more than 100°C can result (Figure 2.11 from **Paper S.III**). A range of high impact applications based on the effect has been suggested and are currently being studied, including photothermal imaging [104], plasmonic photothermal therapy (PPTT) [105], and heat-assisted magnetic recording [106]. Moreover, studies based on optically confined particles are paving the way for applications using heating effects to enhance chemical reactions [41], in drug delivery applications [107], and molecular transition studies [108], as well as others [35–39].

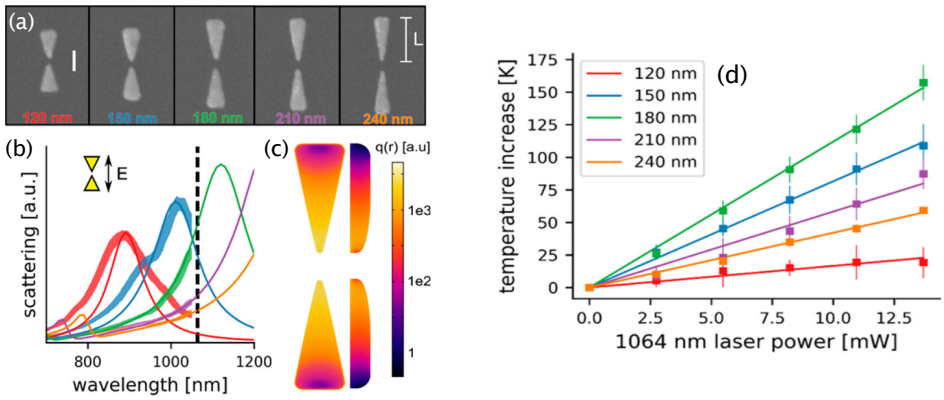

FIGURE 2.11: (a) SEM images of differently sized gold nanoantennas. (b) The simulated and experimentally measured scattering spectra of the nanoantennas, presenting varied interaction with a 1064 nm heating laser. (c) Heat source density for the 180 nm antenna when excited with 1064 nm light. (d) Measured temperature increase during heating laser power build-up, together with linear fits to the data. The temperature increase is seen to scale with spectral overlap at 1064 nm illumination. The figure is adapted with permission from [109] ©2018 American Chemical Society.

2.5.2 Reshaping

Despite being thermally stable up to their melting point in bulk form, the surface atoms of nanoparticles are known to be substantially more mobile than their bulk counterparts [110]. This mobility is further accelerated in a heated environment. Especially for metallic nanostructures, this property leads to continuous reorganisation of the surface atoms. For nanorods, the reorganisation is found to be driven by a curvature induced diffusion process where adatoms migrate from high to low curvature areas [111], resulting in a rod becoming shorter and wider, eventually forming the thermodynamically stable sphere. This is associated with a spectral blueshift since the restoring dipolar force increases when the opposite ends of the rod approach each other.

Rigorous studies of the reshaping of immobilised gold nanorods have been conducted, especially with pulsed laser illumination [112–115]. A few particularly noteworthy examples of applications of pulsed laser reshaping are dense data storage [9], production of ultra-narrow dispersions in colloidal ensembles of nanorods [116], controlled termination of heating during PPTT to prevent harming healthy cells [117], and ultra-flat plasmonic absorbers [118]. Nanoparticles tend to be even more prone to reshaping under continuous wave (CW) illumination where nanorods have been seen to reshape at as low temperatures as 150°C [119]. Just like other forms of thermal reshaping [120, 121], the CW-induced reshaping is a gradual process that can take anywhere from minutes to hours depending on the thermal environment since it is based on adatom diffusion.

During recent years, more unusual nanoparticle reshaping in focused laser beams has been demonstrated [122]. For example, ordinary colloidal nanorods have been seen to bend when illuminated with a diffraction-limited beam [123] and nanospheres have been shown to exhibit polarisation directed growth to nanorods [124]. While performing the experiments presented in **Paper I**, I observed some such counterintuitive reshaping effects (Figure 2.12). When single-crystalline gold nanorods with an average longitudinal LSP resonance at around 750 nm in water were illuminated with a focused 660 nm CW laser (intensity as low as 5 $\mathrm{mW}/\mu\mathrm{m}^2$), atypical spectral characteristics were observed. Some nanorods' spectral peak remained more or less stationary for long periods of time (>5 min), after which it experienced some irreversible change that blueshifted the spectral peak more than 100 nm (Figure 2.12a). By performing correlative SEM imaging before and after the optical experiment, the spectral shift could be attributed to a rapid reshaping event. Other nanorods in the same batch instead presented a gradual redshift of its LSP resonance (Figure 2.12b). Post-experiment SEM investigations then rather reveal a deformed nanorod with a rugged surface.

These reshaping observations would require more investigation to be fully understood, but regardless they allude to the complex and fascinating physics at work with these systems. Exotic reshaping which in some ways resemble the observed results have been seen from optical force-mediated stretching of nanoparticles [125]. Albeit not exactly equivalent, optical forces could play a role in our observations as well, due to our highly focused beam. Furthermore, bubble formation around a nanoparticle drastically reduces the thermal conductivity of the surrounding, which could enable the nanorod to both rapidly reshape into a nanosphere or undergo surface evaporation to gradually deform the surface [126], and could hence be another component in the full explanation.

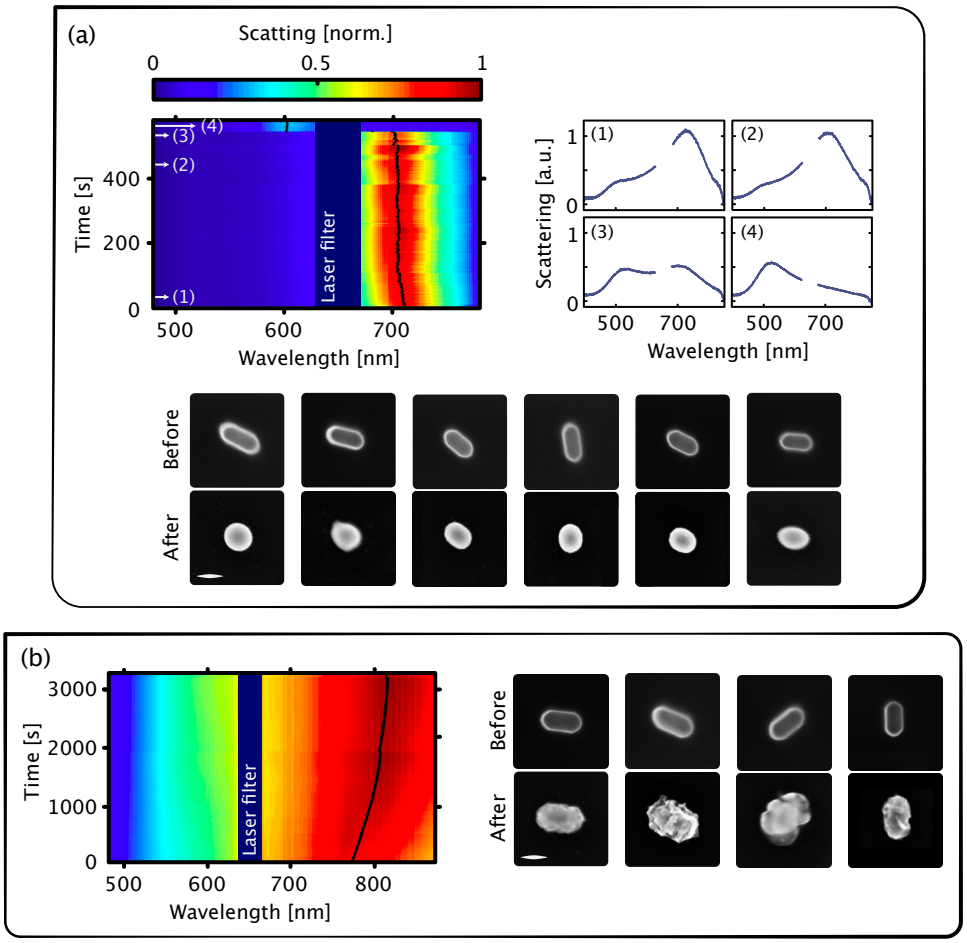

FIGURE 2.12: Abnormal reshaping of single-crystalline gold nanorods, caused by illumination with a focused 660 nm CW laser. (a) Explosive reshaping that transforms a nanorod to a more spherical particle. The particle is stable for several minutes, after which it abruptly changes its morphology to drastically blue-shift the spectral peak. The top-left figure displays time-resolved spectra where the black line marks the peak position. The white numbers (1)-(4) denote times when the spectra to the right are recorded. Before and after the optical experiments, SEM images of individual nanorods are recorded. The spectral shift seems to be explained by a rapid reshaping event. (b) Other particles under the same illumination conditions display slow red-shifts of their LSP resonance peak. This is inconsistent with the expected continuous blue-shift accompanied by photo-induced reshaping towards a sphere. SEM imaging after optical experiments indicates that the rods develop a rough surface.

Chapter 3

Phase-gradient metasurfaces

In the previous chapter interactions between light and matter within nano-optics were introduced. The treatment was then concerned with individual nanostructures that due to resonances in the visible wavelength band presented enhanced optical interaction. However, when many such particles are brought together their interactions and resonances can couple to each other and form further modified effects [127]. Such collective effects, unseen for ordinary materials, are studied within the field of optical metamaterials.

In general, a metamaterial is a man-made material that has been engineered to have some property; optical, acoustic, structural, or other, which cannot be found in naturally occurring materials [128]. The metamaterial that has garnered the most attention from researchers and the general public alike is that of electromagnetic negative-index metamaterials, which allows materials to present a negative refractive index in some wavelength regime and can therefore bend light in the opposite direction compared to ordinary materials [13, 129, 130]. With such negative refraction one could design systems for diffraction-less lenses [14], cloaking [15], and perfect absorbers [131] to mention a few possible applications. Metamaterials are generally constructed by metallic or dielectric elements, often in the form of rings, rods, or split rings, which are arranged in a subwavelength periodic grid in 3D space. Due to the subwavelength spacing, from the light's perspective the metamaterial appears as a continuous medium that can be associated with effective optical properties that can be specifically tailored. Since the size of the constituent elements has to shrink as the wavelength does, fabrication of such materials become increasingly difficult. Hence, most metamaterials have been realised in the terahertz to near-infrared regime [128].

If one imposes the restriction of only placing a single layer of particles, the 2D equivalent to a metamaterial is obtained, which is referred to as a *metasurface*. Turning to metasurfaces has granted entry to the visible wavelength regime by circumventing the two main drawbacks of metamaterials, namely (1) that the elements constituting the metamaterial become increasingly lossy in visible wavelengths, and (2) that fabrication of nanoscopic 3D structures is challenging [132]. Metasurfaces has for the last 20 years been a popular research area from which a wealth of fundamental results as well as applications have emanated. Many of these findings have been beautifully summarised in review articles [16, 84, 133, 134]. The particular type of metasurfaces studied in this thesis are termed *phase-gradient metasurfaces* and will be introduced in this chapter.

3.1 Wavefront curvature and phase profiles

From fundamental optics, the most basic three-dimensional propagating electromagnetic wave is the plane wave [1]. As it propagates its profile is unchanged and its wavefronts, defined as the surfaces of constant phase, remain planar. For any other wavefront moving through a homogenous medium, the wavefront will either diverge or converge. In this respect, how a light wave is propagating is determined solely by the curvature of the wavefronts (planes of constant phase), or by the phase profile in any Cartesian plane, assuming that the total amplitude of the wave is constant and unchanging.

Hence, any optical element (e.g. a lens, axicon, or waveplate) placed in the beam path can be described as a phase modulation object. The simplest such case is the transmission of a plane wave that arrives at an angle to the interface between two materials of different optical thickness. From Snell's law, we know that such a light beam will bend towards the surface normal. In the wavefront/phase picture, this can be understood simply as changing the angle of the wavefronts, or equivalently the slope of the linear phase profile projected onto the plane of the interface.

To fully grasp the relationship between the wavefront curvature and in-plane phase profiles, let us visualise the working of a lens, as in Figure 3.1. A plane wave strikes a lens, and its wavefronts are converted to spherical wavefronts and generate a focus a certain distance away. If the phase profile was recorded at the boundary of the lens (dashed line in Figure 3.1), a rotationally symmetric paraboloid phase profile would be found, as described by $\phi(r,\lambda) = \frac{2\pi}{\lambda}\left(\sqrt{r^2+f^2}-f\right)$, where λ is the wavelength of light, r is the radial distance from the optical axis, and f is the focal length of the lens [135, 136]. This relation is found by calculating the optical path length required to translate a plane wave to a spherical wave with the radius of curvature of f, as a function of distance from the optical axis. The phase wrapping

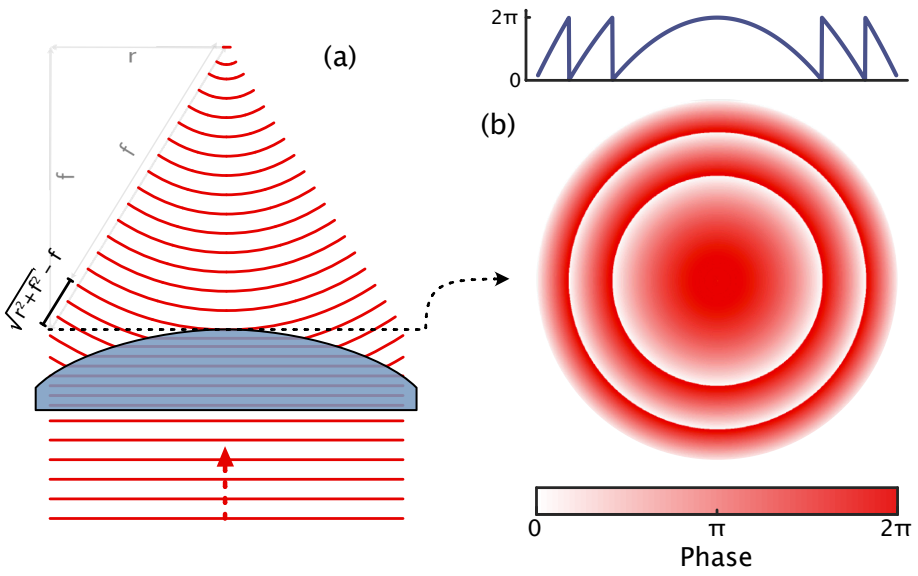

FIGURE 3.1: The relation between wavefront curvature, phase profiles and beam propagation. (a) Illustration of how the wavefronts of a plane wave are curved by a lens to obtain focusing. The solid red lines in the left figure represent planes of constant phase. If a plane cut is taken orthogonal to the optical axis just after the lens, the radial phase profile in that plane is a paraboloid, which in wrapped phase is presented in (b). Above the 2D plane is also a radially symmetrical plane cut of the phase profile of the lens at this plane.

(modulation of 2π) can be understood as when the subsequent wavefront crosses the cut-plane.

Once projected in one dimension as in the top right inset of Figure 3.1, the general shape of the phase profile might bring to mind optical elements such as Fresnel lenses [137] and kinoform diffractive lenses [138, 139]. Indeed, these derive their function from surfaces engineered to impart a desired phase profile to the incoming wavefronts by removing redundant full multiples of 2π phase delay compared to refractive lenses. In many ways, the study of these optical elements is the predecessor to the vast body of research that the rest of this chapter will introduce.

Lastly, let us note that in fact for any arbitrary object interacting with light, the light field (intensity distribution and wavefronts) will be distorted from a simple plane wave and contain the information about the scene. Upon propagation through our eye or some other well-designed optical system, these wavefronts are translated to an image that allows us to visualise the scene. If one is able to record the full light field at some plane, this recording could then "fool" an observer to see the scene despite only viewing a recorded copy of the phase and intensity profiles that the scene resulted in. This is exactly what is done in holography, where the intricate wavefronts coming off a complete scene can be encoded to an optical element via a space-varying two-dimensional phase profile, allowing the full light field of a scene to be reproduced [1, 140].

3.2 Phase profiles from metasurfaces

One particular feature of metasurfaces is that they can introduce discrete changes to optical properties at an interface. Hence, by cleverly engineering a metasurface to gradually change its phase response across a surface, it is possible to modify the laws of reflection and refraction at the interface [141]. Then something referred to as a *phase gradient metasurface* (PGM) is obtained. To get an intuitive understanding of this, let us inspect the case presented in Figure 3.2a. A plane wave is incident on a metasurface, whose constituent particles are designed so that they can add an arbitrary phase contribution between 0 and 2π. If the adjacent meta-atoms are designed to add a linearly changing amount of phase, the plane wave can be redirected to a different angle, while still remaining a plane wave. In a Huygens-Fresnel picture, the phase of each spherical wave point scatterer is tuned to add up to a plane wave of a certain angle.

Starting from Fermat's principle, Snell's law can be derived by considering the path that minimises the accumulated phase between two points P and Q in media of different index of refraction n_i and n_t (Figure 3.2b). A metasurface can then simply be modelled as an added discrete and spatially varying phase $\phi(x)$ at the interface between the two materials. Therefore with a PGM, the total acquired phase $\Phi(x)$ when travelling from P to Q becomes

$$\Phi_{\text{P-Q}}(x) = \frac{2\pi n_\mathrm{i}}{\lambda_0}\sqrt{x^2+a^2} + \phi(x) + \frac{2\pi n_\mathrm{t}}{\lambda_0}\sqrt{b^2+(l-x)^2}. \tag{3.1}$$

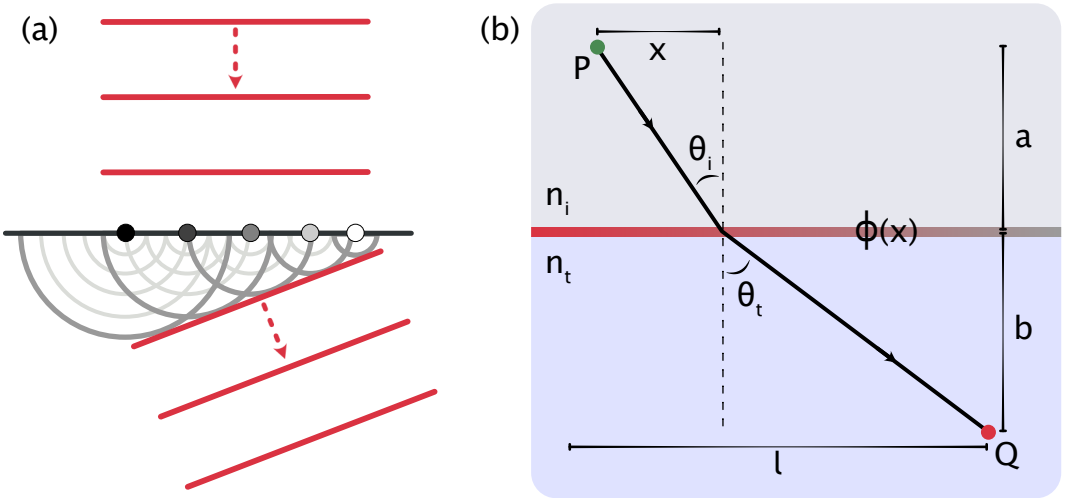

FIGURE 3.2: (a) Illustration of how a controlled phase gradient between adjacent objects can lead to beam steering. In this particular case, a linear phase gradient is imposed along the surface, leading to a simple beam deflection. The refractive equivalent to this system would be a simple wedge-prism used for beam steering. (b) A geometry in which generalised laws of refraction and reflections at an interface with a PGM can be derived by considering the path of least phase accumulation between points P and Q.

Taking the derivative of (3.1) with respect to x and setting it equal to zero to find the path that minimises the acquired phase results in

$$\frac{\mathrm{d}\Phi_{\text{P-Q}}(x)}{\mathrm{d}x} = \frac{2\pi n_\mathrm{i}}{\lambda_0}\frac{x}{\sqrt{x^2+a^2}} + \frac{\mathrm{d}\phi(x)}{\mathrm{d}x} + \frac{2\pi n_\mathrm{t}}{\lambda_0}\frac{-(l-x)}{\sqrt{b^2+(l-x)^2}} = 0. \tag{3.2}$$

By now identifying that $\frac{x}{\sqrt{x^2+a^2}} = \sin\theta_\mathrm{i}$ and $\frac{-(l-x)}{\sqrt{b^2+(l-x)^2}} = \sin\theta_\mathrm{t}$, Equation (3.2) can be simplified to

$$n_\mathrm{t}\sin\theta_\mathrm{t} - n_\mathrm{i}\sin\theta_\mathrm{i} = \frac{\lambda}{2\pi}\frac{\mathrm{d}\phi(x)}{\mathrm{d}x}, \tag{3.3}$$

where $\theta_{\mathrm{i,t}}$ are the angles of the incident and transmitted waves, while $\frac{\mathrm{d}\phi(x)}{\mathrm{d}x}$ is the in-plane variation in phase induced by the PGM. This can be recognised as a modified version of Snell's laws with a PGM at the interface [136, 141]. Similarly, for a PGM on a reflective surface, a generalised law of reflection at angle θ_r can be obtained as

$$\sin\theta_\mathrm{r} - \sin\theta_\mathrm{i} = \frac{\lambda}{2\pi n_\mathrm{i}}\frac{\mathrm{d}\phi(x)}{\mathrm{d}x}. \tag{3.4}$$

In two dimensions the derivative is generalised to a gradient in phase along the surface, giving rise to the PGM's name. Hence, by controlling the phase-gradient along the surface it is possible to change the propagation direction and polarisation of light and construct 2D equivalents to any refractive or reflective optical element. For example, by building the phase profile of a lens (Figure 3.1) light that passes through such a metasurface will be focused to a point. This is a powerful realisation that opens up countless opportunities for researchers to explore. In the context of this thesis, the PGM's light-manipulation can be seen to arise from momentum exchange between the nanostructured matter and light, with possible accompanying reaction forces and torques. Hence, any time a light beam's phase is altered by a PGM, it is synonymous to an engineered spatially varying momentum exchange between light and matter.

An impressive breadth of phase profiles is attainable by this technique; however, one critical limitation to keep in mind in the design process is that the steepest phase gradients attainable is set by the Nyquist criterion [142]. This implies that each 2π phase region must be mapped by at least two elements to avoid aliasing in the phase profile. That is, the difference in phase between adjacent elements $\Delta\phi \leq \pi$. Amongst other things, this sets a limitation for the largest achievable numerical aperture[1] for a flat lens where the phase is mapped by an element with unit-cell size Δx: The largest beam deflection angle θ_{max} occurs at the periphery of a lens, with an in-plane wave vector addition of $k_{\text{max}} = \frac{2\pi n_{\text{m}}}{\lambda} \sin\theta_{\text{max}}$. Hence by using the generalised Snell's law from Equation (3.3), the phase gradient required for a metasurface at this position must be [143]

$$\frac{\Delta\phi}{\Delta x} = \frac{2\pi n_{\text{m}}}{\lambda} \sin\theta_{\text{max}} \Rightarrow \Delta x = \frac{\lambda\Delta\phi}{2\pi n_{\text{m}} \sin\theta_{\text{max}}} \leq \frac{\lambda}{2n_{\text{m}} \sin\theta_{\text{max}}} \Rightarrow NA \leq \frac{\lambda}{2\Delta x}. \quad (3.5)$$

3.3 A brief history of phase-gradient metasurfaces

Considering the enhanced resonant light-matter interaction of plasmonic nanoparticles they seem to be prime candidates to use as building blocks in phase-gradient metasurfaces, where the local phase can be controlled by changing the shape and dimension of each individual nanostructure. Indeed, this was the reasoning in the pioneering PGM works in the early 2010s where plasmonic meta-atoms were used and the term was coined [135, 136, 141, 144–147]. While many proof-of-principle demonstrations of flat optical components were performed at the time with these plasmonic PGMs, finding a configuration for a single layer plasmonic metasurface with both full 2π phase coverage and high efficiency seemed to be elusive [148], especially in transmission mode where PGMs have remained below 10% efficient. Recently, an approach with metal-insulator-metal nanorods/nanoholes have broken this barrier and realised plasmonic metasurfaces with higher transmission efficiencies (>40%) [149, 150]; however at that stage, the community had already found its new forerunner for simultaneously obtaining full phase control and high efficiency, namely all-dielectric PGMs [151].

Partly coinciding with the surge in interest for PGMs was the realisation that nanoparticles made of high refractive index dielectric materials are useful as nano-optical resonators [84, 86]. Not only did these support multiple interesting resonances that could be combined to produce a stronger phase response, but they also displayed lower loss. This realisation was leveraged by researchers to construct single-layer metasurfaces with 2π phase coverage and efficiencies superior to anything seen at visible or NIR wavelengths before [152–155]. Today, state-of-the-art PGMs are almost exclusively fabricated by excavating some type of nanoscopic pattern in a dielectric material, chosen to have low loss in the desired wavelength region [156–158]. Dielectric metasurfaces also present the added benefit of using CMOS-compatible materials, eventually allowing them to be incorporated in contemporary fabrication processes and facilitating its potential commercialisation. For the interested reader, there are plenty of comprehensive

[1] Numerical aperture (NA) is a dimensionless quantity that describes how large the collection cone of a lens or objective is. NA = $n_{\text{m}} \sin\theta_{\text{max}}$ where n_{m} is the refractive index of the surrounding medium and θ_{max} is the largest angle that the objective can collect light from.

reviews for further explorations into both the past and present undertakings in the field of PGMs [17, 143, 159–161].

It is said that no discoveries occur in a vacuum, and this is certainly true for phase-gradient metasurfaces. Several decades before PGMs were introduced, similar wavefront shaping was performed in the microwave regime with frequency-selective surfaces [162–164]. Furthermore, with diffractive optics it has long been possible to make low-cost, efficient, and quite wideband optical elements [165–167], even competitive in commercial applications. However, as the fields of subwavelength gratings [168–172][2], advanced nanofabrication [175], and later dielectric nanophotonics [84] matured, these fields could combine with previous knowledge from both the microwave regime and diffractive optics to create synergies that lead to the unravelling of the exciting field of phase-gradient metasurfaces that we see today. As research progresses it does seem like PGMs do provide some unique properties not previously enabled by the other fields [176]; nevertheless, some controversy remains [177]. Regardless, what is oftentimes lost in the discussion is that, apart from nomenclature, PGMs constitute a subclass of diffractive optics where the unit-cell size is chosen to be smaller than the diffraction limit – effectively suppressing any diffraction order other than the zeroth one.

3.4 Metasurface building blocks

So far we have stated vaguely that phase-gradient metasurfaces can by modifying *some* of its properties impart a spatially varying phase profile to light. Plenty of approaches to do this are available and each comes with its unique set of benefits and drawbacks. All techniques can roughly be sorted into one of three categories, namely propagating, geometric, or resonant phase metasurfaces. Below follows introductory sections for each of these concepts [160, 161].

3.4.1 Propagating phase

From a pedagogic standpoint, propagating phase metasurfaces are probably the simplest to explain. From elementary optics, we know that the optical path length, and hence the accumulated phase, increases proportionally with the refractive index of the material. Hence, if the index of refraction could be controlled with high enough precision, any arbitrary phase gradient could be constructed. This would be the crowning achievement within graded-index optics research [178]. Locally altering the refractive index of a solid bulk material turns out to be exceedingly difficult; however, changing the *effective* refractive index of a subwavelength area by varying the filling ratio of the material is readily doable. Imagine a square lattice with a unit cell of area $\mathcal{P}^2$ containing a dielectric pillar of radius r_0, height H, and refractive index n_{diel} placed in air ($n_{\text{air}} \approx 1$). Such a lattice

[2] One should especially mention the work performed by Lalanne, Chavel, and coworkers in the late 90s on binary blazed subwavelength gratings. They produced TiO_2 nanopillars to make both beam deflectors and lenses of high efficiency for visible wavelengths [172–174]. Considering the striking similarity to today's metasurfaces, one could state that they were decades ahead of their time and did things that in 2015 merited publication in the most prestigious journals, only under a different name. That their work did not spur the PGM revolution seen in the early 2010s is a testament to the importance of timing and framing of the presented research.

would present a light-beam with the effective refractive index

$$n_{\text{eff}} = \frac{n_{\text{diel}}\pi r_0^2 + n_{\text{air}}(\mathcal{P}^2 - \pi r_0^2)}{\mathcal{P}^2}. \tag{3.6}$$

Neglecting any other resonant effects, by passing through the array of pillars a light beam would hence acquire a phase of

$$\phi = \frac{2\pi}{\lambda} n_{\text{eff}} H. \tag{3.7}$$

By then varying the pillar radius across the surface, the phase contribution for each pixel can be selected at will, effectively building up the PGM. As long as the height of the pillar is sufficient it is possible to cover the entire 2π phase range. In practice, the exact phase response is never so simple as Equation (3.7) since the nanopillars start acting as waveguides that will have resonances that alter the phase response and also induce loss channels exempt from the correct phase profile. Hence, for most applications, even this realisation of a phase-gradient metasurface require rigorous electrodynamical simulations to optimise the metasurface building block's geometry.

Much of this was realised by researchers active within diffractive optics long before the PGM revolution of today got started [170, 172–174]. Unfortunately, their contribution has not received much recognition, likely because they are referred to as binary blazed sub-wavelength gratings instead of phase-gradient metasurfaces. However, as the community started moving away from plasmonic building blocks, the propagation phase approach became popular and proved capable of producing efficient metasurfaces with a range of functionalities [160, 179–183]. Figure 3.3 displays a metasurface where circular nanodisks of varying sizes change the phase between 0 and 2π.

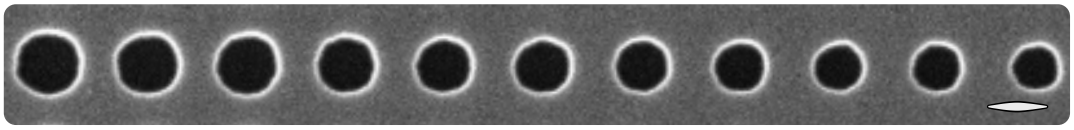

FIGURE 3.3: SEM image of an array of circular nanoholes designed as propagating phase elements, fabricated during exploratory work for the thesis. Each nanostructure defines a particular phase for its pixel dictated by its effective refractive index. The scale bar is 200 nm.

3.4.2 Geometric phase

In the middle of the 1950s, S. Pancharatnam performed substantial work on birefringent crystal optics together with his supervisor C. V. Raman. During this work, they discovered in particular that circularly polarised beams acquire a phase difference related to the orientation of the fast axis of the crystal [184]. What he had discovered with optical experiments was the first observation of the general concept of *geometric phase*, which was later generalised by Sir M. Berry to encompass phase advance of any system when it is subjected to so-called cyclic adiabatic permutations [185]. Since its discovery and generalisation, geometric or Pancharatnam-Berry (PB) phase has become a useful tool to understand processes in both classical and quantum physics.

For phase-gradient metasurfaces the geometric phase becomes a way to spatially control the phase response across a surface. The archetypical PB metasurface

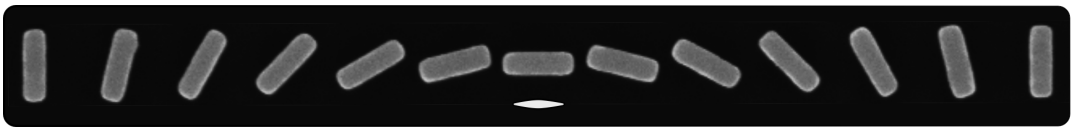

FIGURE 3.4: SEM image of a segment of an array of nanofins designed as PB phase elements. Fabricated during optimisation of the metasurfaces studied in **Paper III**. Each nanofin defines a particular phase for its unit cell in accordance with its rotation. The scale bar is 300 nm.

building block is an anisotropic nanofin (Figure 3.4). This can, due to shape-birefringence, function as a miniature half-wave plate, since an incoming wave experiences different effective indices of refraction along the two principal axis of the nanofin. It turns out that due to the geometrical phase contribution, *light interacting with the nanofin will acquire a phase ϕ that is twice the rotational angle θ of the nanofin* ($\phi = 2\theta$). The PB phase concept was used to build the metasurfaces investigated in **Paper III**.

The PB phase contribution that arises from the interaction with an arbitrary transmissive retarder can be understood from Jones matrix analysis. The matrix for a general retarder with phase delay φ and transmission coefficients $t_{x,y}$ for light polarised along or perpendicular to the retarder's fast axis is written as

$$\mathbf{J} = \begin{bmatrix} t_x & 0 \\ 0 & t_y \mathrm{e}^{i\varphi} \end{bmatrix}. \tag{3.8}$$

By combining this with a rotation matrix

$$\mathbf{M}(\theta) = \begin{bmatrix} \cos\theta & \sin\theta \\ -\sin\theta & \cos\theta \end{bmatrix}, \tag{3.9}$$

the transformation matrix for any arbitrary orientation of the waveplate becomes

$$\begin{aligned} \mathbf{T}(\theta) &= \mathbf{M}^{-1}\,\mathbf{J}\,\mathbf{M} = \\ &= \begin{bmatrix} t_x \cos^2\theta + t_y \mathrm{e}^{i\varphi} \sin^2\theta & (t_x - t_y \mathrm{e}^{i\varphi}) \cos\theta \sin\theta \\ (t_x - t_y \mathrm{e}^{i\varphi}) \cos\theta \sin\theta & t_x \sin^2\theta + t_y \mathrm{e}^{i\varphi} \cos^2\theta \end{bmatrix}. \end{aligned} \tag{3.10}$$

When an electric field of arbitrary polarisation $|E_{\text{in}}\rangle$ passes through the waveplate, the resulting outgoing electric field is obtained as the matrix multiplication $|E_{\text{out}}\rangle = \mathbf{T}(\theta)|E_{\text{in}}\rangle$. At first glance, there is no physically intuitive observations to make from this expression; however, after a lengthy exercise in algebraic manipulation it can be written as

$$\begin{aligned} |E_{\text{out}}\rangle &= \mathbf{T}(\theta)|E_{\text{in}}\rangle = \\ &= \varsigma_{\text{N}}|E_{\text{in}}\rangle + \varsigma_{\text{PB}}\left[\mathrm{e}^{2\theta i}|R\rangle\langle L|E_{\text{in}}\rangle + \mathrm{e}^{-2\theta i}|L\rangle\langle R|E_{\text{in}}\rangle\right]. \end{aligned} \tag{3.11}$$

Here, $\langle\star|\star\rangle$ denotes the scalar product, $\varsigma_{\text{N}} = \frac{1}{2}(t_x + t_y \mathrm{e}^{i\varphi})$ and $\varsigma_{\text{PB}} = \frac{1}{2}(t_x - t_y \mathrm{e}^{i\varphi})$, whereas $|L\rangle = \frac{1}{\sqrt{2}}\begin{bmatrix} 1 \\ i \end{bmatrix}$ and $|R\rangle = \frac{1}{\sqrt{2}}\begin{bmatrix} 1 \\ -i \end{bmatrix}$ are the circularly polarised unit vectors. On this form, there are plenty of valuable conclusions about the effect of passing light through a half-wave plate. The first term in Equation (3.11) describes a component of light that will pass through the waveplate unaffected by it. The two other terms relate to light that will experience the PB phase shift of $\phi = |2\theta|$, with the sign of the shift being dictated by the handedness of the light. The total amount

of light acquiring the PB phase shift is determined by the magnitude of $t_{x,y}$ and φ, whereas the ratio of light acquiring either positive or negative phase is determined by the ellipticity of $|E_{\text{in}}\rangle$. In the special case of a perfect waveplate with $t_x = t_y = 1$ and $\varphi = \pi$, a circularly polarised beam (e.g. $|L\rangle$) is subjected to total polarisation conversion and all light picks up the PB phase of $\phi = 2\pi$. Then $|E_{\text{out}}\rangle = \mathrm{e}^{2\theta i}|R\rangle$.

In the original work by Pancharatnam, the phase gain was proven geometrically by comparing traces for two different orientations of the waveplate on the Poincaré sphere [184]. However, a more intuitive way of understanding how differently oriented nanofins cause transmitted or reflected light to acquire an angle-dependent phase is suggested in [152]. They propose to recall: (1) the basic function of the nanofin as a half-wave plate, and (2) the decomposition of a circularly polarised wave as two temporally offset linear components. The effect of a half-wave plate on a linearly polarised wave is to rotate the plane of polarisation by twice the angle between the plane of polarisation and the waveplate's fast axis. This effectively "mirrors" the polarisation plane in the fast axis of the waveplate. By propagating through the waveplate and hence reflecting the linearly polarised components in the axis of the waveplate, the resulting outgoing circularly polarised wave is seen to switch its handedness and acquire a phase shift that is twice the rotation angle of the waveplate (Figure 3.5).

That such an effect is present for a macroscopic waveplate is one thing; however, that it occurs even if the waveplate is a single nanoparticle is quite remarkable. If the contrast between the nanofin's and the surrounding media's index of refraction is sufficiently high, the nanostructure will act as a truncated waveguide and confine the light [171]. Hence, neighbouring nanofins can have different orientations and subsequently impart different phase to the light that passes through that particular object. Therefore, by discretising any desired phase profile, a Pancharatnam-Berry metasurface can be designed to reproduce that profile by simply selecting the orientation θ of each sub-wavelength element to be half the desired phase ϕ at that location ($\phi = 2\theta$).

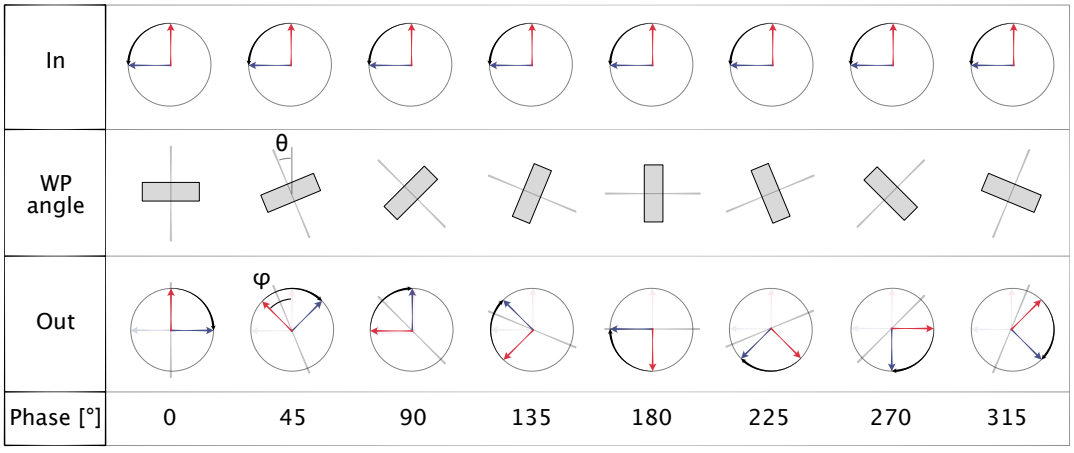

FIGURE 3.5: Illustration of the origin of the PB phase for a half-wave plate. The top row indicated left-handed polarised light propagating into the page. This circularly polarised light can be decomposed into linear time-delayed components (red and blue arrows with $\frac{\pi}{2}$ phase difference). By then "mirroring" these linear components in the differently oriented fast axis waveplates (thin grey lines, middle row), an outgoing right-handed circularly polarised wave (bottom row) with an orientation-dependent phase gain of $\phi = 2\theta$ arises. This is the PB phase used to build up a metasurface based on this technique.

The pioneering realisation that the Pancharatnam-Berry phase concept was useful to sculpt phase profiles of optical elements were made in the early 2000s by the group of E. Hasman. They used spatially varying subwavelength gratings in the mid-IR spectral range to perform a range of ingenious experiments [186–190]. As with phase-gradient metasurfaces in general, also PB metasurfaces made of plasmonic meta-atoms were initially considered [191–193]. Also here, the community thereupon turned to dielectric materials after some convincing demonstrations by the Brongersma [152] and Capasso [155] groups. Since then dielectric PB phase-gradient metasurfaces have been thoroughly researched and seem to be a promising approach to make both highly efficient and diverse metasurfaces [156, 194, 195]. For more detail, an instructive recent review especially focused on progress in metasurfaces based on PB phase can be found in [161].

Regardless of what flat optical component is made it is important to verify that the expected phase profile is obtained experimentally from fabrication. Often this is simply done by noting that the metasurface performs the task it is intended for, hence assuming that the designed phase profile is reproduced. However, to truly improve the performance of a metasurface it would be useful to image its actual imparted phase profile. Again the technique of quadriwave lateral shearing interferometry (QLSI) can be employed to elucidate this. In **Paper S.XIV**, QLSI was used to experimentally record the phase profile of metasurfaces operating as lenses and beam deflectors (Figure 3.6).

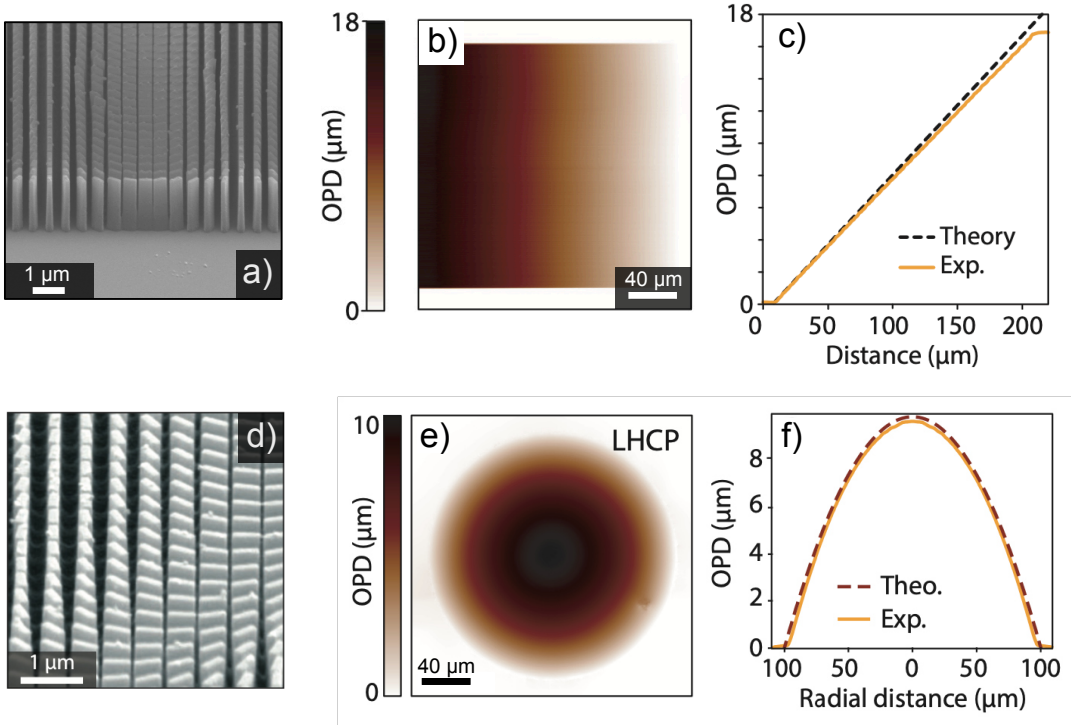

FIGURE 3.6: Phase-gradient metasurfaces based on PB phase elements where the actual imparted phase profile (optical path difference, OPD) is measured by QLSI. The top row displays data for a beam-steering metasurface, whereas the bottom row describes a positive lens, as it acts on left-handed circularly polarised light. (a,d) SEM images of metasurfaces. (b,e) Measured 2D phase profiles. (c,f) Averaged (horizontal/radial) data from the 2D images compared with the expected phase profile from design and theory. The figure is adapted with permission from [196] ©2021 American Chemical Society.

Furthermore, most PGMs are designed to manipulate and shape incident plane waves. However, regularly the phase front of light incident on an optical component has a curvature, the most common being associated with a Gaussian beam. Therefore, in **Paper S.IX**, a PGM reflector was designed to act as a concave mirror that reflects an incoming focused Gaussian beam onto itself. Figure 3.7 demonstrates that a metasurface can theoretically do this with over 90% reflectance and without disrupting the beam shape.

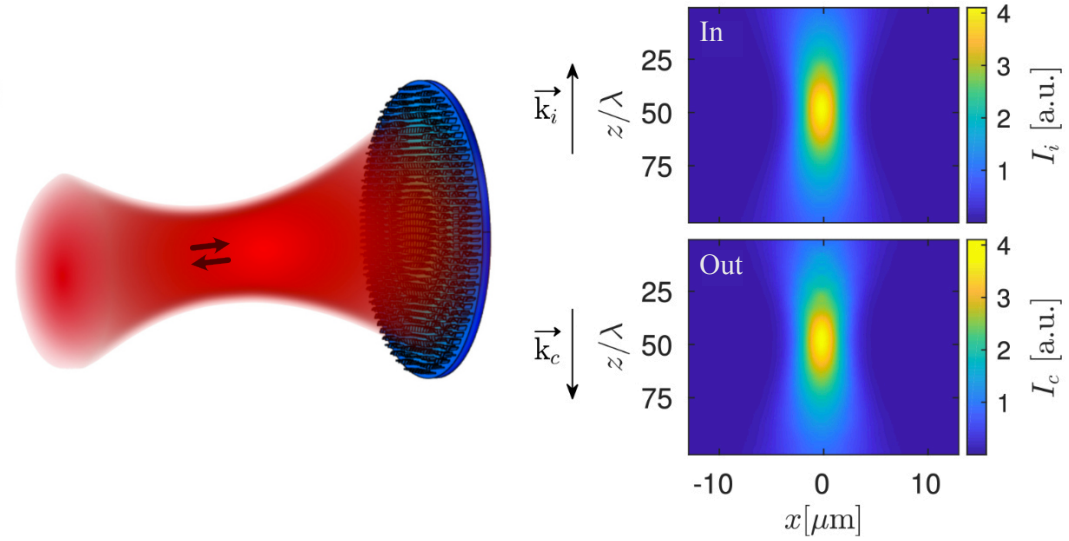

FIGURE 3.7: A theoretical realisation of a PGM in the form of a concave mirror, designed to reflect an incoming Gaussian beam upon itself. For a mirror designed with a numerical aperture of 0.24, the beam is seen to retrace both its path and curvature after it has been reflected from the metamirror while retaining above 90% of its intensity. The figure is adapted with permission from [197] ©2019 The Optical Society.

A tangential field worth mentioning due to its overlap with PB phase-based PGMs is that of liquid crystal optics using geometric phase [198–201]. The birefringence caused by the anisotropic nature of liquid crystal molecules lends itself well to producing similar phase profiles as discussed above. An inherent benefit is that the liquid crystal pixels can be controlled with an electric field and therefore allow for switchable optical devices. However, as patterning of liquid crystal molecules are more challenging, the range of different optical elements are limited compared to metasurfaces.

Lastly, a property usually presented as a drawback for PB phase metasurfaces is that when operating with unpolarised light the inherent maximum efficiency of a lens is 50%, which for many applications is a significant drawback. On the other hand, this does offer an extra degree of freedom in that the function of a lens can be tuned to be either converging or diverging since the imparted phase gradient will be positive or negative depending on the handedness of incoming light [191]. At the same time, using multiple ($\geq$4) LC-based PB lenses in sequence has been demonstrated to produce a polarisation insensitive compound lens [202], which might be of interest also for metasurface-based PB systems.

3.4.3 Resonant phase

In the general field of dielectric nanophotonics, many interesting fundamental resonance modes have been investigated [12], and some of them were introduced in Chapter 2. In recent years, employing and tuning specific such resonances has been suggested as a way to improve PGMs. One example is when an electric dipole and a magnetic dipole of equal magnitude and phase overlap, fulfilling Kerker's condition [92]. Due to destructive interference, the back-scattering of such a structure is completely cancelled. A nanoparticle fulfilling this condition will act as a Huygens' source, which only reradiates in the forward direction, and therefore constitute a building block in a Huygens' metasurface. These hold promise to further increase the efficiency of flat optical components [154, 203–206]; however, still suffer from narrow spectral bandwidth, and large electromagnetic coupling between adjacent meta-atoms [160].

Furthermore, another area where resonant PGMs appear is for realising efficient high-angle beam steering and by extension efficient high-NA lenses – an area where metalenses hold an advantage over diffractive optical components [176]. The highest efficiency near-unity numerical aperture lens (NA ≈ 1 in air) realised to date is based on resonant dielectric meta-atoms [207]. By overlapping resonances of two adjacent nanoparticles, a compound antenna (Figure 3.8) can be created that asymmetrically scatters light [208, 209]. By placing such antennas in an array, the direction of asymmetric scattering can be tuned by varying the antenna spacing. Such resonant dielectric dimer metasurfaces for high-angle beam steering were used for the experiments performed in **Paper IV**.

By strict definition, these metasurfaces can be considered blazed diffraction gratings rather than PGMs, since the unit-cell size is larger than the wavelength. However, despite being constructed by sub-wavelength unit-cells, a PGM always has a diffractive supercell period $\mathcal{P}_{\text{sup}}$ within which a number of meta-atoms build up a 2π zone. This period sets the beam-steering angle according to $\vartheta = \sin^{-1} \frac{\lambda}{\mathcal{P}_{\text{sup}}}$ [152, 194]. For a beam deflector, $\mathcal{P}_{\text{sup}}$ is constant across the surface, whereas for a lens it will decrease away from the optical axis. Considering this, such resonant compound antennas should be counted as building blocks in PGMs too, only where the phase response for individual subwavelength particles is difficult to separate due to the high degree of electromagnetic coupling.

FIGURE 3.8: SEM image of a segment of an array of nanodimers as elements in a resonant metasurface, fabricated during method development for **Paper IV** . The scale bar is 300 nm.

3.5 Research frontier

The forefront of research within phase-gradient metasurfaces is developing at an incredible pace. As mentioned above, the field holds enormous potential to contribute to a range of avenues of both science and technology. Therefore, a chapter on phase-gradient metasurfaces would be incomplete without an outlook towards the challenges remaining for them to reach their full potential. Four major research directions in the field are identified, namely:

1. Scalability:

   Up to this point, most fabrication in the metasurface community is done through electron beam lithography, to define the detailed and spatially varying meta-atom configurations. This is fine for scientific exploration, but by production line standards it is simply not scalable since it is several orders of magnitude too slow. Therefore, one struggle that PGM proponents need to address is that of scalability in fabrication. The most advantageous move in this direction seems to be to approach the semiconductor fabrication industry by using deep UV lithography to both scale and speed up potential fabrication [210–213]. Another approach would be to use nano-imprint lithography to define the nanoparticle structures. Then a mould is made with electron beam lithography and subsequently replicated multiple times to make flat optical elements [214, 215].

2. Achromatic metasurfaces:

   A phase profile that is engineered to produce a certain optical effect is wavelength-specific. This means that there is a strong wavelength dependence to basic PGMs, even in the absence of material dispersion. Hence, early industrial adoption of the technique could be in laser-based applications. Nevertheless, metasurfaces that operate with achromatic behaviour over a broad wavelength spectrum is highly desirable for most other optical components. Therefore, designing achromatic PGMs has been a top priority for many researchers in the community for several years. Approaches include fine-tuning the spectral response of meta-atoms [158, 216–218], making compensative doublet metalenses [219, 220], metasurface-refractive multiplet lens systems leveraging the opposite dispersion of refractive and diffractive optics [221, 222], and others as outlined in reviews [160, 161, 223].

3. Active metasurfaces:

   The PGMs discussed above are all stationary and each is designed for a certain fixed function. There are plenty of systems where replacing bulk refractive optical components with flat counterparts could reduce weight and form factor. However, if a metasurface could be actively tuned to any desired phase profile, that would add a whole new dimension of possible uses. Therefore, one attractive field of research today is to try to implement active control of phase profiles with metasurfaces. A range of attempts to reach this has been put forth. Amongst the most innovative are; multiplexed metasurfaces [224], flexible metasurfaces [225, 226], and metasurfaces combined with liquid crystals to augment already established SLM[3] techniques [227, 228]. Yet others propose to use material properties with a dispersive response to alter the metasurface's optical behaviour [229–231].

   An alternative approach for obtaining tuneable flat optical components has been investigated during the last years. By producing a thermal gradient in some material, a phase gradient effect can be produced via the concomitant refractive index gradient [232–234]. Albeit a step removed from the patterned metasurfaces

[3] The spatial light modulator (SLM) can in many ways be considered the micro-scale counterpart to metasurfaces in that they can manipulate the phase of an incoming wave in space to produce any desired profile. Such systems are routinely used in both research and commercial products to manipulate light.

discussed here, it is noteworthy due to the clear connection it has to the photothermal effects discussed in Section 2.5.

4. Applications:

   As the field is coming of age and the fundamental physical queries are resolved, more focus is put on demonstrating the usefulness for real-world applications. There seems to be a consensus about the disruptive potential of flat optics and in 2019 it was among the "Top 10 Emerging Technologies" according to Scientific American [235]. In recent years a wealth of interesting demonstrations where PGMs are used as an integral part in a more complete system has emerged. A few of the most exciting ones include: Vertical cavity emitting lasers (VCSEL) with integrated metasurfaces for beam-shaping [236]; multi-photon entangled light sources [237]; achromatic light-field imaging with metalens arrays [183]; compact imaging systems in biomedical applications [238–240], augmented and virtual reality (AR/VR) devices [241, 242]; LIDAR systems [243]; and display technology [244]. Lastly, it seems that both established technology companies as well as start-up companies are vesting interests to a larger extent in the possibilities offered by metasurfaces [245].

Chapter 4

Optical forces and torques

In Chapter 2 it was pointed out that the momentum of light is insufficient to noticeably alter the momentum of electrons in matter. Similarly, for long it was thought that any useful mechanical effects on materials were negligible too. However, as photons interact with matter they do partake in momentum transfer, albeit the per-photon contribution is minute. Regardless, if the photon density is sufficient, the momentum transfer from light to matter will inevitably cause some noticeable mechanical effects, through optical forces and torques. The following chapter aims to introduce the components of optical manipulation essential for the thesis. For a more comprehensive summary, see the excellent book by Jones *et al.* [22] or reviews on the topic [21, 246, 247].

4.1 Optical forces

The most basic optical force, radiation pressure, arises even with plane wave illumination and at steady state propels any particle along the propagation direction of light [18]. The radiation pressure can be expressed in terms of the time-averaged Poynting vector $\mathbf{S}$ and the speed of light c as $P = \langle \mathbf{S} \rangle / c$, or as the summed force imparted by all photons with individual momentum $p = h/\lambda$. If a ray of light is completely absorbed all the photon momentum is transferred to the physical object, and if light is perfectly reflected twice this momentum is transferred.

Moreover, if a particle or ensemble of particles, scatters light non-symmetrically or simply redirects light, the physical object must experience an instantaneous force in the opposite direction for momentum to be conserved. On a macroscopic scale, the avenue where optical momentum transfer can become most relevant may be in the drag-free environment of space, where a long-term goal has been to utilise optical forces to construct solar-sail vehicles driven by light's momentum [248, 249]. Recently, phase-gradient metasurfaces have even been suggested as a means to stabilise these so-called beam rider structures [250, 251].

Nevertheless, even in viscous media, small enough particles or large enough light intensities can result in forces sufficient to propel objects with appreciable speeds. For example, directionally scattering resonant nanostructures have been seen to experience reactive optical forces that propel them laterally [252, 253]. In fact, any manifestation of a phase gradient of light, induced or incident, will result in an optical force that propels an object [254]. This is leveraged when collimated light is redirected to produce optical forces that lift refractive microparticles [255–257] or propel wedge-shaped microparticles [258] in liquid environments. Indeed, even

centimetre-scaled liquid crystal PB phase objects have been seen to move due to directional light steering [259]. In **Paper IV** this idea was used to propel microscopic particles in plane wave illumination. For steady state propagation in all these cases, an additional force must be present that maintains the structure's orientation. Often this is an interface that prevent the torque that would otherwise reorient the particle and quench the reactive force.

4.1.1 Optical forces in a focused beam

Once light is focused through a strong lens the incident total momentum is vastly more complex and therefore so are the resulting optical forces and torques. As a result, as was discovered in the 1980s by Arthur Ashkin and coworkers, small particles can be confined in 3D by light in optical tweezers with sufficient laser power.

In a focused light beam, the induced forces can be decomposed into a scattering and absorption force component ($F_{\text{scat/abs}}$) and a gradient force (F_{grad}) component. The first is a non-conservative force acting in the propagation direction of the light, which arises from scattering and absorption processes. The gradient force appears as a reactive force in response to how the optical interaction with the particle alters the momentum distribution of the outgoing light in relation to the incoming one. The gradient force is therefore responsible for the confinement in optical tweezers. Three-dimensional confinement can be obtained when the gradient force overcomes the scattering/absorption force. To achieve sufficiently strong gradient forces experimentally, microscope objectives with high numerical apertures are employed due to their large deflection angles.

Large dielectric particles in the Mie regime will redirect photon momentum due to refraction, resulting in a counter-force on the particle. Hence, an attractive potential is created near the intensity maximum of a trapping laser. This is referred to as the ray optics model of optical tweezers. For particles smaller than the wavelength, in the so-called Rayleigh regime, the description based on refraction breaks down. Instead, the particle can be seen to experience a Lorentz force in response to its induced polarisation. Expressions for the optical forces can then be derived under the quasi-static approximation [260]. When the electric dipole moment $\mathbf{p}$ and the incoming electric field $\mathbf{E}$ are linearly related the total force can be decomposed into the gradient and scattering and absorption force components;

$$\mathbf{F}_{\text{grad}} = \frac{\varepsilon_0 \varepsilon_{\text{m}}}{4} \nabla \left(\mathbf{E}^* \cdot \boldsymbol{\alpha}' \cdot \mathbf{E} \right) \tag{4.1}$$

$$\mathbf{F}_{\text{scat/abs}} = \frac{\varepsilon_0 \varepsilon_{\text{m}}}{2} \text{Im}\{ \mathbf{E}^* \cdot \boldsymbol{\alpha}'' \cdot \nabla \mathbf{E} \}, \tag{4.2}$$

where * denotes the complex conjugate. For particles with a scalar polarisability (i.e. spheres, or nanorods aligned with the Cartesian axes of the incoming light) and by introducing $I = |\mathbf{E}|^2$, the expressions can be simplified further to

$$\mathbf{F}_{\text{grad}} = \frac{\varepsilon_0 \varepsilon_{\text{m}}}{4} \alpha' \nabla I, \qquad \mathbf{F}_{\text{scat/abs}} = \frac{\varepsilon_0 \varepsilon_{\text{m}}}{2} \alpha'' \text{Im}\{ \mathbf{E}^* \cdot \nabla \mathbf{E}) \}.$$

For a particle with arbitrary size and shape the resulting optical forces can be found using more advanced numerical methods. Conservation of electromagnetic energy flowing through a surface enclosing a particle yielded its optical properties

(Equation (2.11)). Similarly, by considering the conservation of momentum across the bounding interface, the optical forces for an arbitrary particle can be calculated. This is done by following the Maxwell's stress tensor method [22].

As seen from Equation (4.1), a particle with positive polarisability (refractive index higher than its surrounding) will be directed towards the high-intensity region of the light, whereas one of negative polarisability will be expelled from the trap. For plasmonic particles, the sign of the real part of the polarisability may change when crossing the LSP resonance due to a phase change of the resonance. This may lead to the gradient force being attractive for light on the low-frequency (red) side of the LSP peak, while repulsive for high-frequency (blue) light [29]. Furthermore, when it comes to metallic nanoparticles, they are generally difficult to confine in three dimensions with single-beam optical tweezers. Due to their strongly enhanced scattering and absorption close to the LSP resonance, the scattering and absorption force becomes larger than the gradient force. However, if one detunes the trapping laser from the LSP resonance wavelength for small metallic nanoparticles, 3D confinement is possible [28].

The electromagnetic field in optical tweezers is commonly a Gaussian beam. Within the paraxial approximation[1], the optical forces on particles in the Rayleigh regime can be calculated (derivations outlined in references [262, 263]). Figure 4.1 displays results of such calculations performed for a nanorod of length 80 nm and width 40 nm (see extinction spectra in Figure 2.8), as it is placed in the focus of a Gaussian beam with divergence equal to that of an objective with numerical aperture NA = 1.4. To illustrate the importance of the LSP resonance on the trapping stability, the forces are investigated at two standard laser wavelengths: 660 nm (red light, Figure 4.1a) and 1064 nm (NIR light, Figure 4.1b). For the 660 nm laser, the scattering and absorption component dominates, and the particle is propelled in the propagation direction of the light. The NIR laser, however, excites the particle far away from resonance and produces an optical force that is dominated by the gradient force, and hence confines the particle in 3D.

Stable trapping occurs when the potential well $\mathcal{U}(\mathbf{r})$ caused by the optical forces is much deeper than the particle's kinetic energy due to Brownian motion. Therefore, the stability criterion is defined as when the ratio $\exp\left[-\frac{\mathcal{U}(\mathbf{r})}{k_\mathrm{B}T}\right] \ll 1$, where k_B is the Boltzmann constant. An estimate to when this criterion is fulfilled is when $\frac{\mathcal{U}(\mathbf{r})}{k_\mathrm{B}T} \geq 10$ [20], corresponding to the particle statistically residing in the trap for hundreds of seconds [264]. For 1064 nm laser light (Figure 4.1b), this criterion is fulfilled if the temperature is assumed to be below $T = 430$ K, and stable trapping is thus possible. On the contrary, for 660 nm illumination, three-dimensional confinement is not possible since the scattering force surpasses the gradient force, and the particle will unavoidably be propelled along the optical axis. In the rightmost graph of Figure 4.1a this can be understood seeing that all force vectors are directed upwards. Nevertheless, both the optical forces are significantly enhanced by the LSP resonance and the potential well in the xy plane is deep ($> 60k_\mathrm{B}T$). Hence, if the particle's movement in the z-direction is restricted by other means, the particle will be stably trapped in the radial plane.

[1]The validity of the paraxial model is decreasing as the angle of incoming radiation increases. Hence, for high NA objectives, the estimated forces will differ from their true values [261]. Nevertheless, since the purpose here is to illustrate the qualitative properties of the Gaussian optical trap, such deviations are neglected.

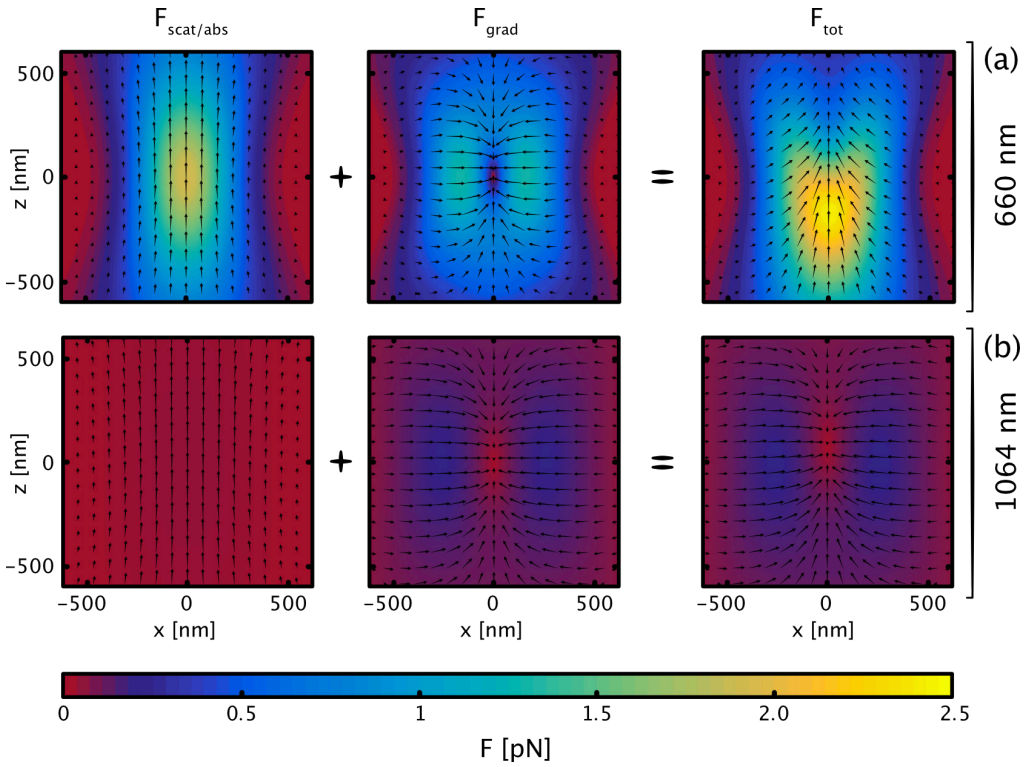

FIGURE 4.1: Direction and magnitude of optical forces for a point dipole with the optical properties of a prolate spheroid gold nanoparticle (80 nm long and 40 nm wide) in a paraxial Gaussian beam with circularly polarised laser light at the wavelength of (a) 660 nm, and (b) 1064 nm. The light is focused through an objective of NA = 1.4 and has a total power of 100 mW. The leftmost graphs show the scattering component, the middle ones the gradient force component, and the rightmost the total force. The maximum force values are $F_{\text{max}} = 2.5$ pN and 150 fN for (a) and (b), respectively.

The effects associated with near-resonance excitation can be beneficial for applications. In those cases, one can sacrifice one dimension of manipulation for stable confinement in two dimensions by using alternative configurations for optical tweezers. Such could include counterpropagating optical traps discussed in references [19, 265] and **Paper S.VII**, where two beams with opposite propagation directions are superimposed and effectively cancel the scattering force. Another technique utilises a glass surface with the same charge polarity as the trapped object. As the particle is pushed by radiation pressure towards the charged surface it will be repelled by Coulomb interaction and find a stable trapping position at some distance from the glass-water interface. This technique is subsequently referred to as "2D optical tweezers" and was used in **Paper I** and **II**. Its underlying physics is discussed further in Section 4.4.

4.1.2 Optical trapping with phase-gradient metasurfaces

Working with optical tweezers puts high demands on the objective lens used. To obtain strong gradient forces, a lens with high quality and NA is needed. The working distance, cost, immersion medium, flexibility and user-friendliness, parallelisation, and miniaturisation can also play a role for the end result. In this thesis where a novel form of flat lenses is studied in conjunction with optical forces, it is natural to imagine combining these two to study optical trapping with flat lenses.

Indeed, this is such a promising and intuitive idea that researchers have already touched upon this for quite some time. Already before the phase-gradient metasurface surge in the early 2010s there were studies using Fresnel zone plates [266] and diffractive optics [267] to construct low form factor optical tweezers systems. Yet, as phase-gradient metasurfaces have become more popular, it seems they could offer some novel opportunities to the optomanipulation community:

A theoretical study suggested the benefit of phase-gradient metasurfaces for optical manipulation due to their potential to create complex fields carrying both linear and angular momentum [56]. Then in 2018, the first experimental realisations were presented. First, 3D optical trapping using phase-gradient metasurfaces was realised with a reflective Fresnel zone plate high-contrast grating to form a focus to trap particles in microfluidic environments [54]. A further benefit of phase-gradient metasurfaces is that they offer control over the polarisation of light as well as its propagation. This was around the same time used to demonstrate metalens optical tweezers which could control the trapping location of microparticles along the optical axis, by using polarisation sensitive meta-atoms which for orthogonal linear polarisation formed foci at two different locations [55].

Since these first demonstrations, a range of studies has been published that explore the topic of phase-gradient metasurface optical tweezers. From theoretical studies exploring new potential trapping geometries, such as gradient line-traps [268, 269] or coherent beam focus steering [270] for particle sorting, to experimental realisations of high-efficiency transmissive dielectric metasurfaces with ability to produce both optical forces and torques [57], and dual-focus diffraction-limited optical traps [271]. It seems that the idea might be picking up momentum and it will be interesting to see how the field progresses in the years to come.

4.2 Optical torque

Similar to linear momentum, if a particle causes the angular momentum of light to change after an interaction, the object must experience a counteracting torque. The fundamental observations of light-induced torques in the early 20^{th} century [42] did not amount to much experimental follow-up work at the time. However, the interest was rekindled as optical tweezers grew more common, and it turned out that also light-induced torques could be applied to the optomechanically confined objects, providing an additional level of control [272].

Angular momentum can be carried by light in two different forms, either by its polarisation or by the shape of its wavefront. These two types are referred to as spin angular momentum (SAM) [42], and orbital angular momentum (OAM) [273], and their function and difference are illustrated in Figure 4.2. Hence, to impart a net torque to an object the optical interaction needs to result in a change in the angular momentum density of light. This can be done when a particle simply absorbs light that carries either spin- [274–276] or orbital angular momentum [272, 277]. Moreover, angular momentum transfer can arise from an altered polarisation state of the reemitted light. For example, birefringent particles can act as waveplates and convert e.g. linearly polarised light to circularly polarised light [43, 45, 278], or asymmetric particles can scatter light in such a way as to introduce OAM to the exiting light [279–282].

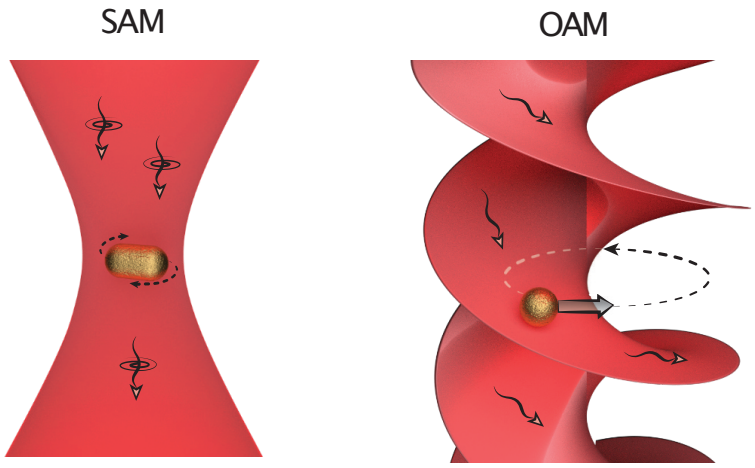

FIGURE 4.2: Illustration of the function and difference between a light beam carrying spin angular momentum (SAM, left) through its polarisation state, and orbital angular momentum (OAM, right) through its phase front. Figure is adapted from **Paper S.XI** with permission from [283] ©2019 American Chemical Society.

The majority of studies on optically induced torques have been concerned with microscopic objects. However, the enhanced light-matter interactions offered by resonant nanoparticles could be useful for enhanced optical torques as well as forces [46, 47, 246, 284]. Through resonantly enhanced optical torques, gold nanoparticles have, while optically trapped in 2D against a cover-glass, been made to spin in water with rotation frequencies above several kHz for nanospheres [276] and several tens of kHz for nanorods (**Paper S.I**). In **Paper I**, the rotational dynamics of such a spinning nanoparticle was used to study photothermal effects.

For stable rotation around one axis, the equation of motion can be written as

$$J\ddot{\theta}(t) = \mathcal{M}_{\text{opt}} + \mathcal{M}_{\text{f}} + \mathcal{M}_{\text{s}}, \tag{4.3}$$

where J is the moment of inertia for the particle, θ is the orientation angle, $\mathcal{M}_{\text{opt}}$ is the driving optical torque, $\mathcal{M}_{\text{f}}$ the opposing frictional torque from the surrounding liquid, and $\mathcal{M}_{\text{s}}$ a stochastic torque due to rotational Brownian motion, whose time-average is zero.

The frictional torque from the surrounding liquid is counteracting the optical torque. For a small spherical or spheroidal particle, the flow of liquid around the object is laminar due to the low Reynolds number. Consequently, the friction torque can be expressed as $\mathcal{M}_{\text{f}} = -\gamma_{\text{r}}\Omega = -\pi\mathcal{G}\eta(T)L^3\Omega$ [53], where Ω is the angular velocity and γ_{r} is the rotational friction coefficient for a sphere or prolate spheroidal particle expressed in terms of the length of the particle L, the viscosity of the surrounding water $\eta(T)$. $\mathcal{G}$ is a geometrical shape correction factor, that for spheres is equal to one and approaches zero when a spheroidal particle's eccentricity approaches one [285].

A general expression for the total optical torque ($\mathcal{M}_{\text{opt}}$) is attainable analytically for spheres and spheroids, either small enough for the quasi-static model to be valid, or using Mie theory. When these can be used to estimate an electrical dipole strength $\mathbf{p}$ that dominates the multipolar response, the time-averaged optical torque perpendicular to the direction of propagation of light can be related to the incoming electric field $\mathbf{E}$ as

$$\mathcal{M}_{\text{opt}} = \langle \mathbf{p} \times \mathbf{E} \rangle. \tag{4.4}$$

In the case of circularly polarised light, an isotropic particle will experience a torque that is solely accounted for by absorption of SAM, whereas a perfect thin rod (1D polarisable particle) will derive its torque from a polarised scattering component as well as from absorption. In a more complex case, with a particle that is both asymmetric and absorptive, the total torque $\mathcal{M}_{\text{opt}}$ can be obtained by integrating Maxwell's stress tensor from a numerically obtained electric field distribution [284]. Regardless of how the optical torque is estimated, when it is exactly counteracted by the friction torque ($\mathcal{M}_{\text{opt}} = \mathcal{M}_{\text{f}}$), the particle is on average rotating with a frequency as determined by [53]

$$f_{\text{avg}} = \frac{\mathcal{M}_{\text{opt}}}{2\pi\gamma_{\text{r}}}, \tag{4.5}$$

The control offered by optical forces and torques enables applications within e.g. microrheology [286], biology of both living organisms [287] and its DNA building blocks (**Paper S.IV**), non-equilibrium thermodynamics (**Paper S.V**), and as optical torque wrenches [288], to mention a few. In general, optical forces and torques is one of several options to drive so-called nano- and micromotors with light. This and other techniques have recently been reviewed in **Paper S.XI** for nanoparticles and in several reviews for microscopic particles [289, 290].

Lastly, the studies mentioned above are all performed in water. However, optical manipulation can also be performed in air [291] and even vacuum. Thanks to the non-existent drag in vacuum, rotation frequencies of several MHz have been observed [292], and such rotating particles have been used to build record-sensitivity torque sensors [293].

4.3 Brownian motion

Even if optical forces and torques can allow micro- and nanoparticles to be confined to impressively small volumes, their motion cannot be stopped completely. The erratic and seemingly random motion of small particles has been observed and pondered over for centuries. An early documented discussion about such motion and its underlying cause is found in the Roman philosopher Lucretius's "On the Nature of Things" from the last century BC [294] where he eloquently describes it as:

> "Observe what happens when sunbeams are admitted into a building and shed light on its shadowy places. You will see a multitude of tiny particles mingling in a multitude of ways... their dancing is an actual indication of underlying movements of matter that are hidden from our sight... It originates with the atoms which move of themselves. Then those small compound bodies that are least removed from the impetus of the atoms are set in motion by the impact of their invisible blows and in turn cannon against slightly larger bodies. So the movement mounts up from the atoms and gradually emerges to the level of our senses, so that those bodies are in motion that we see in sunbeams, moved by blows that remain invisible."

Indeed, such random motion referred to as Brownian motion is caused by collisions between the particle and its surrounding molecules, as proven by Einstein in 1905 [295]. It turns out that the motion of the Brownian particle is well described by complementing Newton's equation of motion with a stochastic term [22]. One obtains the Langevin equation of motion for *translational* Brownian

motion as

$$m\ddot{\mathbf{r}}(t) = -\gamma_{\mathrm{t}}\dot{\mathbf{r}}(t) + \mathcal{F}(t), \tag{4.6}$$

where $\mathcal{F}(t)$ is a random force with zero time average and that is uncorrelated in time (i.e. $\langle\mathcal{F}(t)\rangle = 0$ and $\langle\mathcal{F}(t)\mathcal{F}(t')\rangle = 0$). m is the particle's mass and γ_{t} its hydrodynamic friction coefficient for translational motion, which for a sphere in the low Reynolds number regime[2] can be written using Stokes's law as $\gamma_{\mathrm{t}} = 6\pi\eta r_0$. Here, η is the environment's viscosity, which for water can be approximated by an Arrhenius-type equation [276, 297].

In the presence of an external force $F(\mathbf{r})$ (e.g. the optical forces from the laser tweezers) and in the low Reynolds number regime, the Langevin equation can be rewritten as [22]

$$\dot{\mathbf{r}}(t) = -\frac{1}{\gamma_{\mathrm{t}}}F(\mathbf{r}) + \sqrt{2D_{\mathrm{t}}}W(t). \tag{4.7}$$

$D_{\mathrm{t}} = \frac{k_{\mathrm{B}}T}{\gamma_{\mathrm{t}}}$ is the diffusion coefficient, and $W(t)$ is white noise. The acceleration in Equation (4.6) is removed since inertial effects can be neglected in the low Reynolds number regime, since the momentum relaxation time becomes short (<1 μs) [298].

In the same way as molecular collisions give rise to translational Brownian motion, they can also give rise to *rotational* Brownian motion. This expresses itself as a stochastic torque that causes the particle to randomly change its orientation. Such a process becomes especially important for anisotropic particles [299]. The Langevin equation for rotational Brownian motion, including an externally applied torque $\mathcal{M}_{\mathrm{ext}}(\mathbf{r})$ reads [22]

$$\dot{\theta}(t) = -\frac{1}{\gamma_{\mathrm{r}}}\mathcal{M}_{\mathrm{ext}}(\mathbf{r}) + \sqrt{2D_{\mathrm{r}}}W(t). \tag{4.8}$$

Here, $\theta(t)$ is the rotation angle, whereas γ_{r} is the friction coefficient for rotational motion, and $D_{\mathrm{r}} = \frac{k_{\mathrm{B}}T}{\gamma_{\mathrm{r}}}$ is the diffusion coefficient for rotational motion.

4.3.1 Trapping stiffness

The translational Brownian motion of a particle inside the optical tweezers gives rise to positional oscillations. For small fluctuations, the force acting on an optically trapped particle is approximately linear. The strength of the restoring force acting on the particle in one dimension can, therefore, be described as a Hookean spring with spring constant k_{s}, i.e. its stiffness. Characterising the trapping stability of the optical tweezers (referred to as trap stiffness) is both an established method for calibrating and quality-testing optical tweezers, and for measuring valuable parameters such as force, viscosity, and temperature.

In the one-dimensional case of Equation (4.7) and in the linear regime where $F(x) = -k_{\mathrm{s}}x$, the Fourier transform of the stochastic positional fluctuations of the trapped particle sampled for a sufficiently long time t_{exp} generates an overdamped Lorentzian power spectrum according to

$$P(f) = \frac{|\tilde{x}(f)|^2}{t_{\mathrm{meas}}} = \frac{D_{\mathrm{t}}}{2\pi^2}\frac{1}{f_{\mathrm{c}}^2 + f^2}. \tag{4.9}$$

[2]The Reynolds number characterises the ratio between inertial and viscous forces on an object in a fluid. Nanoparticles are generally in the "low Reynolds number regime", where viscosity dominates over inertia. In such a laminar regime, the motion of an object is determined by only its momentary force, without any "memory". Reference [296] introduces the topic in a very accessible way.

Here, $f_c = \left(\frac{k_s}{2\pi\gamma_t}\right)$ is defined as the corner frequency of the Lorentzian, containing k_s as the trapping stiffness of the optical tweezers [300]. Consequently, we can obtain an expression for the trapping stiffness

$$k_s = 2\pi\gamma_t f_c. \tag{4.10}$$

By measuring a particle's positional fluctuations in the trap and Fourier transforming these, the power spectrum can be obtained. The corner frequency can thereafter be extracted by fitting the experimentally obtained power spectrum to Equation (4.9), and together with an estimate for the friction coefficient, the trap stiffness can be measured.

4.3.2 Hot Brownian motion

So far, the Brownian diffusion considered above has taken place in a homogeneous environment, where the particle is at equilibrium with its surroundings. This implies there are no gradients in any of the surroundings' properties. In Section 2.5 the fact that a plasmonic particle is significantly heated by light was introduced. This heating leads to strong thermal and viscous gradients in the particle's surroundings. This holds for any optically trapped particle and especially for metallic nanoparticles, due to Ohmic heating. It is not apparent from the homogeneous case how a Brownian particle in these temperature-induced non-equilibrium environments should behave, and another theory that captures this is needed.

Since the time scale for heat conduction is faster than the characteristic diffusion time of the particle, the surrounding gradient will be comoving with the particle. It turns out that the dynamics of such a particle can be well described by an effective temperature and viscosity in a homogenous medium, which gives the particle the same diffusive behaviour as the real heated one in the thermal gradient. This effective temperature and viscosity (giving rise to an effective diffusion coefficient) is discussed for translational motion in references [301, 302], and for rotational motion in [303].

Due to the fact that rotational and translational motion sample their environments differently (expressed as a more localised velocity flow field for rotational motion in reference [303]), the temperatures associated to translation ($T_{\mathrm{HBM,t}}$) and rotation ($T_{\mathrm{HBM,r}}$) will be different. They relate to each other and the nanoparticle surface temperature (T_{surf}) and surrounding (T_0) according to $T_0 \leq T_{\mathrm{HBM,t}} \leq T_{\mathrm{HBM,r}} \leq T_{\mathrm{surf}}$. The relationship between these temperatures has been verified experimentally by several independent experiments such as [34, 304, 305] and in **Paper S.II**.

4.4 Surface interactions

In the majority of the studies performed for this thesis, small particles are moving in close proximity to flat surfaces. In **Papers I** and **II**, stable confinement of metallic nanoparticles is obtained by balancing the destabilising radiation pressure component of the optical force with a repulsive force from a surface with the same charge polarity as the nanoparticles (Figure 4.3a). In this case, the three main force components are the repulsive Coulomb force, the attractive van der Waals force and the optical scattering force. In **Paper IV**, dielectric microparticles sediment at and move along a water-glass interface (Figure 4.3b). For microparticles, the forces

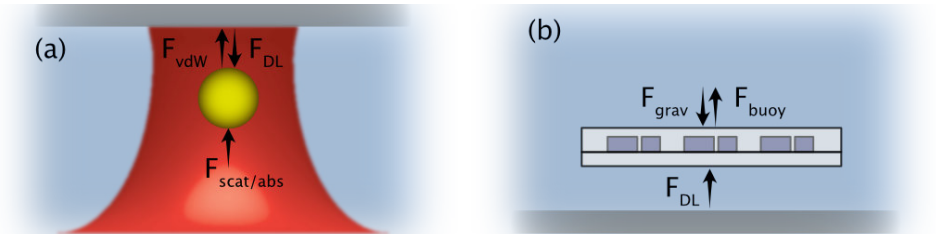

FIGURE 4.3: Decomposition of forces involved when nano- and microparticles approach charged surfaces. (a) A nanoparticle confined in 2D optical tweezers. Coulomb repulsion (F_{DL}, double layer repulsion) is counteracting the scattering force ($F_{\mathrm{scat/abs}}$). The short-range van der Waals force (F_{vdW}) also comes into play as the particle approaches the surface. (b) A microparticle that sediments on a surface at the water-glass interface. Gravity (F_{grav}) acts downwards while being counteracted by buoyancy (F_{buoy}) and Coulomb repulsion.

of gravity and buoyancy are non-negligible and balanced by the repulsive electrostatic force.

For both cases, in aqueous solutions the interaction and forces between charged surfaces, such as a particle and an interface, are described by the DLVO theory. The forces arise from interaction between charges in the objects as well as ionic layers at their surfaces and can be decomposed into two components; the van der Waals force (vdW) and the Coulomb force (double layer repulsion, DL) [306].

The van der Waals force results from the correlation between instantaneous multipolar (primarily dipolar) charge fluctuations of adjacent objects. For two single atoms or molecules, such interactions include only the two entities' dipoles. However, going to nanoparticles and even macroscopic bodies the interaction between all component multipoles needs to be summed to provide a measure of the force. Therefore, the vdW force is highly dependent on the shape of the interacting objects.

A surface in a liquid can become charged either by ionisation of its surface atoms or by adsorption of ions from solution. This surface charge will attract oppositely charged counter-ions, some of which will bind to the surface in a so-called Stern (or Helmholtz) layer, whereas others form a diffuse electric double layer as an atmosphere around the particle. Such charged counter-ion clouds are responsible for the repulsive force between objects in solution. Relevant measures for the strength and range of these repulsive forces are captured in the zeta potential and the Debye length. These describe the potential difference between the edge of the stabile counter-ion cloud and the surrounding medium, and the thickness of the double layer, respectively. Double layer forces can in general be derived from the Poisson-Boltzmann equation, and the special case of a spherical particle near an interface is approximately obtained through the Derjaguin approximation, both of which are outlined in detail in reference [306].

Lastly, as a particle performs Brownian motion near an interface, the drag that it experiences increases as it gets closer to the surface, because of the surface's no-slip (sometimes partial-slip) boundary condition [307]. The drag coefficients are different for different degrees of freedom (i.e. translation or rotation, parallel or perpendicular to the surface) and each can for a spherical particle be approximated using Faxén's laws [308, 309].

Chapter 5

Research methods

Any hypothesis proposed in science needs to withstand rigorous scrutiny of both experimental and numerical nature. To take a research project from conception to a finalised article requires a brimming toolbox of methods. Generally, when an idea for a nano-optics study is conceived a nanostructure first needs to be optimised, often via numerical simulations. After finding an optimal structure, it needs to be realised experimentally using nanofabrication techniques. Thereafter, characterisation measurement ensues to verify the study's hypothesis. These are usually optical experiments but can also include additional simulations. The chapter below follows the chronological outline of such a generic research project and introduces standard techniques as well as methods specific to the appended papers.

5.1 Numerical simulations

To design and optimise a nanostructure's optical response a prudent first step is with numerical simulations. As mentioned in Chapter 2 there are several techniques used in nano-optics. Yet, the one that has become most prevalent within the research community and hence also used in this thesis is the finite-difference time-domain (FDTD) approach. Here, Maxwell's equations are solved in a discretised cubic coordinate system by iteratively stepping forward in time. Since the method is performed in the time-domain with a broadband pulse the spectral response of the simulated structure is accessible through a Fourier transform. A more thorough introduction of the technique is beyond the scope of this thesis and further details can be acquired in reference [310].

All FDTD simulations performed for the thesis were done using the commercial software Lumerical FDTD Solutions. The shape and material composition of the nanostructure is built using computer-aided design, the boundary conditions and meshing properties are decided, whereupon the equations can be solved and fields extracted on predefined surfaces. The FDTD simulations for **Papers I** and **II** were performed by Dr. Nils Odebo Länk and Dr. Denis Baranov was responsible for the ones in **Paper IV**. I performed the simulations for **Paper III**, where polarisation-resolved transmission through polymer nanofins in a periodic lattice was carried out to optimise the PB polarisation conversion efficiency at different optical wavelengths.

Moreover, thermal simulations have been of importance for the thesis. These have been performed with the finite element method (FEM) in COMSOL Multiphysics software, by Dr. Steven Jones. An introduction to this can be found in [96, 311].

5.2 Nanofabrication

The ability to structure matter with nanometric precision has enabled nanoscience to flourish, with nano-optics being only one of the areas where *nano* is now a common prefix. Nanofabrication is often divided into either bottom-up or top-down techniques, where molecules are made to assemble into complex shapes or bulk matter is artificially nanostructured by removing excess material, respectively. However, in the thesis' context, it is rather more instructive to make the distinction between the fabrication of nanoparticles in colloidal suspensions (**Papers I, II** and **IV**) and surface-bound nanostructures (**Paper III** and partly **Paper IV**). Naturally, a field as vast as nanofabrication will only be cursorily introduced here, and more details can be found in the following books [175, 312, 313].

5.2.1 Surface-bound nanostructures

In 1959 Richard Feynman boldly challenged the scientific community to enter the realm of nanoscience in his iconic lecture "There's Plenty of Room at the Bottom" [314]. Not only did he inspire his contemporaries, but also managed to predict with impressive accuracy many of the fabrication processes critical to modern top-down nanofabrication. To fabricate a surface-bound nanostructure is a sequential process where one or several functional layers are patterned and partly removed to successively build the final nanostructure. A procedure consists of many detailed recipe steps and tools, all with technical names and acronyms; however, each layer usually consists of lithographic patterning, material deposition and pattern transfer via etching or lift-off, in different combination and order (Figure 5.1):

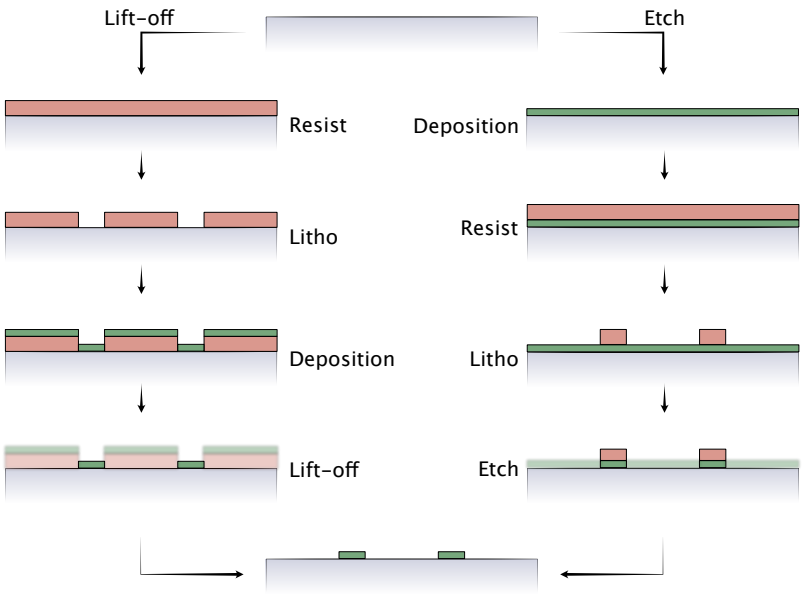

FIGURE 5.1: An overview of the two most prevalent nanofabrication processes, namely lift-off (left) and etching (right). Both processes are ideally initiated on a planar substrate (which can have previously been structured). The lift-off process then proceeds to coat the substrate with a suitable resist (red), followed by a lithography step to define the desired pattern. After the pattern has been exposed, the target material (green) is deposited, usually via evaporation. The sample is then submerged in a developer which dissolve the remaining resist and undesired target material, leaving the layer finished. The etch process instead starts by depositing a thin film of the target material, followed by a layer of resist. Thereafter, a lithographic step defines the pattern which subsequently can be transferred to the target material via an etching step.

- **Material deposition:**

  Any nanofabrication procedure starts from a pristine wafer or slab of material. Patterning can be done straight into this bulk substrate; however, the substrate is mostly used as a support structure. Instead, the material of interest is often deposited onto the wafer to form high-quality thin films that then can be patterned. Techniques for material deposition are plenty but can roughly be subdivided into chemical- and physical vapour deposition (CVD and PVD). Both have benefits depending on the intended material deposited and are used throughout this thesis. For example, low-pressure CVD and subsequent thermal annealing are used to deposit low-loss polycrystalline silicon films that are patterned in **Paper IV**.

  Soluble elements, in this context often polymers, are commonly deposited using spin-coating. This is routinely used to coat (potentially large-scale) surfaces with light- or electron-irradiation-sensitive resists which are subsequently used in a lithographic step to transfer a pattern to another functional layer. Depending on its chemical composition, a resist can be classified as positive or negative, if it becomes either more or less soluble in a developer after irradiation. Albeit often used as an intermediate step, resists can also have useful optical properties for nano-optics applications. In **Paper III**, a method that uses the patterned resist itself as building-blocks for PB metasurfaces is presented.

  Material deposition can also be performed after a lithographic step. Through a lift-off process, the deposited material only remains in predetermined areas where the resist had selectively been removed during the lithography. Due to its non-conformal step coverage which leaves side-walls uncovered, the PVD technique of evaporative deposition is often preferred here [315]. The remaining deposited material can either be the material of interest for the intended application (e.g. gold forming plasmonic nanoparticles) or a robust etch mask for further processing (e.g. nickel used in **Paper IV** to mask the final microparticle etching).

- **Lithography:**

  A desired nanoscopic pattern can be written in the resist by lithographic techniques with sufficient pattern transfer resolution, which include among others photo-, imprint-, and electron-beam lithography. In nano-optic research, where critical dimensions are often below one hundred nanometers, the most prevalent technique is electron-beam lithography (EBL). Hence, it is the technique used in **Papers III** and **IV** to expose patterns. However, due to its high cost and low throughput speed, EBL is not suited for assembly-line manufacturing, but it is ideal for the often small batches and flexible demands in a research environment.

  By rasterising a focused electron beam across the resist-covered substrate, a 2D pattern with a minimum feature size of around ten nanometers can be inscribed in the resist. When the exposed sample is subsequently submerged in a developer, the positive or negative image of the desired pattern will be dissolved to reveal the underlying substrate. This is now accessible to either deposit the target material or for removing the exposed underlying layer with etching [316].

Another lithographic technique worth mentioning is hole-mask colloidal lithography [317]. Here, charged colloidal polystyrene beads are made to self-assemble on a surface in a quasi-periodic monolayer. These beads then define a mask for either lift-off or etching as discussed above. The technique has been used extensively in past studies by the Käll group to construct optical metasurfaces [318–320], and again by me for the work performed in **Paper S.XII** mentioned in Section 2.2.2 and **Paper S.VIII** discussed below. A benefit of the technique is that it can easily be upscaled to a fraction of the cost of other techniques with similar resolution. Nevertheless, being a self-assembly technique, the possible patterns are limited compared to regular top-down approaches, although clever augmentations to the technique continue to be invented [321].

- **Etching:**

  A technique used for creating art historically, etching is nowadays an essential step in micro- or nanofabrication to transfer a pattern in a masking layer into an underlying target material. An etchant is chosen because it reacts with the target material to form volatile compounds that subsequently desorb from the surface [313]. For example, halogen elements (group 17 in the periodic table; Cl, F, Br, etc.) are well suited to etch dielectric materials. Moreover, etching methods can be subdivided into those that use either liquid or gaseous active compounds (wet or dry etching, respectively). During wet etching, the sample is simply submerged in the etching compound. Dry etching is most commonly performed in reactive ion etching (RIE) configurations where a plasma of the etch gas is formed and ionised molecules are accelerated towards the substrate.

  Moreover, etching can be either isotropic or anisotropic, meaning that it removes material equally in all directions or preferentially in one specific direction. Both can be useful, depending on the fabrication needs. For example, in **Paper IV** anisotropic etching was used to excavate the silicon metasurface whereas isotropic etching was used to release microparticles from its sacrificial substrate. Wet etching techniques can be anisotropic e.g. by the active compound reacting differently on different crystalline facets, whereas dry reactive ion etching often gains its anisotropy from both directionally incident ions as well as non-reactive compounds formed on the vertical surfaces during etching. When performing RIE the anisotropy of the etch is dependent on a range of parameters, including etch gas composition, plasma energy, acceleration voltage, pattern density, etc., and finding the optimal recipe for obtaining vertical side-walls can be time-consuming.

  Lastly, it is important to consider the etch selectivity between the material that is being removed and the mask layer. For some etch procedures a resist can form a non-reactive and well-suited etch mask, while some etching requires a more robust mask such as SiO_2 or a metal such as Ni or Cr. This then entails an additional lift-off step before the etch to produce the mask.

Controlled structuring at these small length scales often becomes complicated and even the seemingly simplest step can cause issues. An illustrative example of this is when drying a sample from water. The high interfacial tension of water can result in forces sufficient to deform and destroy sensitive nanostructures. To solve this issue one can beautifully utilise a fundamental thermodynamic property, namely the supercritical state of matter where the liquid and gas phases coexist

and the interfacial tension attributed to the phase transition vanishes. In *critical point drying* the water is replaced by liquid carbon dioxide which is heated and pressurised to become supercritical and then purged from the chamber to leave a dry and intact nanostructure [322]. The technique proved crucial in **Paper III** where it was used to obtain high aspect ratio nanostructures and efficient metasurfaces. If regular drying was used after the resist metasurface had been developed, the tall and tightly packed nanofins collapsed. Most supercritical drying use either acetone or isopropanol as an intermediate liquid since both CO_2 and water is soluble in these. Unfortunately, these intermediate liquids dissolve the resist studied. However, a surfactant-modified hexane solution can be used as an intermediate liquid that does not dissolve the resist metasurface.

Furthermore, depending on the complexity of a nanostructure, a multitude of parameters can influence both the fabrication procedure and finally its optical properties. Therefore, despite having found an optimal design for a particular task with numerical simulations it is common that some additional experimental optimisation is needed. By fabricating various nanostructures with small perturbations around the numerical optimum the figure of merit can usually be refined further. Figure 5.2 demonstrates such an approach for two cases where either a fabrication parameter (EBL dose) or the constituent particle's dimensions were varied.

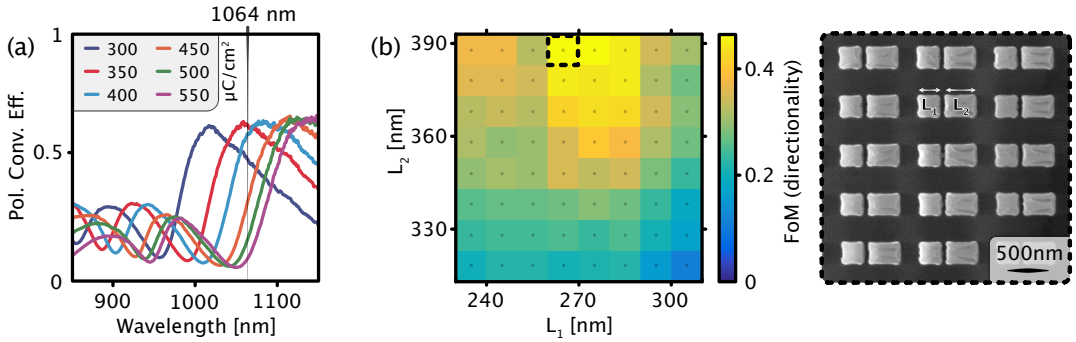

FIGURE 5.2: A simulated optimal nanostructure often benefits from some refinement using complementary experimental optimisation. (a) Shift of polarisation-conversion spectra for transmissive silicon PB metasurfaces (Section 5.3.4) fabricated with different doses of electron beam exposure. For an operation wavelength of 1064 nm, the optimal dose is ~350 μC/cm^2. (b) Figure of merit for beam steering metasurfaces measured by Fourier microscopy (Section 5.3.5). In **Paper IV**, transmission asymmetry between the ± 1 diffraction orders ($\mathcal{T}_{+1}$, $\mathcal{T}_{-1}$) is key to large momentum transfer and therefore the figure of merit is defined as FoM = $(\mathcal{T}_{+1} - \mathcal{T}_{-1})/\mathcal{T}_{\text{bkg}}$, where $\mathcal{T}_{\text{bkg}}$ is the background transmission. When varying both element's length, the FoM is seen to be maximised for the length combination of $L_1 = 265$ nm and $L_2 = 385$ nm. An SEM image of the optimal structure is shown on the right.

5.2.2 Colloidal suspensions

Chemical synthesis of metallic nanoparticles has been performed for centuries. Predating the understanding of resonant nanoparticles, both Roman and medieval artists used plasmonic effects to obtain vivid colours in cranberry glass (e.g. the Lycurgus cup) and stained church windows (e.g. Notre Dame's rose windows), respectively. That the vivid colours are attributed to metallic nanoparticles formed around small seeds when metallic salts are reacting with a reduction agent to form single-crystalline nanoparticles was first suggested by Faraday in 1857 [323]. Since then so-called seed-mediated wet-chemical growth of metallic nanoparticles has

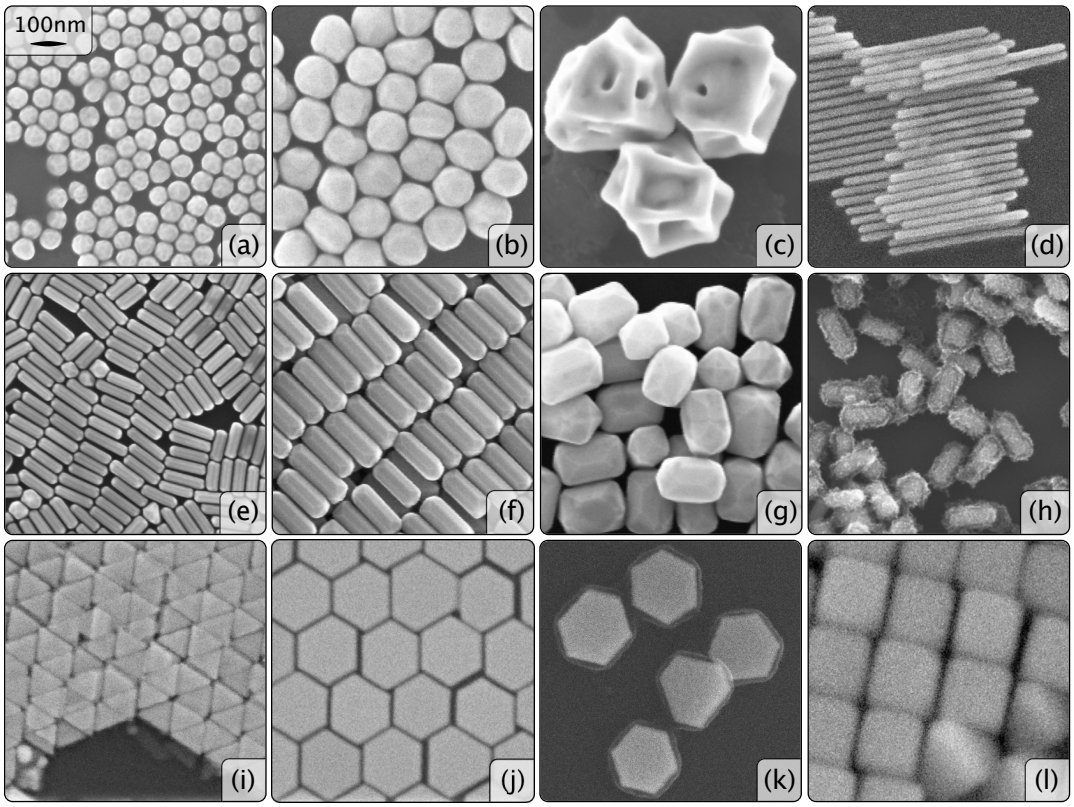

FIGURE 5.3: A sample of shapes and sizes of colloidal gold nanoparticles attainable through wet-chemical synthesis. (a-b) Nanospheres of different diameters, (c) nanostars, (d) nanowires, (e-g) nanorods of different aspect ratios, (h) core-shell nanorods with gold core and TiO_2 shell, (i) triangular nanoplates, (j) hexagonal nanoplates, (k) core-shell nanoplate with gold core and SiO_2 shell, and (l) nanocubes. The synthesis was performed by Dr. Lei Shao (a-c,e-h) and Dr. Ximin Cui (d,i-l). The scale bar in (a) is valid for all subfigures.

been explored in detail [324, 325], specifically driven by the strong interest in nano-optical applications. In particular, the realisation that different crystalline facets will lead to different growth rates and that these can be controlled by face-selective capping agent surfactants has enabled an abundance of differently shaped nanoparticles to be constructed [77, 325–328]. Figure 5.3 exemplifies part of the diverse range of nanoparticles available when using seed-mediated wet-chemical synthesis.

In **Paper I**, gold nanorods were used as rotary nanomotors driven by circularly polarised light. These were synthesised in-house by Dr. Lei Shao using seed-mediated growth and anisotropic etching similar to what is presented in reference [325]. In **Paper II** a batch of simple prototypical gold nanospheres were acquired from a company (Sigma-Aldrich) and its Brownian motion and optical characteristics were studied in the vicinity of the glass surfaces in the 2D trapping geometry introduced in Chapter 4. Hence, bottom-up colloidal synthesis was in this thesis exclusively used to produce gold nanoparticles and, accordingly, most discussion below is concerned with this metal. However, colloidal nanoparticles can be synthesised with silver [329, 330], palladium [330], metallic alloys [331], and as core-shell structures [332] as well.

From Chapter 2, we know that the final shape of the nanoparticle significantly influences its optical properties. For instance, the spectral position of the longitudinal LSP resonance is proportional to the length of a nanorod. Hence, if a

specific wavelength of operation is desired for an application it becomes important to produce nanorods with precise dimensions. Fortunately, as long as the nanorod is longer than required it is possible to perform post-growth anisotropic oxidation to selectively shorten the rod and pick the resonance position with precision [333]. Such an approach was used in **Paper I** to optimise the overlap between the nanorod's spectrum and the excitation laser to maximise the photothermal effects investigated.

For the colloid to be stable and to avoid aggregation of nearby nanoparticles a stabilising surfactant is commonly required, which forms a repulsive double-layer around each nanoparticle. The most prevalently used growth recipe, as introduced by J. Turkevich [334] and later refined by others [335, 336], uses sodium citrate to both reduce a gold salt precursor ($HAuCl_4$) and thereafter stabilise the final colloid. However, for directed growth citrate is not ideal since it is not facet-specific. Instead, an ammonium-based surfactant named Cetrimonium bromide (CTAB) is often used both as a directive and post-growth stabilising agent [77, 325, 337]. Unfortunately, CTAB-functionalised nanoparticles can be cytotoxic [338] and it is therefore often desired to replace it with some other surfactant when biological applications are intended. Due to the strong affinity between sulphur and gold, thiol molecules (–SH) are often used as end-groups to organic molecules that bind efficiently to gold [339]. Therefore, with a thiolated end-group, both long-chained polymer and DNA molecules have become commonplace for customisable functionalisation of gold nanoparticles [77].

Colloidal nanoparticles in solution are in many ways synonymous with bottom-up fabrication and wet-chemical synthesis, due to the ease at which large amounts of single-crystalline monodisperse nanoparticles can be made. However, despite the impressive advances in chemical synthesis during recent decades, the attainable shapes, material compositions, and sizes of particles are still limited. To widen the range of colloidal nanoparticles one can utilise top-down fabrication here too. In MEMS fabrication, the release of parts of a complex nanostructure is commonplace and usually performed by dissolving a sacrificial layer on which the nanostructure of interest has been fabricated using lithographic techniques as discussed above [340]. These techniques have also been successfully adopted to realise complex colloidal particles [341]. Such an approach has been used to construct specialised microparticles with embedded nanostructures for light-matter momentum exchange [253, 342], and in **Paper IV** it was used to release SiO_2 microparticles with embedded directional silicon metasurfaces.

With the current development in nano-optics – moving from metallic nanostructures to high-index dielectric ones – an increased demand is seen for cost-efficient and flexible synthesis of HID nanoparticles with variable shapes. As for its plasmonic counterparts, chemical synthesis of HID nanostructures improves at an impressive pace [343–346] and hopefully within a decade a variety of nanoparticles can be routinely self-assembled. However, to meet the present increased demand, top-down fabrication and release of HID nanoparticles can prove useful. In **Paper S.VIII**, one such fabrication procedure was explored to make large-scale silicon metasurfaces with nanoparticles that can subsequently be released into solution via wet-etching of a sacrificial layer (Figure 5.4).

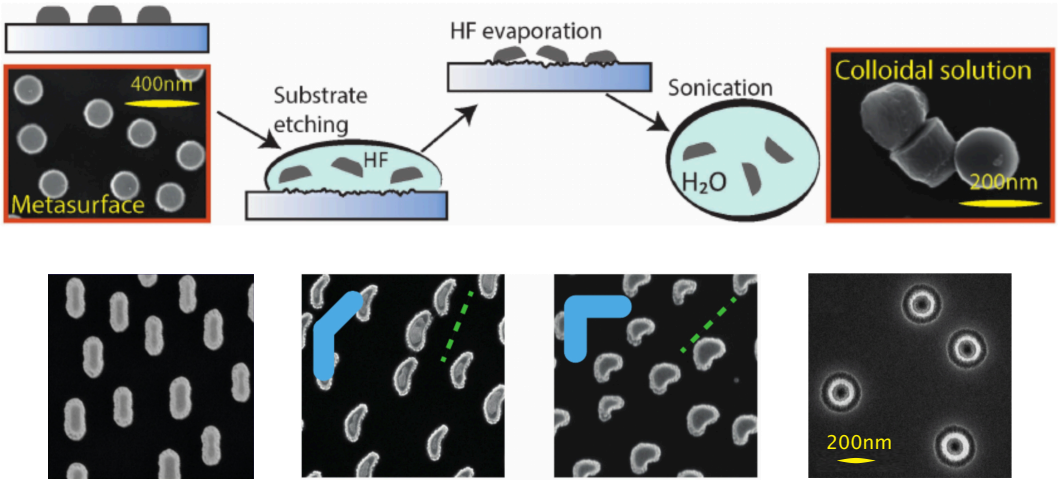

FIGURE 5.4: Summary of the results of **Paper S.VIII**. The hole-mask colloidal lithography technique [317] can be adapted to fabricate large-scale surface-bound metasurfaces of silicon nanoparticles. The nanoparticles can subsequently be released into colloidal suspension by etching an underlying sacrificial layer of SiO_2. Owing to the top-down fabrication approach, a wide range of complex shapes of released nanoparticles can be obtained. The figure is adapted with permission from [347] ©2018 John Wiley and Sons.

5.3 Optical characterisation

As with nanofabrication, there is no ubiquitous solution for optical characterisation of nano-optics systems and each project presents different challenges. Methods used in this thesis include optical tweezers and different kinds of microscopy and spectroscopy, with the most central ones introduced below.

5.3.1 Optical tweezing

Papers I and **II** relied heavily on 2D optical tweezing of metallic nanoparticles. The type of tweezers system used for these publications are similar to several previous publications from the Käll group [53, 276, 348]. To further spread knowledge about the technique's practical details, a method-paper (**Paper S.VI**) with an accompanying video was produced that outlines the setup and operation of such an optical tweezers system.

In summary, optical tweezers are constructed by collimating light from a sufficiently strong laser and directing it into a microscope objective. In both optical tweezing projects in this thesis, a 660 nm laser was used to form the trap. A colloidal sample with the nanoparticles of interest is prepared with a concentration of $\sim$5000 particles per μL to avoid interference between multiple particles, and then $\sim$5 μL of the solution is put in a sample cell in the microscope. Since metallic nanoparticles with strong absorption are studied, the laser is focused close to a microscope cover slide that has been prepared to provide sufficient Coulomb repulsion for particles to be stably confined in 2D without becoming printed on the glass surface.

To study the translational motion of the particle in the optical tweezers, a fast camera was used to record particles' translational Brownian motion in the trap. These fluctuations can subsequently be transformed into a power spectrum from which the trapping stiffness can be extracted. This is done following Equations

(4.9) and (4.10). The rotational motion of a non-symmetric particle can also be probed using power spectrum analysis; however, for this work, it is instead measured with autocorrelation of linearly polarised back-scattering from the trapped particles. Theoretically, a continuously rotating particle would generate an autocorrelation curve expressed as [276]

$$C(\tau) = I_0^2 + \frac{I_1^2}{2} \exp\left[-\frac{\tau}{\tau_0}\right] \cos(2\mathcal{N}\pi f_{\text{avg}}\tau). \tag{5.1}$$

Here τ is the correlation lag time, f_{avg} is the average rotation frequency, and $\mathcal{N}$ is the degree of rotational symmetry ($\mathcal{N} = 2$ for a rod). The term $\tau_0 = \frac{\pi\eta(T)\mathcal{G}L^3}{\mathcal{N}^2 k_{\text{B}}T}$ describes the autocorrelation decay time and provides information of the rotational Brownian motion. L is the long axis of a spheroid, T is the temperature in the surrounding liquid in the vicinity of the nanoparticle, and $\mathcal{G}$ is the shape correction factor introduced in Section 4.2. Hence, by fitting the theoretical autocorrelation curve to experimental data, information about the rotational dynamics and subsequently the temperature can be extracted.

5.3.2 Dark-field spectroscopy

Because of their strongly enhanced scattering, the most commonly used method for both observation and spectroscopy of single resonant nanoparticles is the dark-field (DF) configuration. Here, the illumination is such that only the scattering and not the incident light reaches the detector, providing a high signal-to-noise ratio for observation of individual nanoparticles against a dark background. When recording a raw spectrum $I_{\text{raw}}(\lambda)$ from a scattering nanoparticle it will not only contain the spectral characteristics of the nanoparticle, but also variations related to e.g. the illumination's spectral profile, detector response, and background signal. Hence, it is crucial to calibrate a spectrum before using it for interpretation. To do so, spectra for the white light illumination $I_{\text{white}}(\lambda)$, the background $I_{\text{bkg}}(\lambda)$ and the detector's dark counts $I_{\text{dark}}(\lambda)$ are recorded and thereafter the calibrated spectrum is obtained from

$$I_{\text{scatt}}(\lambda) = \frac{I_{\text{raw}}(\lambda) - I_{\text{bkg}}(\lambda)}{I_{\text{white}}(\lambda) - I_{\text{dark}}(\lambda)}. \tag{5.2}$$

Another signal that unavoidably arises when working with an intense laser in a 2D tweezing configuration is autofluorescence from the nearby glass slide [349]. By recording the background signal with empty laser tweezers the autofluorescence can be accounted for and does not corrupt the nanoparticle's spectrum.

From Chapter 2 we know that the nanoparticle spectrum contains plenty of information, which partly can be accessed by fitting a Lorentzian function to a resonance mode. From this, one can extract the peak position and full width at half maximum (FWHM), providing information about the nanoparticle's size, damping characteristics, surroundings, etc. Time-resolved nanoparticle sensing is then enabled by tracking the spectral evolution in time [6], as is done in **Paper I**. The Lorentzian can be expressed as

$$I(E) = \frac{1}{2\pi} \frac{\Gamma}{(E - E_0)^2 + (\frac{1}{2}\Gamma)^2}, \tag{5.3}$$

where $E = \frac{hc}{\lambda}$ is the energy expressed in terms of the speed of light c, Planck's constant h, and the vacuum wavelength. Γ is the full width at half maximum (FWHM) and E_0 is the Lorentzian's peak position.

5.3.3 Total internal reflection microscopy

As a scatterer is placed in an evanescent field, it will convert some of the exponentially decaying near-field radiation into far-field scattered light through a process called frustrated total internal reflection. The intensity of such scattered light depends on where in the decaying evanescent field the particle is located. By knowing the decay profile of the evanescent wave, and measuring the scattered intensity, it is possible to extract information about the separation distance between the surface and the scatterer. This is the base of a microscopy technique called *total internal reflection microscopy* (TIRM), which has been successfully used to probe a range of interactions between particles and surfaces [350–357]. In **Paper II**, a 514 nm laser was free-space coupled via a dove-prism to perform TIRM.

In order to reach a measure for the particle-surface separation distance, a translation between scattered intensity and height is needed. Previously, it was recognised that the height-dependent scattering followed the same exponential decay as the evanescent field, $I(h) = I_0 \mathrm{e}^{-\beta h}$. Here, h is the separation distance, I_0 is the incident intensity at the surface, $\beta = \frac{4\pi}{\lambda}\sqrt{n_{\text{glass}}^2 \sin^2\theta_i - n_{\text{water}}^2}$ is the reciprocal penetration depth of the evanescent field, expressed in terms of the refractive index of the two media n_{water} and n_{glass}, and the angle of incidence θ_i for the exciting light wave.

In an attempt to verify this exponential dependence, Mie calculations in the vicinity of an interface were performed by Dr. Nils Odebo Länk. By comparing the intensity-distance translation for collection from the water side of the interface from this Mie-model to the exponentially decaying model, a discrepancy manifested as an oscillatory trend is noted (Figure 5.5a). However, when the light is collected on the glass-side of the interface or if an anti-reflection coating is applied at the interface when collecting from the water-side, the oscillation goes away, and the exponential trend is present also for the Mie-model (Figure 5.5b). Therefore, the discrepancy for the collection geometry at hand is attributed to

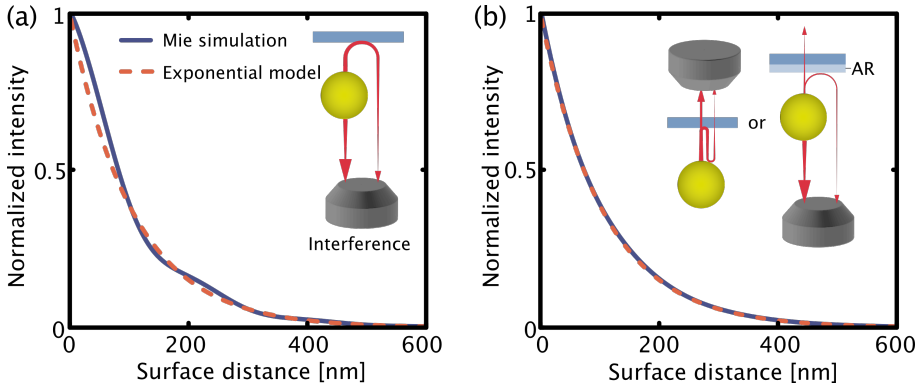

FIGURE 5.5: Scattered TIRM intensity from a 100 nm gold sphere near a glass interface. A Mie-model (blue) is compared to the previously used exponential decay model (dashed orange). (a) For light collected from the water side, the intensity-distance relation is deviating from exponential decay. This trend is explained from interference between directly scattered light with scattered and reflected light (see inset), which becomes negligible if one instead were to collect light from the glass side, or when using an anti-reflection coated surface (as shown in (b)).

interference between directly scattered light and light reflected once from the interface. Hence, for the intensity-distance translation performed in **Paper II**, a table obtained from the Mie simulations is used, rather than the exponential model.

5.3.4 Measurement of PB metasurface efficiency

A high transmission or reflection efficiency is essential for phase-gradient metasurfaces to eventually become a competitor to conventional optical elements. For PB metasurfaces we saw in Section 3.4.2 that the component of light that acquires a phase-shift also experiences a concomitant reversal of handedness. Hence, the first step in any metasurface optimisation process is to find the nanofin dimensions that produce the highest cross polarised transmission for circularly polarised light. This is equivalent to trying to find the configuration where $t_x = t_y = 1$ and $\varphi = \pi$ in Equation (3.11), where the metasurface acts as a perfect half-wave retarder.

The basic function of a half-wave retarder is to reverse the handedness of circularly polarised light or rotate the plane of linear polarisation. The linear polarisation plane turns two times the angle between the fast axis and its incident direction. Hence, the amount of circularly polarised light that reverses handedness (and acquires a PB phase) is equivalent to the amount of linearly polarised light that turns its polarisation direction. Experimentally, the second of these cases is much simpler since it involves only two crossed linear polarisers where the retarder is placed with its fast axis halfway between the two polarisers (at 45°). The light that passes through the crossed polarisers has thus been turned by the half-wave retarder and acquired a PB phase.

That these two cases are equivalent also for PB metasurfaces is verified with FDTD simulations of polarisation-resolved transmission spectra through a metasurface consisting of a homogenous array of nanofins placed at 45° (Figure 5.6). Since the

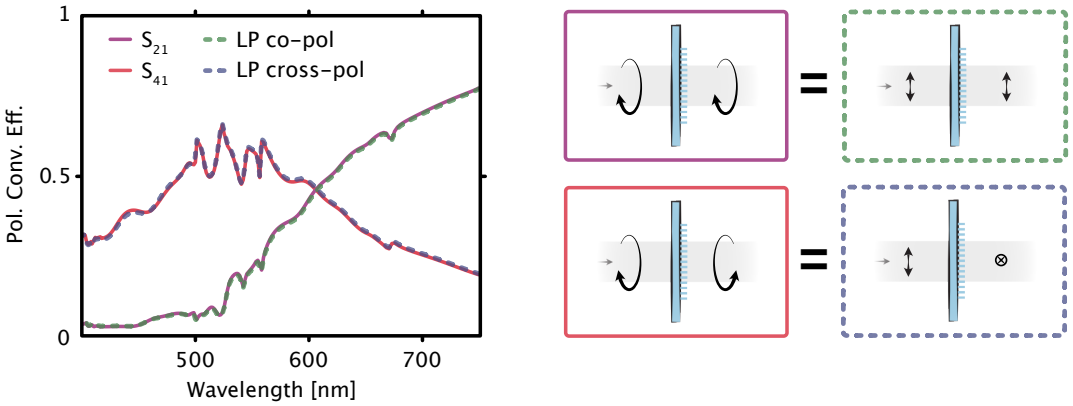

FIGURE 5.6: Polarisation-resolved transmission spectra from FDTD simulations for a polymer nanofin array optimised for operation at 532 nm light, from **Paper III**. When RCP light is sent in, the transmitted light is either still RCP (S_{21}, purple line), or reversed to LCP (S_{41}, red line) while acquiring a PB phase. When horizontal linearly polarised light is incident at an angle of 45° in relation to the nanofin's fast axis, part of the transmitted light remains horizontal (co-pol, green dash), and the rest is rotated by 90 ° (cross-pol, blue dash). That these spectra are identical justifies the validity of measuring linear cross-polarised transmission to gauge a PB metasurface's polarisation conversion efficiency.

spectra for these two cases are identical the linearly polarised approach to quantify the polarisation conversion efficiency is used in **Paper III**.

5.3.5 Fourier microscopy

In nano-optics, angles at which light is transmitted or reflected supply valuable information about a system. From image formation theory it is well known that the spatial and angular information of an image are related via the Fourier transform. Thus, any imaging system has both a set of conjugate focal planes and back focal (Fourier) planes. By projecting a back-focal plane onto a detector, the angular information content of the image is resolved as a decomposition of plane waves with each k-vector appearing as a point spread function in the image. This angle-resolved imaging technique is referred to as Fourier microscopy or back-focal plane imaging [358]. If a spectrum is taken at each position in the Fourier plane it is even possible to perform angle-resolved spectroscopy.

In **Paper III** and **IV**, Fourier microscopy was useful to investigate the beam-steering qualities of phase-gradient metasurfaces. In particular, for the asymmetric transmission metasurfaces studied in **Paper IV** the technique enabled us to quantify and optimise the metasurfaces to maximise the momentum transfer from light to matter (Figure 5.7). Since maximal momentum transfer is sought, a figure of merit is defined as

$$\mathrm{FoM} = \frac{\mathcal{T}_{+1} - \mathcal{T}_{-1}}{\mathcal{T}_{\mathrm{bkg}}}, \tag{5.4}$$

where $\mathcal{T}_{\mathrm{bkg}}$ is the background transmission (Figure 5.7a), whereas $\mathcal{T}_{+1}$, $\mathcal{T}_{-1}$ are transmission to the ± 1 diffraction orders (Figure 5.7b). For the particular metasurface, corresponding to the one imaged in Figure 5.2b, an FoM = 0.45 can be determined with Fourier microscopy.

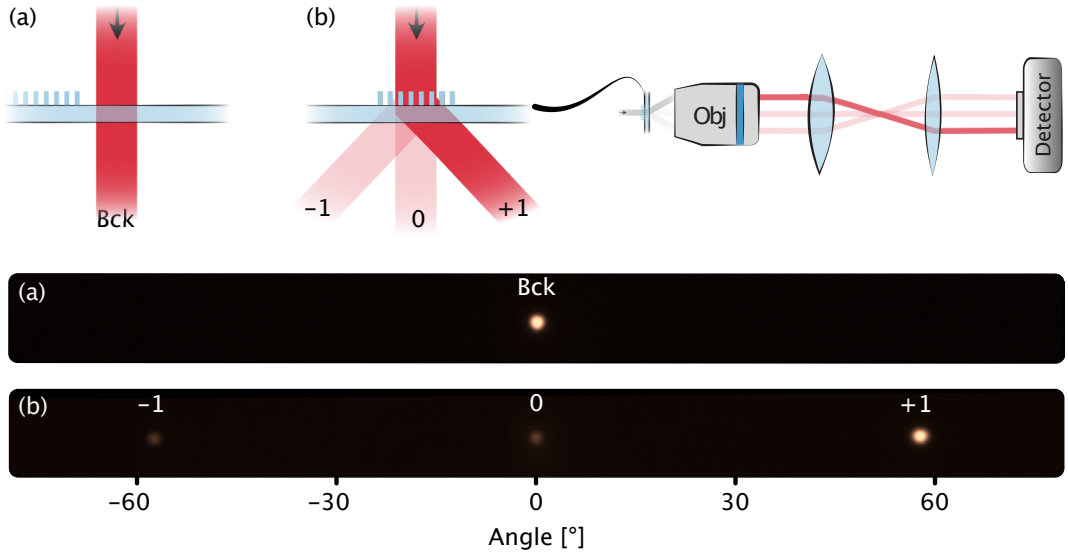

FIGURE 5.7: Fourier microscopy used to study the angular distribution of light interacting with nanostructures. (a) As normal incidence collimated light passes through a substrate undeviated only a single point shows up on the Fourier image. (b) As light passes through a beam-steering metasurface the main spot shift to the +1 diffraction order with only little light reaching the 0th and -1 orders. From this, the FoM for a range of metasurfaces can be investigated to find the optimal design.

5.4 Brownian dynamics simulations

The Langevin equation for translational motion is written according to Equation (4.7). This stochastic differential equation needs to be solved to obtain a Brownian particle's trajectory. A common way of solving this problem is through iterative methods, where the position at one time-step is re-evaluated to the next one by applying a stochastic term to either the position or the velocity of the particle. In **Paper II**, an approach to do this was used which produces a time-efficient solution by expressing the equation in Liouville operators [359] as outlined in reference [360]. One time-step in the algorithm is made by the four steps below, and the three-dimensional counterpart is solved by iteratively performing the four steps along each Cartesian coordinate axis.

Brownian dynamics simulation algorithm:

1. $\tilde{v}_{n+1} = \frac{1}{2}a_n\Delta t + \sqrt{c_0}v_n + v_{\text{th}}\sqrt{1-c_0}W_{1,n}$
2. $x_{n+1} = x_n + \tilde{v}_{n+1}\Delta t$
3. $a_{n+1} = \frac{F_{\text{tot}}(x_{n+1})}{m}$
4. $v_{n+1} = \frac{1}{2}\sqrt{c_0}a_{n+1}\Delta t + \sqrt{c_0}\tilde{v}_{n+1} + v_{\text{th}}\sqrt{1-c_0}W_{2,n}$

Here, $c_0 = \mathrm{e}^{-\gamma_{\text{t}}\Delta t/m}$, $v_{\text{th}} = \sqrt{\frac{k_{\text{B}}T}{m}}$, and $W_{1,n}$ and $W_{2,n}$ are Gaussian random numbers with zero mean, unit variance and that are uncorrelated in time.

The first step is the discretised analytical solution to the Langevin equation, solved at a half time-step without altering the position (Step 1). When the velocity for the time-step is estimated, that velocity is used to calculate the new position (Step 2). The total force F_{tot} at the current location of the particle is used to calculate its instantaneous acceleration (Step 3). For the specific case investigated in **Paper II** the total force is comprised of the surface dependent van der Waals and Coulomb force components estimated from [306], as well as an optical force component obtained from Mie calculations performed by Dr. Nils Odebo Länk. After the acceleration is found, the conclusive velocity for the time-step is estimated with another use of the discretised analytical solution of the Langevin equation (Step 4). The separated velocity calculation is a symmetric decomposition performed to reduce the errors of the method [360].

The hydrodynamic friction coefficient γ_{t} is for a sphere set by Stokes's law and is governed by the viscosity of the surrounding fluid and the radius of the particle. The value of γ_{t} is affected both by the presence of the surface and the fact that the metallic nanoparticle in the optical trap is performing hot Brownian motion. Therefore, the values going into the simulation routine take these effects into account.

To certify the correctness of the algorithm, the known case of freely diffusing Brownian spheres ($r_0 = 50$ nm) is tested. The external force term is set to zero, and the friction coefficient is made isotropic. The mean square displacement (MSD) in one dimension of such particles' positional fluctuations should be proportional to

time [22]. It relates as

$$\mathrm{MSD}_x(t) = \langle (x(t) - x_0)^2 \rangle \propto t, \tag{5.5}$$

where the brackets denote an ensemble average, $x(t)$ is the particle position at time t, and x_0 is a reference position for each particle. Figure 5.8 displays the MSD in each Cartesian direction for a freely diffusing particle simulated in the model above, and the expected relation is seen to hold. Moreover, the diffusion coefficient of a Brownian particle is related to the mean square displacement as $\mathrm{MSD}(t) = 2D_\mathrm{t}t$. From the data in Figure 5.8, the diffusion coefficient is estimated to 4.5 $\mu\mathrm{m}^2/\mathrm{s}$. This is found to be only 4% away from the analytically derived value for the diffusion coefficient ($D_\mathrm{t} = \frac{k_\mathrm{B}T}{\gamma_\mathrm{t}}$ [22]), and can be compared to the experimentally measured value of around 4 $\mu\mathrm{m}^2/\mathrm{s}$ for the nanoparticles used in **Paper II**. This agreement is reasonable, considering that experimentally the colloidal nanoparticles suffer from polydispersity and that their hydrodynamic radius is slightly enlarged by the stabilising double layer.

This algorithm is a general one for Brownian motion in several regimes, capturing both the initial ballistic and the subsequent diffusive states. The transition between these occurs on the time-scale of the momentum-relaxation time $\tau = m/\gamma_\mathrm{t}$ [298]. For micro- and nanoparticles in liquids this is usually below a single μs, and hence shorter than what most experimental detectors can capture. Therefore, in the diffusive regime, inertial effects can be disregarded and the mass-containing term in the Langevin equation (4.7) cancels out. To verify this, the diffusion coefficient is calculated for freely diffusing spherical particles of fixed size but with masses spaning three orders of magnitude. At the time of 0.5 ms, which is the time-limit for the detector used in **Paper II**, the diffusion coefficient remains at a value of around 4.5 $\mu\mathrm{m}^2/\mathrm{s}$ for all particles.

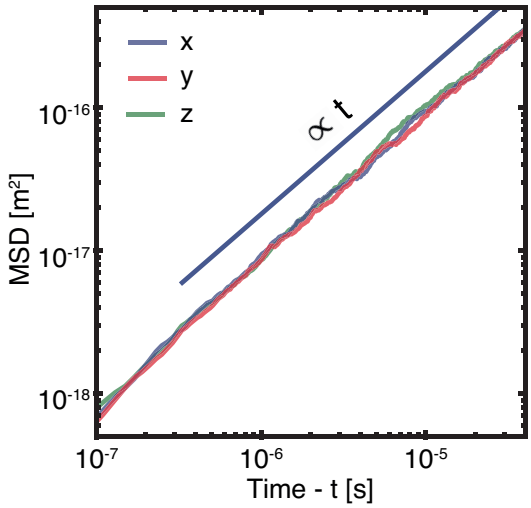

FIGURE 5.8: Mean square displacement for a freely diffusing 100 nm nanosphere. The MSD is proportional to time. From the MSD, the diffusion coefficient of the object can be obtained to 4.5 $\mu\mathrm{m}^2/\mathrm{s}$.

Chapter 6

Concluding remarks

Scientific output during doctoral studies can be seen as a product of the conducted experiments, the individual student's ability and curiosity, the available resources both in terms of infrastructure and colleagues, and the current scientific opportunities. Pragmatically, the output will in some way reflect all of these components. The condensed and objective scientific contribution of this thesis is presented in the appended papers. However, research is as much a personal endeavour as it is a scientific one and in the journal article format the multifaceted efforts of the research are somewhat lost. Therefore, this chapter attempts to summarise and discuss the papers in a wider, slightly more reflective format, and thereafter end with an outlook towards future undertakings.

Paper I

Probing Photothermal Effects on Optically Trapped Gold Nanorods by Simultaneous Plasmon Spectroscopy and Brownian Dynamics Analysis

As a new Ph.D. candidate, it is natural to look close to home for a first project. It is where the research group's expertise lies and where there is hopefully plenty of support and guidance. As I joined the group, the major ongoing project related to my interests was that of 2D trapping of metallic nanoparticles and specifically operating these as rotary nanomotors. Starting in the group, I contributed to **Paper S.I** where it was shown that nanorods can spin faster than 2.5 million revolutions per minute when driven with near-resonant circularly polarised light. Even though the inevitable temperature increase associated with laser trapping was accounted for in this publication, there were still thermal considerations that could be elucidated further.

Hence, for the first study of this thesis, we set out to study how photothermally induced effects alter gold nanorods as they are trapped in optical tweezers. Two independent yet complementary measurement techniques, namely photon correlation spectroscopy and dark-field spectroscopy were utilised to probe temporal changes experienced by the trapped nanoparticles. It was with single-nm resolution possible to discern nanorod reshaping of a few nanometres during 30-minute experiments. Furthermore, from the measurement channels, two gauges for the temperature of the particle's surroundings were obtainable, which both showed temperatures of water superheating to $\sim$230°C. These measurements were based on the analysis of altered rotational Brownian motion as well as LSP resonance peak shift, caused by the temperature-dependent viscosity and refractive index of the surrounding water, respectively.

Thermoplasmonic effects is a popular research area and this particular article has been cited in subsequent studies to exemplify both advantageous and detrimental photothermal effects. It was also useful locally in our research when using the trapping and rotation geometry for sensitive biological applications in **Paper S.IV**. Apart from furthering the community's understanding of photothermal effects at the nanoscale, this study also served an educational purpose for me personally. After completing the study I had constructed optical setups from scratch, performed optical tweezing and characterisation, and been exposed to a plethora of physics and data analysis that would be useful throughout the rest of my studies. Equipped with this I was ready to remove the training wheels and steer my research towards new innovative projects. But before that, one more question about the 2D trapping of metallic nanoparticles intrigued me, namely the influence of the nearby surface.

Paper II

Surface Interactions of Gold Nanoparticles Optically Trapped Against an Interface

It is well-known that the presence of a surface can affect a micro- or nanoparticle's movement and its thermal and optical properties significantly. Considering how prevalent the surface-based 2D optical trapping geometry is, it seemed surprising to find that the literature lacked detailed investigations about the nanoparticle-surface separation distance and ultimately the surface's influence on the dynamics and properties of a 2D trapped nanoparticle. In most studies, the nanoparticle is treated as if residing in a homogenous solution, and the surface is not accounted for.

To certify or falsify this presumption, experiments employing total internal reflection microscopy were carried out. After having installed a detector sensitive enough to capture the shot-noise limited signal, the distance separating a trapped gold nanosphere and the glass interface was measured to be between $\sim$30-90 nm, depending on laser power and double-layer force screening. An analytical force model was introduced that, when used as the external force in Equation (4.7), closely reproduces the experimentally observed positional fluctuations of a trapped particle. Once the exact separation distance is known, it is possible to draw conclusions about the surface's effect on a particle's dynamic and thermal behaviour. At these separation distances, a particle experiences a $\sim 10\%$ reduced temperature compared to in a homogenous water environment, due to the increased thermal conductivity of the nearby glass. Furthermore, its translational motion is significantly damped due to increased drag near the surface, while the rotational motion is only weakly affected.

For me personally, this study addressed a main fundamental physical question about surface-based 2D optical tweezing of metallic nanoparticles. Certainly, there are plenty of scientific questions left to study in similar systems; however, I felt that this one was important for me to address before moving on in my research. Since its publication in 2019, this article has so far attracted limited attention. However, with an idealistic view of science, one can argue that it is important to allow the pursuit of answers to even seemingly minor questions. In that sense, this was my most curiosity-driven project. Hopefully, in the future, this study's findings will prove useful for someone else posing a related question.

Paper III

Large-Scale Metasurfaces Made by an Exposed Resist

During the early years of my graduate work I intently followed the progress of the field of flat optics and phase-gradient metasurfaces. It seemed to be a fascinating topic with plenty of potential for both scientific breakthroughs as well as industrial applications. Recognising that this field too is based on momentum transfer, I decided to continue my research by exploring it in the context of optical forces and torques. To do that it was paramount to establish a procedure to reliably build phase-gradient metasurfaces. During an exploratory phase of nanofabrication, we realised that off-the-shelf EBL resists had optical properties that could potentially render them useful as the very construction material for flat optical components. Since this idea was absent in the literature and could be of use for the community, we decided to veer from the intended course and perform a more comprehensive study of this system.

Early results showed promising results of beam-steering and near-diffraction-limited lenses. However, it was soon realised that due to the comparably low refractive index of polymers, metasurfaces with transmission efficiencies exceeding 10% eluded us. This was because efficient metasurfaces required high aspect-ratio particles, which collapsed under capillary forces during post-development drying. The project's turning point was the realisation that taller meta-atoms could be fabricated if supercritical drying in a CO_2 environment was performed, avoiding the liquid-gas phase transition and therefore any detrimental interfacial tension. Thus, metasurfaces with transmission efficiencies above 60% could be obtained, facilitating the fabrication of efficient high-NA lenses, substrate-independent metasurfaces, as well as flexible and macroscopic optical elements. Further benefits of the technique are that it is faster, cheaper, and safer than conventional metasurface fabrication techniques, which today often rely on multiple steps of material deposition, patterning, and etching.

In terms of scientific impact, not sufficient time has passed to objectively gauge if the idea will prove useful for the community. However, as it was published, the paper attracted conciderable attention in regular media as well as from potential industrial collaborators, hence serving a parallel purpose of science outreach. Moreover, the fabrication technique has since been used to fabricate metasurfaces used in **Paper S.XIV**, and for an additional ongoing study. Nevertheless, if industry-wide adoption of flat optics will happen, it will likely rather be based on scaleable and robust techniques such as UV-lithography or nano-imprint lithography, rendering EBL superfluous in fabrication.

Paper IV

Microscopic Metavehicles Powered and Steered by Embedded Optical Metasurfaces

Entering the phase-gradient metasurface field with an optical manipulation background made us realise the untapped potential in using metasurfaces as a means to derive motion from beam- and polarisation-manipulation even of plane waves. In the community, metasurfaces are mostly seen as stationary objects that manipulate light. However, beam shaping metasurfaces could, instead of the preceding optical components, take on the responsibility of producing complex optical momentum distributions resulting in optical forces and torques.

Engineered metasurfaces could then in some contexts lessen the stringent requirements on focused beams for optical manipulation.

Metasurfaces based on anisotropic silicon dimers were fabricated to function as polarisation-sensitive asymmetric diffraction gratings, steering light preferentially to the +1 diffraction order. Being anisotropic, the metasurface also converts the polarisation of reemitted light, resulting in a torque that aligns the long axis of the dimer to the polarisation plane of the incident light. By embedding this metasurface into a microparticle, we demonstrated that the momentum exchange results in forces and torques sufficient to drive and steer these objects. In unfocused light beams with an average light intensity of only $\sim$10 μW/μm^2 the metasurfaces move at speeds of above 10 μm/s. These so-called metavehicles were subsequently shown to perform controlled complex motion and could even function as transport vehicles for microscopic objects of both inorganic and biological character.

At the time of writing, the manuscript for this project is under review and hence its impact and influence is yet to be determined. However, considering the vast amount of metasurfaces studied in the community, there is ample opportunity to investigate their incorporation into scaled-down and dynamic systems where the full potential of momentum exchange between light and matter can be exploited.

Outlook

As eloquently illustrated by Prof. Matt Might; if one can view the world's aggregate knowledge as a sphere, the work embodying a Ph.D. is to expand this sphere by a minuscule amount in some specific direction [361]. In the last 20 years or so the science of nanophotonic systems has interdisciplinarily provided expansion in several directions, including physics, chemistry, and biology [362], and the study of optical forces and torques dates back even further. I hope that this thesis' work has somehow aided said expansion within both nanophotonics and optical manipulation, and that it will help inspire research to come. However, in line with the aphorism "The more you learn, the more you realise how much you don't know.", an expanding sphere of collective knowledge inevitably unlocks new questions as well as opportunities. These can roughly be grouped into either fundamental or application-oriented, and possible continuations of this thesis include both. Proposed continuations of each specific project are outlined in the concluding paragraph of each article, whereas here a broader view is taken.

Even the seemingly simple system of small particles confined by light is still subject of investigation from a fundamental perspective. Plenty of effort has been exerted to modify and widen the capabilities for optical manipulation; either by more exotic light fields such as Airy [363] or Bessel beams [364], or by the tailored optical response of nanoparticles to realise for example pulling forces [365], topologically enabled continuous rotation [366], and lateral forces perpendicular to light's propagation direction [367, 368]. Although theoretically more complex than ordinary optical tweezers, such systems could provide additional degrees of freedom for optically mediated manipulation.

Moreover, if multiple particles are confined in the same loosely focused beam, their interactions with light and each other result in optically bound aggregates [369–371]. These, sometimes referred to as optical matter, display interesting dynamics and if conditions are right the collective scattering even gives rise to

something as counterintuitive as negative optical torque [372]. Potentially, the techniques and results from **Papers I** and **II** could prove useful in further elucidating such dynamics. It would be interesting to study how anisotropic nanoparticles fair in such environments and what role photothermal effects or the vicinity to a glass interface plays.

Optical manipulation and force sensing with micron-sized dielectric spheres has long been a workhorse in the study of biological systems, and today there are multiple companies (e.g. Lumicks, JPK Instruments, and Boulder Nonlinear Systems) even providing turnkey optical tweezers systems. With the increasing fundamental understanding of resonant nanostructures and their enhanced optical forces and torques, it is desirable to demonstrate potential commercialisable applications of such systems as well. For instance, metallic nanoparticles in optical tweezers can be used in nanosurgery for precise injection of active substances or medicine into single cells [107, 373]. Other intriguing suggested applications include resonantly improved nanotweezers geometries based on field enhancement of surface-bound nanoantennas of both plasmonic [374] and dielectric [375] kind, novel nanofabrication platforms based on localised photothermally induced curing of polymers [38] or optical printing of individual nanoparticles [51], and high-resolution surface imaging with optically trapped nanoparticles [376].

Furthermore, with the current interest in high-index dielectric nanoparticles, a natural query is how they can augment optical forces and torques. Their lower absorption together with their rich optical response endowed by having both electric *and* magnetic resonances in the visible to NIR regime could lead to interesting behaviours [377]. Despite being suggested as a route to reduce radiation pressure forces, the overlapping magnetic and electric resonances fulfilling the first Kerker condition does not seem to contribute particularly to trap stability [378]. Nevertheless, for applications where reduced photothermal heating is required, the lower absorption of high-index dielectric and particularly silicon nanoparticles under NIR illumination is superior to its metallic counterparts [264]. These early results are sufficiently promising to warrant future investigations into high-index dielectric nanoparticle optical manipulation. Moreover, by making use of effective-medium metamaterials, the optical response and subsequently manipulation of dielectric nanostructures can be modifiable, potentially to fit the needs of particularly demanding applications [379]. Such an idea, to use top-down nanofabrication to engineer the optomechanical response of micro- and nanoparticles, is similar to what was performed in **Papers III** and **IV**, and maybe the fabrication procedure explored here can further be used in this context.

Despite being related via the overarching topic of light-matter momentum transfer, **Paper III** is to some extent the odd one out in this thesis. It is concerned with the fabrication of static and large-scale phase-gradient metasurfaces for the potential replacement of refractive optical components with metasurface counterparts. Such flat optics likely have a bright future ahead, partly eluded to in the outlook provided in the concluding section of Chapter 3. However, at its heart, this thesis is concerned with optical forces and torques on matter. The usefulness of metasurfaces in this context is more clearly exemplified in **Paper IV**, which provides a first experimental demonstration that metasurfaces are capable of providing stable propulsion due to optical momentum exchange. Going forward it is easy to envision other functionalities that could be included into these dynamical

metasurfaces, to make more multifunctional optically driven microscopic robots. For example, flat lens-based or plasmonic optical tweezers could be constructed ”on board” to supply more functions related to the demonstrated transport capabilities. Another possible function that easily could be added is a plasmonic antenna to perform non-stationary molecular sensing experiments. Moreover, a range of different phase-gradient metasurfaces can be explored to produce even more freedom of motion, including the direction of travel (forwards/backwards) and variable turning radius. One particularly interesting realisation of stationary phase-gradient metasurfaces has been performed in reference [380] where optically multiplexed holograms were designed based on orbital angular momentum encoding. If such metasurfaces were embedded into metavehicles, a range of driving modes for the same particle and wavelength could be designed.

Bibliography

1. Hecht, E. *Optics* (Pearson Education, 2016).
2. Khattak, H. K., Bianucci, P. & Slepkov, A. D. Linking plasma formation in grapes to microwave resonances of aqueous dimers. *Proceedings of the National Academy of Sciences* **116,** 4000–4005 (2019).
3. Bharadwaj, P., Deutsch, B. & Novotny, L. Optical antennas. *Advances in Optics and Photonics* **1,** 438–483 (2009).
4. Maier, S. A. *Plasmonics: fundamentals and applications* (Springer Science & Business Media, 2007).
5. Novotny, L. & Hecht, B. *Principles of nano-optics* (Cambridge University Press, 2012).
6. Anker, J. N. *et al.* Biosensing with plasmonic nanosensors. *Nature Materials* **7,** 442–453 (2008).
7. Huang, X., Jain, P. K., El-Sayed, I. H. & El-Sayed, M. A. Plasmonic photothermal therapy (PPTT) using gold nanoparticles. *Lasers in Medical Science* **23,** 217 (2008).
8. Ghosh, P., Han, G., De, M., Kim, C. K. & Rotello, V. M. Gold nanoparticles in delivery applications. *Advanced Drug Delivery Reviews* **60,** 1307–1315 (2008).
9. Zijlstra, P., Chon, J. W. & Gu, M. Five-dimensional optical recording mediated by surface plasmons in gold nanorods. *Nature* **459,** 410 (2009).
10. Catchpole, K., & Polman, A. Plasmonic solar cells. *Optics Express* **16,** 21793–21800 (2008).
11. Liu, Z., Hou, W., Pavaskar, P., Aykol, M. & Cronin, S. B. Plasmon resonant enhancement of photocatalytic water splitting under visible illumination. *Nano Letters* **11,** 1111–1116 (2011).
12. Kuznetsov, A. I., Miroshnichenko, A. E., Brongersma, M. L., Kivshar, Y. S. & Luk'yanchuk, B. Optically resonant dielectric nanostructures. *Science* **354** (2016).
13. Shelby, R. A., Smith, D. R. & Schultz, S. Experimental verification of a negative index of refraction. *Science* **292,** 77–79 (2001).
14. Pendry, J. B. Negative refraction makes a perfect lens. *Physical Review Letters* **85,** 3966 (2000).
15. Pendry, J. B., Schurig, D. & Smith, D. R. Controlling electromagnetic fields. *Science* **312,** 1780–1782 (2006).
16. Holloway, C. L. *et al.* An overview of the theory and applications of metasurfaces: The two-dimensional equivalents of metamaterials. *IEEE Antennas and Propagation Magazine* **54,** 10–35 (2012).
17. Yu, N. & Capasso, F. Flat optics with designer metasurfaces. *Nature Materials* **13,** 139–150 (2014).
18. Nichols, E. F. & Hull, G. F. A preliminary communication on the pressure of heat and light radiation. *Physical Review (Series I)* **13,** 307 (1901).
19. Ashkin, A. Acceleration and trapping of particles by radiation pressure. *Physical Review Letters* **24,** 156 (1970).
20. Ashkin, A., Dziedzic, J. M., Bjorkholm, J. & Chu, S. Observation of a single-beam gradient force optical trap for dielectric particles. *Optics Letters* **11,** 288–290 (1986).
21. Neuman, K. C. & Block, S. M. Optical trapping. *Review of Scientific Instruments* **75,** 2787–2809 (2004).
22. Jones, P. H., Maragò, O. M. & Volpe, G. *Optical tweezers: Principles and applications* (Cambridge University Press, 2015).
23. Svoboda, K., Schmidt, C. F., Schnapp, B. J. & Block, S. M. Direct observation of kinesin stepping by optical trapping interferometry. *Nature* **365,** 721 (1993).

24. Finer, J. T., Simmons, R. M. & Spudich, J. A. Single myosin molecule mechanics: piconewton forces and nanometre steps. *Nature* **368,** 113 (1994).
25. Abbondanzieri, E. A., Greenleaf, W. J., Shaevitz, J. W., Landick, R. & Block, S. M. Direct observation of base-pair stepping by RNA polymerase. *Nature* **438,** 460 (2005).
26. Chu, S., Bjorkholm, J., Ashkin, A & Cable, A. Experimental observation of optically trapped atoms. *Physical Review Letters* **57,** 314 (1986).
27. Raab, E., Prentiss, M, Cable, A., Chu, S. & Pritchard, D. E. Trapping of neutral sodium atoms with radiation pressure. *Physical Review Letters* **59,** 2631 (1987).
28. Svoboda, K. & Block, S. M. Optical trapping of metallic Rayleigh particles. *Optics Letters* **19,** 930–932 (1994).
29. Arias-González, J. R. & Nieto-Vesperinas, M. Optical forces on small particles: attractive and repulsive nature and plasmon-resonance conditions. *JOSA A* **20,** 1201–1209 (2003).
30. Hansen, P. M., Bhatia, V. K., Harrit, N. & Oddershede, L. B. Expanding the optical trapping range of gold nanoparticles. *Nano Letters* **5,** 1937–1942 (2005).
31. Selhuber-Unkel, C., Zins, I., Schubert, O., Sonnichsen, C. & Oddershede, L. B. Quantitative optical trapping of single gold nanorods. *Nano Letters* **8,** 2998–3003 (2008).
32. Toussaint, K. *et al.* Plasmon resonance-based optical trapping of single and multiple Au nanoparticles. *Optics Express* **15,** 12017–12029 (2007).
33. Bosanac, L., Aabo, T., Bendix, P. M. & Oddershede, L. B. Efficient optical trapping and visualization of silver nanoparticles. *Nano Letters* **8,** 1486–1491 (2008).
34. Ruijgrok, P., Verhart, N., Zijlstra, P, Tchebotareva, A. & Orrit, M. Brownian fluctuations and heating of an optically aligned gold nanorod. *Physical Review Letters* **107,** 037401 (2011).
35. Kyrsting, A., Bendix, P. M., Stamou, D. G. & Oddershede, L. B. Heat profiling of three-dimensionally optically trapped gold nanoparticles using vesicle cargo release. *Nano Letters* **11,** 888–892 (2010).
36. Andres-Arroyo, A., Wang, F., Toe, W. J. & Reece, P. Intrinsic heating in optically trapped Au nanoparticles measured by dark-field spectroscopy. *Biomedical Optics Express* **6,** 3646–3654 (2015).
37. Šiler, M., Ježek, J., Jákl, P., Pilát, Z. & Zemánek, P. Direct measurement of the temperature profile close to an optically trapped absorbing particle. *Optics Letters* **41,** 870–873 (2016).
38. Fedoruk, M., Meixner, M., Carretero-Palacios, S., Lohmüller, T. & Feldmann, J. Nanolithography by plasmonic heating and optical manipulation of gold nanoparticles. *ACS Nano* **7,** 7648–7653 (2013).
39. Bendix, P. M., Reihani, S. N. S. & Oddershede, L. B. Direct measurements of heating by electromagnetically trapped gold nanoparticles on supported lipid bilayers. *ACS Nano* **4,** 2256–2262 (2010).
40. Osinkina, L. *et al.* Tuning DNA binding kinetics in an optical trap by plasmonic nanoparticle heating. *Nano Letters* **13,** 3140–3144 (2013).
41. Ni, W., Ba, H., Lutich, A. A., Jäckel, F. & Feldmann, J. Enhancing single-nanoparticle surface-chemistry by plasmonic overheating in an optical trap. *Nano Letters* **12,** 4647–4650 (2012).
42. Beth, R. A. Mechanical detection and measurement of the angular momentum of light. *Physical Review* **50,** 115 (1936).
43. Friese, M., Nieminen, T., Heckenberg, N. & Rubinsztein-Dunlop, H. Optical alignment and spinning of laser-trapped microscopic particles. *Nature* **394,** 348 (1998).
44. Paterson, L *et al.* Controlled rotation of optically trapped microscopic particles. *Science* **292,** 912–914 (2001).
45. La Porta, A. & Wang, M. D. Optical torque wrench: angular trapping, rotation, and torque detection of quartz microparticles. *Physical Review Letters* **92,** 190801 (2004).
46. Tong, L., Miljkovic, V. D. & Käll, M. Alignment, rotation, and spinning of single plasmonic nanoparticles and nanowires using polarization dependent optical forces. *Nano Letters* **10,** 268–273 (2009).

47. Pelton, M. *et al.* Optical trapping and alignment of single gold nanorods by using plasmon resonances. *Optics Letters* **31,** 2075–2077 (2006).
48. Dienerowitz, M., Mazilu, M., Reece, P. J., Krauss, T. F. & Dholakia, K. Optical vortex trap for resonant confinement of metal nanoparticles. *Optics Express* **16,** 4991–4999 (2008).
49. Yan, Z. *et al.* Guiding spatial arrangements of silver nanoparticles by optical binding interactions in shaped light fields. *ACS Nano* **7,** 1790–1802 (2013).
50. Figliozzi, P. *et al.* Driven optical matter: Dynamics of electrodynamically coupled nanoparticles in an optical ring vortex. *Physical Review E* **95,** 022604 (2017).
51. Urban, A. S., Lutich, A. A., Stefani, F. D. & Feldmann, J. Laser printing single gold nanoparticles. *Nano Letters* **10,** 4794–4798 (2010).
52. Shao, L. & Käll, M. Light-driven rotation of plasmonic nanomotors. *Advanced Functional Materials* **28,** 1706272 (2018).
53. Shao, L., Yang, Z.-J., Andrén, D., Johansson, P. & Käll, M. Gold nanorod rotary motors driven by resonant light scattering. *ACS Nano* **9,** 12542–12551 (2015).
54. Tkachenko, G. *et al.* Optical trapping with planar silicon metalenses. *Optics Letters* **43,** 3224–3227 (2018).
55. Markovich, H., Shishkin, I. I., Hendler, N. & Ginzburg, P. Optical manipulation along an optical axis with a polarization sensitive meta-lens. *Nano Letters* **18,** 5024–5029 (2018).
56. Ma, Y., Rui, G., Gu, B. & Cui, Y. Trapping and manipulation of nanoparticles using multifocal optical vortex metalens. *Scientific Reports* **7,** 1–9 (2017).
57. Chantakit, T. *et al.* All-dielectric silicon metalens for two-dimensional particle manipulation in optical tweezers. *Photonics Research* **8,** 1435–1440 (2020).
58. Teyssier, J., Saenko, S. V., Van Der Marel, D. & Milinkovitch, M. C. Photonic crystals cause active colour change in chameleons. *Nature Communications* **6,** 1–7 (2015).
59. Sato, O., Kubo, S. & Gu, Z.-Z. Structural color films with lotus effects, superhydrophilicity, and tunable stop-bands. *Accounts of Chemical Research* **42,** 1–10 (2009).
60. Kinoshita, S. & Yoshioka, S. Structural colors in nature: the role of regularity and irregularity in the structure. *ChemPhysChem* **6,** 1442–1459 (2005).
61. Bohren, C. F. & Huffman, D. R. *Absorption and scattering of light by small particles* (John Wiley & Sons, 2008).
62. Yang, H. U. *et al.* Optical dielectric function of silver. *Physical Review B* **91,** 235137 (2015).
63. Gall, D. Electron mean free path in elemental metals. *Journal of Applied Physics* **119,** 085101 (2016).
64. Johnson, P. B. & Christy, R.-W. Optical constants of the noble metals. *Physical Review B* **6,** 4370 (1972).
65. Sehmi, H. S., Langbein, W. & Muljarov, E. A. *Optimizing the Drude-Lorentz model for material permittivity: Examples for semiconductors* in *2017 Progress In Electromagnetics Research Symposium-Spring (PIERS)* (2017), 994–1000.
66. Palik, E. D. *Handbook of optical constants of solids* (Academic Press, 1998).
67. Myroshnychenko, V. *et al.* Modelling the optical response of gold nanoparticles. *Chemical Society Reviews* **37,** 1792–1805 (2008).
68. Mie, G. Beiträge zur Optik trüber Medien, speziell kolloidaler Metallösungen. *Annalen der Physik* **330,** 377–445 (1908).
69. Meier, M & Wokaun, A. Enhanced fields on large metal particles: dynamic depolarization. *Optics Letters* **8,** 581–583 (1983).
70. Zeman, E. J. & Schatz, G. C. An accurate electromagnetic theory study of surface enhancement factors for silver, gold, copper, lithium, sodium, aluminum, gallium, indium, zinc, and cadmium. *Journal of Physical Chemistry* **91,** 634–643 (1987).
71. Bon, P., Maucort, G., Wattellier, B. & Monneret, S. Quadriwave lateral shearing interferometry for quantitative phase microscopy of living cells. *Optics Express* **17,** 13080–13094 (2009).
72. Baffou, G. *et al.* Thermal imaging of nanostructures by quantitative optical phase analysis. *ACS Nano* **6,** 2452–2458 (2012).

73. Khadir, S. *et al.* Optical imaging and characterization of graphene and other 2D materials using quantitative phase microscopy. *ACS Photonics* **4,** 3130–3139 (2017).
74. Khadir, S. *et al.* Full optical characterization of single nanoparticles using quantitative phase imaging. *Optica* **7,** 243–248 (2020).
75. Barnes, W. L., Dereux, A. & Ebbesen, T. W. Surface plasmon subwavelength optics. *Nature* **424,** 824 (2003).
76. Homola, J., Yee, S. S. & Gauglitz, G. Surface plasmon resonance sensors. *Sensors and Actuators B: Chemical* **54,** 3–15 (1999).
77. Chen, H., Shao, L., Li, Q. & Wang, J. Gold nanorods and their plasmonic properties. *Chemical Society Reviews* **42,** 2679–2724 (2013).
78. Willets, K. A. & Van Duyne, R. P. Localized surface plasmon resonance spectroscopy and sensing. *Annu. Rev. Phys. Chem.* **58,** 267–297 (2007).
79. Schuller, J. A. *et al.* Plasmonics for extreme light concentration and manipulation. *Nature Materials* **9,** 193 (2010).
80. Amendola, V., Pilot, R., Frasconi, M., Maragò, O. M. & Iatì, M. A. Surface plasmon resonance in gold nanoparticles: a review. *Journal of Physics: Condensed Matter* **29,** 203002 (2017).
81. Jiang, N., Zhuo, X. & Wang, J. Active plasmonics: principles, structures, and applications. *Chemical Reviews* **118,** 3054–3099 (2017).
82. Stockman, M. I. *et al.* Roadmap on plasmonics. *Journal of Optics* **20,** 043001 (2018).
83. Brongersma, M. L., Halas, N. J. & Nordlander, P. Plasmon-induced hot carrier science and technology. *Nature Nanotechnology* **10,** 25–34 (2015).
84. Jahani, S. & Jacob, Z. All-dielectric metamaterials. *Nature Nanotechnology* **11,** 23–36 (2016).
85. Baranov, D. G. *et al.* All-dielectric nanophotonics: the quest for better materials and fabrication techniques. *Optica* **4,** 814–825 (2017).
86. García-Etxarri, A. *et al.* Strong magnetic response of submicron silicon particles in the infrared. *Optics Express* **19,** 4815–4826 (2011).
87. Enkrich, C *et al.* Magnetic metamaterials at telecommunication and visible frequencies. *Physical Review Letters* **95,** 203901 (2005).
88. Pakizeh, T., Abrishamian, M., Granpayeh, N, Dmitriev, A. & Käll, M. Magnetic-field enhancement in gold nanosandwiches. *Optics Express* **14,** 8240–8246 (2006).
89. Kruk, S. & Kivshar, Y. Functional meta-optics and nanophotonics governed by Mie resonances. *ACS Photonics* **4,** 2638–2649 (2017).
90. Kuznetsov, A. I., Miroshnichenko, A. E., Fu, Y. H., Zhang, J. & Luk'yanchuk, B. Magnetic light. *Scientific Reports* **2,** 492 (2012).
91. Saviot, L. *Javascript Mie scattering calculator* Accessed: 2020-12-11. `https://saviot.cnrs.fr/mie/index.en.html`.
92. Kerker, M., Wang, D.-S. & Giles, C. Electromagnetic scattering by magnetic spheres. *JOSA* **73,** 765–767 (1983).
93. Fu, Y. H., Kuznetsov, A. I., Miroshnichenko, A. E., Yu, Y. F. & Luk'yanchuk, B. Directional visible light scattering by silicon nanoparticles. *Nature Communications* **4,** 1–6 (2013).
94. Staude, I. *et al.* Tailoring directional scattering through magnetic and electric resonances in subwavelength silicon nanodisks. *ACS Nano* **7,** 7824–7832 (2013).
95. Luk'yanchuk, B. S., Voshchinnikov, N. V., Paniagua-Domínguez, R. & Kuznetsov, A. I. Optimum forward light scattering by spherical and spheroidal dielectric nanoparticles with high refractive index. *ACS Photonics* **2,** 993–999 (2015).
96. Baffou, G. *Thermoplasmonics: Heating metal nanoparticles using light* (Cambridge University Press, 2017).
97. Baffou, G. & Quidant, R. Thermo-plasmonics: using metallic nanostructures as nano-sources of heat. *Laser & Photonics Reviews* **7,** 171–187 (2013).
98. Baffou, G., Cichos, F. & Quidant, R. Applications and challenges of thermoplasmonics. *Nature Materials* **19,** 946–958 (2020).
99. Neumann, O. *et al.* Solar vapor generation enabled by nanoparticles. *ACS Nano* **7,** 42–49 (2012).

100. Baffou, G., Polleux, J., Rigneault, H. & Monneret, S. Super-heating and micro-bubble generation around plasmonic nanoparticles under cw illumination. *The Journal of Physical Chemistry C* **118,** 4890–4898 (2014).
101. Fang, Z. *et al.* Evolution of light-induced vapor generation at a liquid-immersed metallic nanoparticle. *Nano Letters* **13,** 1736–1742 (2013).
102. Hou, L., Yorulmaz, M., Verhart, N. R. & Orrit, M. Explosive formation and dynamics of vapor nanobubbles around a continuously heated gold nanosphere. *New Journal of Physics* **17,** 013050 (2015).
103. Jones, S. C. *Mass Transport via Thermoplasmonics* PhD thesis (Chalmers University of Technology, Dec. 2020).
104. Boyer, D., Tamarat, P., Maali, A., Lounis, B. & Orrit, M. Photothermal imaging of nanometer-sized metal particles among scatterers. *Science* **297,** 1160–1163 (2002).
105. Huang, X., El-Sayed, I. H., Qian, W. & El-Sayed, M. A. Cancer cell imaging and photothermal therapy in the near-infrared region by using gold nanorods. *Journal of the American Chemical Society* **128,** 2115–2120 (2006).
106. Kryder, M. H. *et al.* Heat assisted magnetic recording. *Proceedings of the IEEE* **96,** 1810–1835 (2008).
107. Li, M., Lohmüller, T. & Feldmann, J. Optical injection of gold nanoparticles into living cells. *Nano Letters* **15,** 770–775 (2014).
108. Šípová, H., Shao, L., Odebo Länk, N., Andrén, D. & Käll, M. Photothermal DNA release from laser-tweezed individual gold nanomotors driven by photon angular momentum. *ACS Photonics* (2018).
109. Jones, S., Andrén, D., Karpinski, P. & Käll, M. Photothermal heating of plasmonic nanoantennas: Influence on trapped particle dynamics and colloid distribution. *ACS Photonics* **5,** 2878–2887 (2018).
110. Iijima, S. & Ichihashi, T. Structural instability of ultrafine particles of metals. *Physical Review Letters* **56,** 616 (1986).
111. Taylor, A. B., Siddiquee, A. M. & Chon, J. W. Below melting point photothermal reshaping of single gold nanorods driven by surface diffusion. *ACS Nano* **8,** 12071–12079 (2014).
112. Zijlstra, P., Chon, J. W. & Gu, M. White light scattering spectroscopy and electron microscopy of laser induced melting in single gold nanorods. *Physical Chemistry Chemical Physics* **11,** 5915–5921 (2009).
113. Link, S., Burda, C., Nikoobakht, B & El-Sayed, M. A. Laser-induced shape changes of colloidal gold nanorods using femtosecond and nanosecond laser pulses. *The Journal of Physical Chemistry B* **104,** 6152–6163 (2000).
114. Habenicht, A., Olapinski, M., Burmeister, F., Leiderer, P. & Boneberg, J. Jumping nanodroplets. *Science* **309,** 2043–2045 (2005).
115. Gordel, M. *et al.* Post-synthesis reshaping of gold nanorods using a femtosecond laser. *Physical Chemistry Chemical Physics* **16,** 71–78 (2014).
116. González-Rubio, G. *et al.* Femtosecond laser reshaping yields gold nanorods with ultranarrow surface plasmon resonances. *Science* **358,** 640–644 (2017).
117. Takahashi, H., Niidome, T., Nariai, A., Niidome, Y. & Yamada, S. Photothermal reshaping of gold nanorods prevents further cell death. *Nanotechnology* **17,** 4431 (2006).
118. Wang, J. *et al.* Photothermal reshaping of gold nanoparticles in a plasmonic absorber. *Optics Express* **19,** 14726–14734 (2011).
119. Petrova, H. *et al.* On the temperature stability of gold nanorods: comparison between thermal and ultrafast laser-induced heating. *Physical Chemistry Chemical Physics* **8,** 814–821 (2006).
120. Mohamed, M. B., Ismail, K. Z., Link, S. & El-Sayed, M. A. Thermal reshaping of gold nanorods in micelles. *The Journal of Physical Chemistry B* **102,** 9370–9374 (1998).
121. Liu, Y., Mills, E. N. & Composto, R. J. Tuning optical properties of gold nanorods in polymer films through thermal reshaping. *Journal of Materials Chemistry* **19,** 2704–2709 (2009).
122. Makarov, S. V. *et al.* Light-induced tuning and reconfiguration of nanophotonic structures. *Laser & Photonics Reviews* **11,** 1700108 (2017).

123. Babynina, A. *et al.* Bending gold nanorods with light. *Nano Letters* **16,** 6485–6490 (2016).
124. Violi, I. L., Gargiulo, J., Von Bilderling, C., Cortés, E. & Stefani, F. D. Light-induced polarization-directed growth of optically printed gold nanoparticles. *Nano Letters* **16,** 6529–6533 (2016).
125. Wang, S. & Ding, T. Photothermal-assisted optical stretching of gold nanoparticles. *ACS Nano* **13,** 32–37 (2018).
126. Setoura, K., Okada, Y. & Hashimoto, S. CW-laser-induced morphological changes of a single gold nanoparticle on glass: observation of surface evaporation. *Physical Chemistry Chemical Physics* **16,** 26938–26945 (2014).
127. Ebbesen, T. W., Lezec, H. J., Ghaemi, H., Thio, T. & Wolff, P. A. Extraordinary optical transmission through sub-wavelength hole arrays. *Nature* **391,** 667–669 (1998).
128. Engheta, N. & Ziolkowski, R. W. *Metamaterials: physics and engineering explorations* (John Wiley & Sons, 2006).
129. Smith, D. R., Padilla, W. J., Vier, D., Nemat-Nasser, S. C. & Schultz, S. Composite medium with simultaneously negative permeability and permittivity. *Physical Review Letters* **84,** 4184 (2000).
130. Shalaev, V. M. *et al.* Negative index of refraction in optical metamaterials. *Optics Letters* **30,** 3356–3358 (2005).
131. Landy, N. I., Sajuyigbe, S, Mock, J. J., Smith, D. R. & Padilla, W. J. Perfect metamaterial absorber. *Physical Review Letters* **100,** 207402 (2008).
132. Soukoulis, C. M. & Wegener, M. Past achievements and future challenges in the development of three-dimensional photonic metamaterials. *Nature Photonics* **5,** 523–530 (2011).
133. Chen, H.-T., Taylor, A. J. & Yu, N. A review of metasurfaces: physics and applications. *Reports on Progress in Physics* **79,** 076401 (2016).
134. Glybovski, S. B., Tretyakov, S. A., Belov, P. A., Kivshar, Y. S. & Simovski, C. R. Metasurfaces: From microwaves to visible. *Physics Reports* **634,** 1–72 (2016).
135. Aieta, F. *et al.* Aberration-free ultrathin flat lenses and axicons at telecom wavelengths based on plasmonic metasurfaces. *Nano Letters* **12,** 4932–4936 (2012).
136. Yu, N. *et al.* Flat optics: controlling wavefronts with optical antenna metasurfaces. *IEEE Journal of Selected Topics in Quantum Electronics* **19,** 4700423–4700423 (2013).
137. Levy, M. *Fresnel Lens* Accessed 2020-03-24. `https://academic.eb.com/levels/collegiate/article/Fresnel-lens/35385` (Encyclopædia Britannica).
138. Soskind, Y. *Field guide to diffractive optics* (SPIE, 2011).
139. Faklis, D. & Morris, G. M. Spectral properties of multiorder diffractive lenses. *Applied Optics* **34,** 2462–2468 (1995).
140. Gerchberg, R. W. A practical algorithm for the determination of phase from image and diffraction plane pictures. *Optik* **35,** 237–246 (1972).
141. Yu, N. *et al.* Light propagation with phase discontinuities: generalized laws of reflection and refraction. *Science* **334,** 333–337 (2011).
142. Otón, J., Millán, M. S., Pérez-Cabré, E. & García-Martínez, P. *Imaging characteristics of programmable lenses generated by SLM* in *AIP Conference Proceedings* **860** (2006), 471–480.
143. Khorasaninejad, M. & Capasso, F. Metalenses: Versatile multifunctional photonic components. *Science* **358,** eaam8100 (2017).
144. Ni, X., Emani, N. K., Kildishev, A. V., Boltasseva, A. & Shalaev, V. M. Broadband light bending with plasmonic nanoantennas. *Science* **335,** 427–427 (2012).
145. Yu, N. *et al.* A broadband, background-free quarter-wave plate based on plasmonic metasurfaces. *Nano Letters* **12,** 6328–6333 (2012).
146. Sun, S. *et al.* High-efficiency broadband anomalous reflection by gradient meta-surfaces. *Nano Letters* **12,** 6223–6229 (2012).
147. Pors, A. & Bozhevolnyi, S. I. Plasmonic metasurfaces for efficient phase control in reflection. *Optics Express* **21,** 27438–27451 (2013).
148. Arbabi, A. & Faraon, A. Fundamental limits of ultrathin metasurfaces. *Scientific Reports* **7,** 43722 (2017).

149. Zhang, J. *et al.* Plasmonic metasurfaces with 42.3% transmission efficiency in the visible. *Light: Science & Applications* **8,** 1–13 (2019).
150. Hanmeng, L., Fang, B., Chen, C., Shining, Z. & Li, T. Cavity-enhanced metallic metalens with improved Efficiency. *Scientific Reports* **10** (2020).
151. Genevet, P., Capasso, F., Aieta, F., Khorasaninejad, M. & Devlin, R. Recent advances in planar optics: from plasmonic to dielectric metasurfaces. *Optica* **4,** 139–152 (2017).
152. Lin, D., Fan, P., Hasman, E. & Brongersma, M. L. Dielectric gradient metasurface optical elements. *Science* **345,** 298–302 (2014).
153. Aieta, F., Kats, M. A., Genevet, P. & Capasso, F. Multiwavelength achromatic metasurfaces by dispersive phase compensation. *Science* **347,** 1342–1345 (2015).
154. Yu, Y. F. *et al.* High-transmission dielectric metasurface with 2π phase control at visible wavelengths. *Laser & Photonics Reviews* **9,** 412–418 (2015).
155. Khorasaninejad, M. *et al.* Metalenses at visible wavelengths: Diffraction-limited focusing and subwavelength resolution imaging. *Science* **352,** 1190–1194 (2016).
156. Liang, H. *et al.* Ultrahigh numerical aperture metalens at visible wavelengths. *Nano Letters* **18,** 4460–4466 (2018).
157. Chen, W. T. *et al.* Immersion meta-lenses at visible wavelengths for nanoscale imaging. *Nano Letters* **17,** 3188–3194 (2017).
158. Wang, S. *et al.* A broadband achromatic metalens in the visible. *Nature Nanotechnology* **13,** 227–232 (2018).
159. Ding, F., Pors, A. & Bozhevolnyi, S. I. Gradient metasurfaces: a review of fundamentals and applications. *Reports on Progress in Physics* **81,** 026401 (2017).
160. Kamali, S. M., Arbabi, E., Arbabi, A. & Faraon, A. A review of dielectric optical metasurfaces for wavefront control. *Nanophotonics* **7,** 1041–1068 (2018).
161. Chen, W. T., Zhu, A. Y. & Capasso, F. Flat optics with dispersion-engineered metasurfaces. *Nature Reviews Materials* **5,** 604–620 (2020).
162. Mittra, R., Chan, C. H. & Cwik, T. Techniques for analyzing frequency selective surfaces – a review. *Proceedings of the IEEE* **76,** 1593–1615 (1988).
163. Pozar, D. Flat lens antenna concept using aperture coupled microstrip patches. *Electronics Letters* **32,** 2109–2111 (1996).
164. Pozar, D. M., Targonski, S. D. & Syrigos, H. Design of millimeter wave microstrip reflectarrays. *IEEE Transactions on Antennas and Propagation* **45,** 287–296 (1997).
165. Swanson, G. J. *Binary optics technology: the theory and design of multi-level diffractive optical elements* tech. rep. (MIT – Lexington Lincoln Lab, 1989).
166. Gale, M. T. Replication techniques for diffractive optical elements. *Microelectronic Engineering* **34,** 321–339 (1997).
167. Lalanne, P. & Chavel, P. Metalenses at visible wavelengths: past, present, perspectives. *Laser & Photonics Reviews* **11,** 1600295 (2017).
168. Fattal, D., Li, J., Peng, Z., Fiorentino, M. & Beausoleil, R. G. Flat dielectric grating reflectors with focusing abilities. *Nature Photonics* **4,** 466–470 (2010).
169. Huang, M. C., Zhou, Y & Chang-Hasnain, C. J. A surface-emitting laser incorporating a high-index-contrast subwavelength grating. *Nature Photonics* **1,** 119–122 (2007).
170. Stork, W., Streibl, N., Haidner, H & Kipfer, P. Artificial distributed-index media fabricated by zero-order gratings. *Optics Letters* **16,** 1921–1923 (1991).
171. Lalanne, P. Waveguiding in blazed-binary diffractive elements. *JOSA A* **16,** 2517–2520 (1999).
172. Lalanne, P., Astilean, S., Chavel, P., Cambril, E. & Launois, H. Blazed binary subwavelength gratings with efficiencies larger than those of conventional échelette gratings. *Optics Letters* **23,** 1081–1083 (1998).
173. Lalanne, P., Astilean, S., Chavel, P., Cambril, E. & Launois, H. Design and fabrication of blazed binary diffractive elements with sampling periods smaller than the structural cutoff. *JOSA A* **16,** 1143–1156 (1999).
174. Lee, M.-S. L. *et al.* Imaging with blazed-binary diffractive elements. *Journal of Optics A: Pure and Applied Optics* **4,** S119 (2002).
175. Stepanova, M. & Dew, S. *Nanofabrication: techniques and principles* (Springer Science & Business Media, 2011).

176. Engelberg, J. & Levy, U. The advantages of metalenses over diffractive lenses. *Nature Communications* **11,** 1–4 (2020).
177. Banerji, S. *et al.* Imaging with flat optics: metalenses or diffractive lenses? *Optica* **6,** 805–810 (2019).
178. Reino, C. G., Pérez, M. & Bao, C. *Gradient-index optics: Fundamentals and applications* 2002.
179. Arbabi, A., Horie, Y., Bagheri, M. & Faraon, A. Dielectric metasurfaces for complete control of phase and polarization with subwavelength spatial resolution and high transmission. *Nature Nanotechnology* **10,** 937–943 (2015).
180. Arbabi, A., Horie, Y., Ball, A. J., Bagheri, M. & Faraon, A. Subwavelength-thick lenses with high numerical apertures and large efficiency based on high-contrast transmitarrays. *Nature Communications* **6,** 1–6 (2015).
181. Zhan, A. *et al.* Low-contrast dielectric metasurface optics. *ACS Photonics* **3,** 209–214 (2016).
182. Khorasaninejad, M. *et al.* Polarization-insensitive metalenses at visible wavelengths. *Nano Letters* **16,** 7229–7234 (2016).
183. Lin, R. J. *et al.* Achromatic metalens array for full-colour light-field imaging. *Nature Nanotechnology* **14,** 227–231 (2019).
184. Pancharatnam, S. *Generalized theory of interference and its applications* in *Proceedings of the Indian Academy of Sciences-Section A* **44** (1956), 398–417.
185. Berry, M. V. Quantal phase factors accompanying adiabatic changes. *Proceedings of the Royal Society of London. A. Mathematical and Physical Sciences* **392,** 45–57 (1984).
186. Bomzon, Z., Biener, G., Kleiner, V. & Hasman, E. Space-variant Pancharatnam–Berry phase optical elements with computer-generated subwavelength gratings. *Optics Letters* **27,** 1141–1143 (2002).
187. Hasman, E., Bomzon, Z., Niv, A., Biener, G. & Kleiner, V. Polarization beam-splitters and optical switches based on space-variant computer-generated subwavelength quasi-periodic structures. *Optics Communications* **209,** 45–54 (2002).
188. Biener, G., Niv, A., Kleiner, V. & Hasman, E. Formation of helical beams by use of Pancharatnam–Berry phase optical elements. *Optics Letters* **27,** 1875–1877 (2002).
189. Hasman, E., Kleiner, V., Biener, G. & Niv, A. Polarization dependent focusing lens by use of quantized Pancharatnam–Berry phase diffractive optics. *Applied Physics Letters* **82,** 328–330 (2003).
190. Bomzon, Z., Biener, G., Kleiner, V. & Hasman, E. Radially and azimuthally polarized beams generated by space-variant dielectric subwavelength gratings. *Optics Letters* **27,** 285–287 (2002).
191. Chen, X. *et al.* Dual-polarity plasmonic metalens for visible light. *Nature Communications* **3,** 1–6 (2012).
192. Karimi, E. *et al.* Generating optical orbital angular momentum at visible wavelengths using a plasmonic metasurface. *Light: Science & Applications* **3,** e167–e167 (2014).
193. Zheng, G. *et al.* Metasurface holograms reaching 80% efficiency. *Nature Nanotechnology* **10,** 308–312 (2015).
194. Khorasaninejad, M. & Crozier, K. B. Silicon nanofin grating as a miniature chirality-distinguishing beam-splitter. *Nature Communications* **5,** 1–6 (2014).
195. Maguid, E. *et al.* Multifunctional interleaved geometric-phase dielectric metasurfaces. *Light: Science & Applications* **6,** e17027–e17027 (2017).
196. Khadir, S. *et al.* Metasurface optical characterization using quadriwave lateral shearing interferometry. *ACS Photonics* **8,** 603–613 (2020).
197. Martínez-Llinàs, J. *et al.* A Gaussian reflective metasurface for advanced wavefront manipulation. *Optics Express* **27,** 21069–21082 (2019).
198. Marrucci, L., Manzo, C & Paparo, D. Pancharatnam–Berry phase optical elements for wave front shaping in the visible domain: switchable helical mode generation. *Applied Physics Letters* **88,** 221102 (2006).
199. Oh, C. & Escuti, M. J. Achromatic diffraction from polarization gratings with high efficiency. *Optics Letters* **33,** 2287–2289 (2008).

200. Lee, Y.-H. *et al.* Recent progress in Pancharatnam–Berry phase optical elements and the applications for virtual/augmented realities. *Optical Data Processing and Storage* **3,** 79–88 (2017).
201. Yu, H., Zhou, Z., Qi, Y., Zhang, X. & Wei, Q.-H. Pancharatnam–Berry optical lenses. *JOSA B* **36,** D107–D111 (2019).
202. Zhan, T., Xiong, J., Lee, Y.-H. & Wu, S.-T. Polarization-independent Pancharatnam–Berry phase lens system. *Optics Express* **26,** 35026–35033 (2018).
203. Decker, M. *et al.* High-efficiency dielectric Huygens' surfaces. *Advanced Optical Materials* **3,** 813–820 (2015).
204. Shalaev, M. I. *et al.* High-efficiency all-dielectric metasurfaces for ultracompact beam manipulation in transmission mode. *Nano Letters* **15,** 6261–6266 (2015).
205. Kruk, S. *et al.* Invited article: Broadband highly efficient dielectric metadevices for polarization control. *APL Photonics* **1,** 030801 (2016).
206. Ollanik, A. J., Smith, J. A., Belue, M. J. & Escarra, M. D. High-efficiency all-dielectric Huygens metasurfaces from the ultraviolet to the infrared. *ACS Photonics* **5,** 1351–1358 (2018).
207. Paniagua-Dominguez, R. *et al.* A metalens with a near-unity numerical aperture. *Nano Letters* **18,** 2124–2132 (2018).
208. Khaidarov, E. *et al.* Asymmetric nanoantennas for ultrahigh angle broadband visible light bending. *Nano Letters* **17,** 6267–6272 (2017).
209. Shibanuma, T. *et al.* Experimental demonstration of tunable directional scattering of visible light from all-dielectric asymmetric dimers. *ACS Photonics* **4,** 489–494 (2017).
210. She, A., Zhang, S., Shian, S., Clarke, D. R. & Capasso, F. Large area metalenses: design, characterization, and mass manufacturing. *Optics Express* **26,** 1573–1585 (2018).
211. Xu, Z. *et al.* CMOS-compatible all-Si metasurface polarizing bandpass filters on 12-inch wafers. *Optics Express* **27,** 26060–26069 (2019).
212. Park, J.-S. *et al.* All-glass, large metalens at visible wavelength using deep-ultraviolet projection lithography. *Nano Letters* **19,** 8673–8682 (2019).
213. Li, N. *et al.* Large-area metasurface on CMOS-compatible fabrication platform: driving flat optics from lab to fab. *Nanophotonics* **1** (2020).
214. Brière, G. *et al.* An etching-free approach toward large-scale light-emitting metasurfaces. *Advanced Optical Materials* **7,** 1801271 (2019).
215. Dirdal, C. A. *et al.* Towards high-throughput large-area metalens fabrication using UV-nanoimprint lithography and Bosch deep reactive ion etching. *Optics Express* **28,** 15542–15561 (2020).
216. Khorasaninejad, M. *et al.* Achromatic metasurface lens at telecommunication wavelengths. *Nano Letters* **15,** 5358–5362 (2015).
217. Shrestha, S., Overvig, A. C., Lu, M., Stein, A. & Yu, N. Broadband achromatic dielectric metalenses. *Light: Science & Applications* **7,** 1–11 (2018).
218. Chen, W. T. *et al.* A broadband achromatic metalens for focusing and imaging in the visible. *Nature Nanotechnology* **13,** 220–226 (2018).
219. Avayu, O., Almeida, E., Prior, Y. & Ellenbogen, T. Composite functional metasurfaces for multispectral achromatic optics. *Nature Communications* **8,** 1–7 (2017).
220. Li, M. *et al.* Dual-layer achromatic metalens design with an effective Abbe number. *Optics Express* **28,** 26041–26055 (2020).
221. Chen, W. T. *et al.* Broadband achromatic metasurface-refractive optics. *Nano Letters* **18,** 7801–7808 (2018).
222. Sawant, R. *et al.* Mitigating chromatic dispersion with hybrid optical metasurfaces. *Advanced Materials* **31,** 1805555 (2019).
223. Zou, X. *et al.* Imaging based on metalenses. *PhotoniX* **1,** 1–24 (2020).
224. Gao, H. *et al.* Dynamic 3D meta-holography in visible range with large frame number and high frame rate. *Science Advances* **6,** eaba8595 (2020).
225. Ee, H.-S. & Agarwal, R. Tunable metasurface and flat optical zoom lens on a stretchable substrate. *Nano Letters* **16,** 2818–2823 (2016).
226. Malek, S. C., Ee, H.-S. & Agarwal, R. Strain multiplexed metasurface holograms on a stretchable substrate. *Nano Letters* **17,** 3641–3645 (2017).

227. Li, S.-Q. *et al.* Phase-only transmissive spatial light modulator based on tunable dielectric metasurface. *Science* **364,** 1087–1090 (2019).
228. Chung, H. & Miller, O. D. Tunable metasurface inverse design for 80% switching efficiencies and 144° angular deflection. *ACS Photonics* **7,** 2236–2243 (2020).
229. Lee, S.-Y. *et al.* Holographic image generation with a thin-film resonance caused by chalcogenide phase-change material. *Scientific Reports* **7,** 1–8 (2017).
230. Iyer, P. P., DeCrescent, R. A., Lewi, T., Antonellis, N. & Schuller, J. A. Uniform thermo-optic tunability of dielectric metalenses. *Physical Review Applied* **10,** 044029 (2018).
231. Li, J. *et al.* Addressable metasurfaces for dynamic holography and optical information encryption. *Science Advances* **4,** eaar6768 (2018).
232. Afridi, A. *et al.* Electrically driven varifocal silicon metalens. *ACS Photonics* **5,** 4497–4503 (2018).
233. Berto, P. *et al.* Tunable and free-form planar optics. *Nature Photonics* **13,** 649–656 (2019).
234. Edrei, E. & Scarcelli, G. Optical focusing beyond the diffraction limit via vortex-assisted transient microlenses. *ACS Photonics* **7,** 914–918 (2020).
235. Moscatelli, A. *Tiny Lenses Will Enable Design of Miniature Optical Devices* Accessed: 2021-01-18. `https://www.scientificamerican.com/article/tiny-lenses-will-enable-design-of-miniature-optical-devices/` (Scientific American).
236. Xie, Y.-Y. *et al.* Metasurface-integrated vertical cavity surface-emitting lasers for programmable directional lasing emissions. *Nature Nanotechnology* **15,** 125–130 (2020).
237. Li, L. *et al.* Metalens-array–based high-dimensional and multiphoton quantum source. *Science* **368,** 1487–1490 (2020).
238. Pahlevaninezhad, H. *et al.* Nano-optic endoscope for high-resolution optical coherence tomography in vivo. *Nature Photonics* **12,** 540–547 (2018).
239. Kwon, H., Arbabi, E., Kamali, S. M., Faraji-Dana, M. & Faraon, A. Single-shot quantitative phase gradient microscopy using a system of multifunctional metasurfaces. *Nature Photonics* **14,** 109–114 (2020).
240. Arbabi, A. *et al.* Miniature optical planar camera based on a wide-angle metasurface doublet corrected for monochromatic aberrations. *Nature Communications* **7,** 1–9 (2016).
241. Lee, G.-Y. *et al.* Metasurface eyepiece for augmented reality. *Nature Communications* **9,** 1–10 (2018).
242. Song, W. *et al.* Large-scale Huygens metasurfaces for holographic 3D near-eye displays. *arXiv preprint arXiv:2010.04451* (2020).
243. Park, J. *et al.* All-solid-state spatial light modulator with independent phase and amplitude control for three-dimensional LiDAR applications. *Nature Nanotechnology,* 1–8 (2020).
244. Joo, W.-J. *et al.* Metasurface-driven OLED displays beyond 10,000 pixels per inch. *Science* **370,** 459–463 (2020).
245. Soon, W. L. *OSA incubator on flat optics: Recent advances and future opportunities* Accessed: 2020-11-25. `https://www.osa.org/en-us/the_optical_society_blog/2020/february_2020/osa_incubator_on_flat_optics_day_1_reflections/`.
246. Lehmuskero, A., Johansson, P., Rubinsztein-Dunlop, H., Tong, L. & Käll, M. Laser trapping of colloidal metal nanoparticles. *ACS Nano* **9,** 3453–3469 (2015).
247. Padgett, M. & Leach, J. in *Structured light and its applications: An introduction to phase-structured beams and nanoscale optical forces* (ed Andrews, D. L.) p.237–248 (Academic press, 2011).
248. Johnson, L. *et al.* NanoSail-D: A solar sail demonstration mission. *Acta astronautica* **68,** 571–575 (2011).
249. Parkin, K. L. The breakthrough starshot system model. *Acta Astronautica* **152,** 370–384 (2018).

250. Ullery, D. C. *et al.* Strong solar radiation forces from anomalously reflecting metasurfaces for solar sail attitude control. *Scientific Reports* **8,** 1–10 (2018).
251. Ilic, O. & Atwater, H. A. Self-stabilizing photonic levitation and propulsion of nanostructured macroscopic objects. *Nature Photonics* **13,** 289–295 (2019).
252. Yifat, Y. *et al.* Reactive optical matter: light-induced motility in electrodynamically asymmetric nanoscale scatterers. *Light: Science & Applications* **7,** 1–7 (2018).
253. Tanaka, Y. Y. *et al.* Plasmonic linear nanomotor using lateral optical forces. *Science Advances* **6,** eabc3726 (2020).
254. Roichman, Y., Sun, B., Roichman, Y., Amato-Grill, J. & Grier, D. G. Optical forces arising from phase gradients. *Physical Review Letters* **100,** 013602 (2008).
255. Swartzlander, G. A., Peterson, T. J., Artusio-Glimpse, A. B. & Raisanen, A. D. Stable optical lift. *Nature Photonics* **5,** 48–51 (2011).
256. Simpson, S. H., Hanna, S., Peterson, T. J. & Swartzlander, G. A. Optical lift from dielectric semicylinders. *Optics Letters* **37,** 4038–4040 (2012).
257. Artusio-Glimpse, A. B., Peterson, T. J. & Swartzlander, G. A. Refractive optical wing oscillators with one reflective surface. *Optics Letters* **38,** 935–937 (2013).
258. Búzás, A. *et al.* Light sailboats: Laser driven autonomous microrobots. *Applied Physics Letters* **101,** 041111 (2012).
259. Magallanes, H. & Brasselet, E. Macroscopic direct observation of optical spin-dependent lateral forces and left-handed torques. *Nature Photonics* **12,** 461–464 (2018).
260. Ashkin, A. & Gordon, J. P. Stability of radiation-pressure particle traps: an optical Earnshaw theorem. *Optics Letters* **8,** 511–513 (1983).
261. Barton, J. & Alexander, D. Fifth-order corrected electromagnetic field components for a fundamental Gaussian beam. *Journal of Applied Physics* **66,** 2800–2802 (1989).
262. Agayan, R. R., Gittes, F., Kopelman, R. & Schmidt, C. F. Optical trapping near resonance absorption. *Applied Optics* **41,** 2318–2327 (2002).
263. Urban, A. S. *et al.* Optical trapping and manipulation of plasmonic nanoparticles: fundamentals, applications, and perspectives. *Nanoscale* **6,** 4458–4474 (2014).
264. Länk, N. O., Johansson, P. & Käll, M. Optical tweezing and photothermal properties of resonant dielectric and metallic nanospheres. *ACS Photonics* **7,** 2405–2412 (2020).
265. Tauro, S., Bañas, A., Palima, D. & Glückstad, J. Dynamic axial stabilization of counter-propagating beam-traps with feedback control. *Optics Express* **18,** 18217–18222 (2010).
266. Schonbrun, E., Rinzler, C. & Crozier, K. B. Microfabricated water immersion zone plate optical tweezer. *Applied Physics Letters* **92,** 071112 (2008).
267. Davidson, N. & Bokor, N. High-numerical-aperture focusing of radially polarized doughnut beams with a parabolic mirror and a flat diffractive lens. *Optics Letters* **29,** 1318–1320 (2004).
268. Shen, Z. *et al.* Optical manipulation of Rayleigh particles by metalenses – a numerical study. *Applied Optics* **58,** 5794–5799 (2019).
269. Shen, Z., Wang, Z., Liu, H. & Shen, Y. Optical trapping and separation of metal nanoparticles by cylindrical metalenses with phase gradients. *IEEE Photonics Journal* **12,** 1–10 (2020).
270. Yin, S. *et al.* Coherently tunable metalens tweezers for optofluidic particle routing. *Optics Express* **28,** 38949–38959 (2020).
271. Ma, L. *et al.* Diffraction-limited axial double foci and optical traps generated by optimization-free planar lens. *Nanophotonics* **9,** 841–853 (2020).
272. He, H, Friese, M., Heckenberg, N. & Rubinsztein-Dunlop, H. Direct observation of transfer of angular momentum to absorptive particles from a laser beam with a phase singularity. *Physical Review Letters* **75,** 826 (1995).
273. Allen, L., Beijersbergen, M. W., Spreeuw, R. & Woerdman, J. Orbital angular momentum of light and the transformation of Laguerre-Gaussian laser modes. *Physical Review A* **45,** 8185 (1992).
274. Friese, M., Enger, J, Rubinsztein-Dunlop, H & Heckenberg, N. R. Optical angular-momentum transfer to trapped absorbing particles. *Physical Review A* **54,** 1593 (1996).

275. Leach, J., Mushfique, H., di Leonardo, R., Padgett, M. & Cooper, J. An optically driven pump for microfluidics. *Lab on a Chip* **6,** 735–739 (2006).
276. Lehmuskero, A., Ogier, R., Gschneidtner, T., Johansson, P. & Käll, M. Ultrafast spinning of gold nanoparticles in water using circularly polarized light. *Nano Letters* **13,** 3129–3134 (2013).
277. Simpson, N., Dholakia, K, Allen, L & Padgett, M. Mechanical equivalence of spin and orbital angular momentum of light: an optical spanner. *Optics Letters* **22,** 52–54 (1997).
278. Neale, S. L., MacDonald, M. P., Dholakia, K. & Krauss, T. F. All-optical control of microfluidic components using form birefringence. *Nature Materials* **4,** 530 (2005).
279. Higurashi, E, Ukita, H, Tanaka, H & Ohguchi, O. Optically induced rotation of anisotropic micro-objects fabricated by surface micromachining. *Applied Physics Letters* **64,** 2209–2210 (1994).
280. Galajda, P. & Ormos, P. Complex micromachines produced and driven by light. *Applied Physics Letters* **78,** 249–251 (2001).
281. Galajda, P. & Ormos, P. Rotors produced and driven in laser tweezers with reversed direction of rotation. *Applied Physics Letters* **80,** 4653–4655 (2002).
282. Lin, X.-F. *et al.* A light-driven turbine-like micro-rotor and study on its light-to-mechanical power conversion efficiency. *Applied Physics Letters* **101,** 113901 (2012).
283. Šíopov Jungová, H., Andrén, D., Jones, S. & Käll, M. Nanoscale inorganic motors driven by light: Principles, realizations, and opportunities. *Chemical Reviews* **120,** 269–287 (2019).
284. Lee, Y. E., Fung, K. H., Jin, D. & Fang, N. X. Optical torque from enhanced scattering by multipolar plasmonic resonance. *Nanophotonics* **3,** 343–350 (2014).
285. Kong, D., Lin, W., Pan, Y. & Zhang, K. Swimming motion of rod-shaped magnetotactic bacteria: the effects of shape and growing magnetic moment. *Frontiers in Microbiology* **5,** 8 (2014).
286. Bishop, A. I., Nieminen, T. A., Heckenberg, N. R. & Rubinsztein-Dunlop, H. Optical microrheology using rotating laser-trapped particles. *Physical Review Letters* **92,** 198104 (2004).
287. Favre-Bulle, I. A., Stilgoe, A. B., Rubinsztein-Dunlop, H. & Scott, E. K. Optical trapping of otoliths drives vestibular behaviours in larval zebrafish. *Nature Communications* **8,** 630 (2017).
288. Pedaci, F., Huang, Z., Van Oene, M., Barland, S. & Dekker, N. H. Excitable particles in an optical torque wrench. *Nature Physics* **7,** 259–264 (2011).
289. Xu, L., Mou, F., Gong, H., Luo, M. & Guan, J. Light-driven micro/nanomotors: from fundamentals to applications. *Chemical Society Reviews* **46,** 6905–6926 (2017).
290. Chen, H., Zhao, Q. & Du, X. Light-powered micro/nanomotors. *Micromachines* **9,** 41 (2018).
291. Jauffred, L., Taheri, S. M.-R., Schmitt, R., Linke, H. & Oddershede, L. B. Optical trapping of gold nanoparticles in air. *Nano Letters* **15,** 4713–4719 (2015).
292. Arita, Y., Mazilu, M. & Dholakia, K. Laser-induced rotation and cooling of a trapped microgyroscope in vacuum. *Nature Communications* **4,** 2374 (2013).
293. Ahn, J. *et al.* Ultrasensitive torque detection with an optically levitated nanorotor. *Nature Nanotechnology,* 1–5 (2020).
294. Lucretius, T. L. C. *On the Nature of Things* trans. by Leonard, W. E. (Project Gutenberg, 1997).
295. Einstein, A. Über die von der molekularkinetischen Theorie der Wärme geforderte Bewegung von in ruhenden Flüssigkeiten suspendierten Teilchen. *Annalen der Physik* **322,** 549–560 (1905).
296. Purcell, E. M. Life at low Reynolds number. *American Journal of Physics* **45,** 3–11 (1977).
297. Fogel'son, R. & Likhachev, E. Temperature dependence of viscosity. *Technical Physics* **46,** 1056–1059 (2001).
298. Volpe, G. & Volpe, G. Simulation of a Brownian particle in an optical trap. *American Journal of Physics* **81,** 224–230 (2013).

299. Mazaheri, M., Ehrig, J., Shkarin, A., Zaburdaev, V. & Sandoghdar, V. Ultrahigh-speed imaging of rotational diffusion on a lipid bilayer. *Nano Letters* **20,** 7213–7219 (2020).
300. Berg-Sørensen, K. & Flyvbjerg, H. Power spectrum analysis for optical tweezers. *Review of Scientific Instruments* **75,** 594–612 (2004).
301. Rings, D., Schachoff, R., Selmke, M., Cichos, F. & Kroy, K. Hot Brownian motion. *Physical Review Letters* **105,** 090604 (2010).
302. Falasco, G, Gnann, M., Rings, D & Kroy, K. Effective temperatures of hot Brownian motion. *Physical Review E* **90,** 032131 (2014).
303. Rings, D., Chakraborty, D. & Kroy, K. Rotational hot Brownian motion. *New Journal of Physics* **14,** 053012 (2012).
304. Arita, Y. *et al.* Rotational dynamics and heating of trapped nanovaterite particles. *ACS Nano* **10,** 11505–11510 (2016).
305. Rodríguez-Sevilla, P., Arita, Y., Liu, X., Jaque, D. & Dholakia, K. The temperature of an optically trapped, rotating microparticle. *ACS Photonics* **5,** 3772–3778 (2018).
306. Israelachvili, J. N. *Intermolecular and surface forces* (Academic Press, 2011).
307. Lauga, E. & Squires, T. M. Brownian motion near a partial-slip boundary: A local probe of the no-slip condition. *Physics of Fluids* **17,** 103102 (2005).
308. Brenner, H. The slow motion of a sphere through a viscous fluid towards a plane surface. *Chemical Engineering Science* **16,** 242–251 (1961).
309. Leach, J. *et al.* Comparison of Faxén's correction for a microsphere translating or rotating near a surface. *Physical Review E* **79,** 026301 (2009).
310. Taflove, A. & Hagness, S. C. Computational electromagnetics: the finite-difference time-domain method. *Artech House, Boston,* 149–161 (1995).
311. COMSOL Multiphysics. *Analyze Thermal Effects with the Heat Transfer Module* Accessed: 2021-01-08. `https://www.comsol.com/heat-transfer-modul`.
312. Fedlheim, D. L. & Foss, C. A. *Metal nanoparticles: synthesis, characterization, and applications* (CRC Press, 2001).
313. Madou, M. J. *Fundamentals of microfabrication: the science of miniaturization* (CRC Press, 2018).
314. Feynman, R. P. There's plenty of room at the bottom. *California Institute of Technology, Engineering and Science magazine* (1960).
315. McPeak, K. M. *et al.* Plasmonic films can easily be better: rules and recipes. *ACS Photonics* **2,** 326–333 (2015).
316. Chen, Y. Nanofabrication by electron beam lithography and its applications: A review. *Microelectronic Engineering* **135,** 57–72 (2015).
317. Fredriksson, H. *et al.* Hole-mask colloidal lithography. *Advanced Materials* **19,** 4297–4302 (2007).
318. Dahlin, A. *et al.* Localized surface plasmon resonance sensing of lipid-membrane-mediated biorecognition events. *Journal of the American Chemical Society* **127,** 5043–5048 (2005).
319. Shegai, T. *et al.* A bimetallic nanoantenna for directional colour routing. *Nature Communications* **2,** 1–6 (2011).
320. Odebo Länk, N., Verre, R., Johansson, P. & Käll, M. Large-scale silicon nanophotonic metasurfaces with polarization independent near-perfect absorption. *Nano Letters* **17,** 3054–3060 (2017).
321. Wang, Y., Zhang, M., Lai, Y. & Chi, L. Advanced colloidal lithography: From patterning to applications. *Nano Today* **22,** 36–61 (2018).
322. Jafri, I. H., Busta, H. & Walsh, S. T. *Critical point drying and cleaning for MEMS technology* in *MEMS Reliability for Critical and Space Applications* **3880** (1999), 51–58.
323. Faraday, M. LIX. Experimental relations of gold (and other metals) to light. – The Bakerian lecture. *The London, Edinburgh, and Dublin Philosophical Magazine and Journal of Science* **14,** 512–539 (1857).
324. Xia, Y., Gilroy, K. D., Peng, H.-C. & Xia, X. Seed-mediated growth of colloidal metal nanocrystals. *Angewandte Chemie International Edition* **56,** 60–95 (2017).
325. Ye, X., Zheng, C., Chen, J., Gao, Y. & Murray, C. B. Using binary surfactant mixtures to simultaneously improve the dimensional tunability and monodispersity in the seeded growth of gold nanorods. *Nano Letters* **13,** 765–771 (2013).

326. Guerrero-Martínez, A., Barbosa, S., Pastoriza-Santos, I. & Liz-Marzán, L. M. Nanostars shine bright for you: colloidal synthesis, properties and applications of branched metallic nanoparticles. *Current Opinion in Colloid & Interface Science* **16,** 118–127 (2011).
327. Romo-Herrera, J. M., Alvarez-Puebla, R. A. & Liz-Marzán, L. M. Controlled assembly of plasmonic colloidal nanoparticle clusters. *Nanoscale* **3,** 1304–1315 (2011).
328. Dreaden, E. C., Alkilany, A. M., Huang, X., Murphy, C. J. & El-Sayed, M. A. The golden age: gold nanoparticles for biomedicine. *Chemical Society Reviews* **41,** 2740–2779 (2012).
329. Wiley, B., Sun, Y., Mayers, B. & Xia, Y. Shape-controlled synthesis of metal nanostructures: the case of silver. *Chemistry–A European Journal* **11,** 454–463 (2005).
330. Lu, X., Rycenga, M., Skrabalak, S. E., Wiley, B. & Xia, Y. Chemical synthesis of novel plasmonic nanoparticles. *Annual Review of Physical Chemistry* **60,** 167–192 (2009).
331. Valodkar, M., Modi, S., Pal, A. & Thakore, S. Synthesis and anti-bacterial activity of Cu, Ag and Cu–Ag alloy nanoparticles: a green approach. *Materials Research Bulletin* **46,** 384–389 (2011).
332. Ghosh Chaudhuri, R. & Paria, S. Core/shell nanoparticles: classes, properties, synthesis mechanisms, characterization, and applications. *Chemical Reviews* **112,** 2373–2433 (2012).
333. Tsung, C.-K. *et al.* Selective shortening of single-crystalline gold nanorods by mild oxidation. *Journal of the American Chemical Society* **128,** 5352–5353 (2006).
334. Turkevich, J., Stevenson, P. C. & Hillier, J. A study of the nucleation and growth processes in the synthesis of colloidal gold. *Discussions of the Faraday Society* **11,** 55–75 (1951).
335. Frens, G. Controlled nucleation for the regulation of the particle size in monodisperse gold suspensions. *Nature Physical Science* **241,** 20–22 (1973).
336. Bastús, N. G., Comenge, J. & Puntes, V. Kinetically controlled seeded growth synthesis of citrate-stabilized gold nanoparticles of up to 200 nm: size focusing versus Ostwald ripening. *Langmuir* **27,** 11098–11105 (2011).
337. Jana, N. R., Gearheart, L. & Murphy, C. J. Wet chemical synthesis of high aspect ratio cylindrical gold nanorods. *The Journal of Physical Chemistry B* **105,** 4065–4067 (2001).
338. Khlebtsov, N. & Dykman, L. Biodistribution and toxicity of engineered gold nanoparticles: a review of in vitro and in vivo studies. *Chemical Society Reviews* **40,** 1647–1671 (2011).
339. Inkpen, M. S. *et al.* Non-chemisorbed gold–sulfur binding prevails in self-assembled monolayers. *Nature Chemistry* **11,** 351–358 (2019).
340. Judy, J. W. Microelectromechanical systems (MEMS): fabrication, design and applications. *Smart Materials and Structures* **10,** 1115 (2001).
341. Fu, X. *et al.* Top-down fabrication of shape-controlled, monodisperse nanoparticles for biomedical applications. *Advanced Drug Delivery Reviews* **132,** 169–187 (2018).
342. Liu, M., Zentgraf, T., Liu, Y., Bartal, G. & Zhang, X. Light-driven nanoscale plasmonic motors. *Nature Nanotechnology* **5,** 570 (2010).
343. Shi, L. *et al.* Monodisperse silicon nanocavities and photonic crystals with magnetic response in the optical region. *Nature Communications* **4,** 1–7 (2013).
344. Lu, X., Hessel, C. M., Yu, Y., Bogart, T. D. & Korgel, B. A. Colloidal luminescent silicon nanorods. *Nano Letters* **13,** 3101–3105 (2013).
345. Dasog, M., Kehrle, J., Rieger, B. & Veinot, J. G. Silicon nanocrystals and silicon-polymer hybrids: Synthesis, surface engineering, and applications. *Angewandte Chemie International Edition* **55,** 2322–2339 (2016).
346. Shavel, A, Guerrini, L & Alvarez-Puebla, R. Colloidal synthesis of silicon nanoparticles in molten salts. *Nanoscale* **9,** 8157–8163 (2017).
347. Verre, R., Odebo Länk, N., Andrén, D., Šípová, H. & Käll, M. Large-scale fabrication of shaped high index dielectric nanoparticles on a substrate and in solution. *Advanced Optical Materials* **6,** 1701253 (2018).
348. Hajizadeh, F. *et al.* Brownian fluctuations of an optically rotated nanorod. *Optica* **4,** 746–751 (2017).
349. Schott, A. TIE-36: Fluorescence of optical glass (2010).

350. Prieve, D. C. Measurement of colloidal forces with TIRM. *Advances in Colloid and Interface Science* **82,** 93–125 (1999).
351. Brown, M., Smith, A. & Staples, E. A method using total internal reflection microscopy and radiation pressure to study weak interaction forces of particles near surfaces. *Langmuir* **5,** 1319–1324 (1989).
352. Bevan, M. A. & Prieve, D. C. Direct measurement of retarded van der Waals attraction. *Langmuir* **15,** 7925–7936 (1999).
353. Walz, J. Y. & Prieve, D. C. Prediction and measurement of the optical trapping forces on a microscopic dielectric sphere. *Langmuir* **8,** 3073–3082 (1992).
354. Hertlein, C., Helden, L., Gambassi, A., Dietrich, S. & Bechinger, C. Direct measurement of critical Casimir forces. *Nature* **451,** 172 (2008).
355. Helden, L., Eichhorn, R. & Bechinger, C. Direct measurement of thermophoretic forces. *Soft Matter* **11,** 2379–2386 (2015).
356. Liu, L., Woolf, A., Rodriguez, A. W. & Capasso, F. Absolute position total internal reflection microscopy with an optical tweezer. *Proceedings of the National Academy of Sciences* **111,** E5609–E5615 (2014).
357. Eichmann, S. L., Anekal, S. G. & Bevan, M. A. Electrostatically confined nanoparticle interactions and dynamics. *Langmuir* **24,** 714–721 (2008).
358. Kurvits, J. A., Jiang, M. & Zia, R. Comparative analysis of imaging configurations and objectives for Fourier microscopy. *JOSA A* **32,** 2082–2092 (2015).
359. Risken, H. in *The Fokker-Planck Equation* 63–95 (Springer, 1996).
360. Bussi, G. & Parrinello, M. Accurate sampling using Langevin dynamics. *Physical Review E* **75,** 056707 (2007).
361. Might, M. *The illustrated guide to a Ph.D.* Accessed: 2021-02-09. `http://matt.might.net/articles/phd-school-in-pictures/`.
362. Atwater, H. A 20-year race to the bottom. *ACS Photonics* **8,** 1–2 (2021).
363. Baumgartl, J., Mazilu, M. & Dholakia, K. Optically mediated particle clearing using Airy wavepackets. *Nature Photonics* **2,** 675–678 (2008).
364. Arlt, J., Garcés-Chávez, V., Sibbett, W. & Dholakia, K. Optical micromanipulation using a Bessel light beam. *Optics Communications* **197,** 239–245 (2001).
365. Chen, J., Ng, J., Lin, Z. & Chan, C. Optical pulling force. *Nature Photonics* **5,** 531–534 (2011).
366. Ilic, O. *et al.* Topologically enabled optical nanomotors. *Science Advances* **3,** e1602738 (2017).
367. Wang, S. & Chan, C. Lateral optical force on chiral particles near a surface. *Nature Communications* **5,** 1–8 (2014).
368. Rodríguez-Fortuño, F. J., Engheta, N., Martínez, A. & Zayats, A. V. Lateral forces on circularly polarizable particles near a surface. *Nature Communications* **6,** 8799 (2015).
369. Burns, M. M., Fournier, J.-M. & Golovchenko, J. A. Optical binding. *Physical Review Letters* **63,** 1233 (1989).
370. Miljkovic, V. D., Pakizeh, T., Sepulveda, B., Johansson, P. & Käll, M. Optical forces in plasmonic nanoparticle dimers. *The Journal of Physical Chemistry C* **114,** 7472–7479 (2010).
371. Dholakia, K. & Zemánek, P. Colloquium: Gripped by light: Optical binding. *Reviews of Modern Physics* **82,** 1767 (2010).
372. Han, F. *et al.* Crossover from positive to negative optical torque in mesoscale optical matter. *Nature Communications* **9,** 1–8 (2018).
373. Maier, C. M. *et al.* Optical and thermophoretic control of Janus nanopen injection into living cells. *Nano Letters* **18,** 7935–7941 (2018).
374. Juan, M. L., Righini, M. & Quidant, R. Plasmon nano-optical tweezers. *Nature Photonics* **5,** 349 (2011).
375. Xu, Z., Song, W. & Crozier, K. B. Optical trapping of nanoparticles using all-silicon nanoantennas. *ACS Photonics* **5,** 4993–5001 (2018).
376. Friedrich, L. & Rohrbach, A. Surface imaging beyond the diffraction limit with optically trapped spheres. *Nature Nanotechnology* **10,** 1064–1069 (2015).

377. Andres-Arroyo, A., Gupta, B., Wang, F., Gooding, J. J. & Reece, P. J. Optical manipulation and spectroscopy of silicon nanoparticles exhibiting dielectric resonances. *Nano Letters* **16,** 1903–1910 (2016).
378. Länk, N. O., Johansson, P. & Käll, M. Directional scattering and multipolar contributions to optical forces on silicon nanoparticles in focused laser beams. *Optics Express* **26,** 29074–29085 (2018).
379. Tang, Y. *et al.* Versatile Multilayer Metamaterial Nanoparticles with Tailored Optical Constants for Force and Torque Transduction. *ACS Nano* **14,** 14895–14906 (2020).
380. Ren, H. *et al.* Complex-amplitude metasurface-based orbital angular momentum holography in momentum space. *Nature Nanotechnology* **15,** 948–955 (2020).